AD-A082 134 CARNEGIE-MELLON UNIV PITTSBURGH PA DEPT OF ELECTRICA--ETC F/G 17/7
OPTICAL PATTERN RECOGNITION FOR MISSILE GUIDANCE.(U)
OCT 79 D CASASENT AFOSR-75-2851

UNCLASSIFIED AFOSR-TR-80-0158 NL

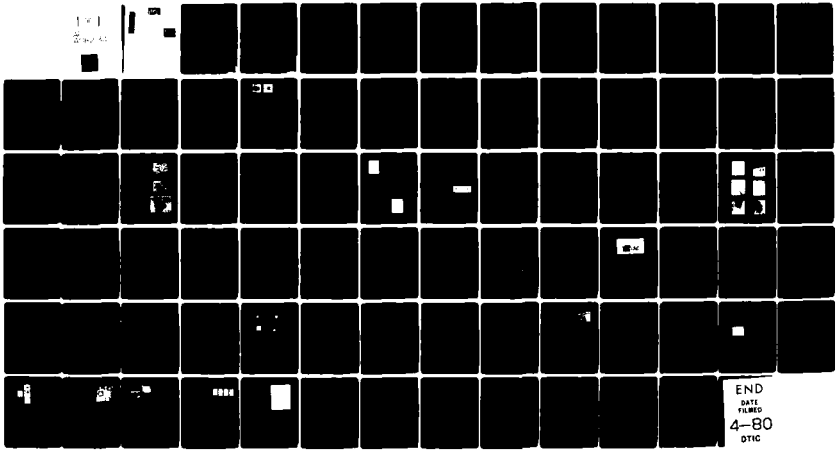

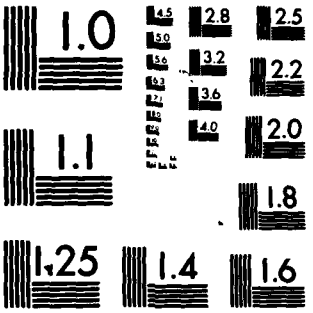

MICROCOPY RESOLUTION TEST CHART

UNCLASSIFIED REPORT DOCUMENTATION PAGE

BEFORE COMPLETING FORM

1. REPORT NUMBER: AFOSR-TR-80-0158

2. GOVT ACCESSION NO

3. RECIPIENT'S CATALOG NUMBER

4. TITLE (and Subtitle): Optical Pattern Recognition for Missile Guidance

5. TYPE OF REPORT & PERIOD COVERED: Final Report, October 1974 -- October 1979

6. PERFORMING ORG. REPORT NUMBER: ---

7. AUTHOR(s): David Casasent

8. CONTRACT OR GRANT NUMBER(s): AFOSR-75-2851

9. PERFORMING ORGANIZATION NAME AND ADDRESS
Carnegie-Mellon University
Department of Electrical Engineering
Pittsburgh, PA 15213

10. PROGRAM ELEMENT, PROJECT, TASK AREA & WORK UNIT NUMBERS
2305/B2
61102F

11. CONTROLLING OFFICE NAME AND ADDRESS
AFOSR/NE
Building 410
Bolling AFB, Washington, D.C. 20332

12. REPORT DATE: 1 Oct[redacted]79

13. NUMBER OF PAGES: 91

14. MONITORING AGENCY NAME & ADDRESS (if different from Controlling Office)

15. SECURITY CLASS. (of this report): Unclassified

15a. DECLASSIFICATION/DOWNGRADING SCHEDULE: N/A

16. DISTRIBUTION STATEMENT (of this Report)

Approved for public release; distribution unlimited.

17. DISTRIBUTION STATEMENT (of the abstract entered in Block 20, if different from Report)

Final rept. 1 Oct 78-31 Sep 79

18. SUPPLEMENTARY NOTES

19. KEY WORDS (Continue on reverse side if necessary and identify by block number)
Coherence measure correlator, equalization correlator, liquid crystal, missile guidance, multi-sensor pattern recognition, normalized invariant moments, optical data processing, optical pattern recognition, photo-DKDP, space-variant pattern recognition, spatial light modulators.

20. ABSTRACT (Continue on reverse side if necessary and identify by block number)
In the past year, our research on optical pattern recognition (OPR) for missile guidance has addressed three general areas: new OPR techniques, OPR experiments on specific missile guidance problems and scenarios, and component evaluation and testing. In the area of component evaluation and testing, we have concentrated on 2-D spatial light modulators (SLM) with specific attention to the photo-DKDP, prom, and the liquid crystal light valve and to a general test and evaluation procedure for these devices. The major results of this program phase has been the development of a general SLM test and evaluation

DD FORM 1 JAN 73 1473 EDITION OF 1 NOV 65 IS OBSOLETE

403445

Unclassified
SECURITY CLASSIFICATION OF THIS PAGE (When Data Entered)

procedure. Our in house test and evaluation program found the photo-DKDP and CCD addressed SLMs worthy of future research and development. In the area of new OPR techniques, we have developed a coherence measure correlator, an equalization correlator, moment invariant hybrid correlator and an averaged filter correlator. Specific missile guidance scenarios pursued were OPR of multisensor and infrared imagery. The former has laid initial ground work for a future program in optical statistical and deterministic pattern recognition. The latter has initiated a generalized approach to OPR using hyperspace formulations and linear combinations of orthonormal basis functions.

OPTICAL PATTERN RECOGNITION FOR MISSILE GUIDANCE

Final Report
1 October 1979

Period Covered

1 October 1978 -- 31 September 1979

Prepared for

Air Force Office of Scientific Research

AFOSR -- NE
Building 410
Bolling Air Force Base
Washington, D.C. 20332

Attention: Captain John Neff

Prepared by

David Casasent
Principal Investigator
Carnegie-Mellon University
Department of Electrical Engineering
Pittsburgh, Pennsylvania 15213

AIR FORCE [illegible] (AFSC)
[illegible] is
[illegible] (7b).
[illegible]
A. D. BLOSE
Technical Information Officer

ABSTRACT

~~In the past year~~, our research on optical pattern recognition (OPR) for missile guidance has addressed three general areas: new OPR techniques, OPR experiments on specific missile guidance problems and scenarios, and component evaluation and testing. In the area of component evaluation and testing, ~~we have~~ has been concentrated on 2-D spatial light modulators (SLM) with specific attention to the photo-DKDP, prom, and the liquid crystal light valve and to a general test and evaluation procedure for these devices. ~~The major results~~ of this ~~program phase has~~ been the development of a general SLM test and evaluation procedure has been developed. ~~Our in house test and~~ evaluation ~~program found the~~ photo-DKDP and CCD ~~addressed~~ SLMs worthy of future research and development. In the area of new OPR techniques, ~~we have developed~~ a coherence measure correlator, an equalization correlator, moment invariant hybrid correlator and an averaged filter correlator have been developed. Specific missile guidance scenarios persued were OPR of multi-sensor and infrared imagery. The former has laid initial ground work for a future program in optical statistical and deterministic pattern recognition. The latter has initiated a generalized approach to OPR using hyperspace formulations and linear combinations of orthonormal basis functions.

Accession For
NTIS GRA&I ☑
DDC TAB ☐
Unannounced ☐
Justification
By
Distribution/
Availability Codes
Dist | Avail and/or special
A

1. INTRODUCTION

In the past year, our research on OPR for missile guidance has concentrated on three general areas: (1) component evaluation, (2) new OPR techniques, and (3) demonstration of OPR on several specific missile guidance data bases.

As the most critical OPR system components we correctly choose the 2-D real-time and reusable SLM. In the course of the past year, we have performed in house evaluation of the liquid crystal light valve (LCLV) and the photo-DKDP SLMs. The results of our general SLM program are summarized in chapter 2. In this paper, we address the general test and evaluation procedure to be used for these components. Such an effort is vital if comparisons and fair evaluations of the diverse candidate SLMs are to be possible. Many detailed experiments were performed on the photo-DKDP SLM in many theoretical studies of this device were performed in conjunction with researchers in France. The results of these tests are summarized in chapter 3. We found this SLM to be one of the most promising ones, with considerable development research possible that should result in a viable device. The results of our in house evaluation of several LCLV SLMs are included in chapter 2. The major flaw in this SLM appears to be its spatially varying nonuniformity of response due to small differences in the thickness of the LC layer. These results and details of the associated theory will comprise a portion of our next annual report.

OPR techniques have classicaly relied on the matched spatial filter (MSF) and the frequency plane correlator (FPC). We have considered and developed several alternatives to this system over the past year. A hybrid coherent system described in chapter 4 is a modification of the joint transform correlator in which the second Fourier transform is performed digitally. The resultant system is a coherence measure correlator. It is of immense use in 1-D pattern recognition such as for Tercom in conjunction with a phase lock loop output

sensor. A modification of this system (the equalization correlator) allows one to correct for different known space-invariant degrading point spread functions in the correlation. The third new OPR technique we have developed is the use of a weighted MSF synthesis system to combine the edge enhancement preprocessing step (found to be of use in multi-sensor image pattern recognition) and MSF correlation into a single one step processor. This research is summarized in chapter 5. The fourth new OPR technique we have developed is the use of an average MSF formed from a linear combination of orthonormal basis functions. In this system, the problem of immediate concern is the recognition of an object independent of its orientation using an average filter. This research is summarized in chapter 6. The fifth and final new OPR technique we have performed initial research on in the past year involves a hybrid optical/digital system to compute the absolute normalized invariant moments of an object. Computation of these feature vectors by digital techniques can then provide the desired pattern recognition information on the presence of an object independent of its geometric orientation. The initial results of this research are summarized in chapter 7.

The final phase of our research on the use of OPR techniques for missile guidance involves the test and evaluation of various OPR methods on divers AFOSR image data bases and missile guidance scenarios. In chapter 3, we briefly discuss the results of our research on real-time SLMs for visible image pattern recognition. In chapter 4, uses made of imagery from WPAFB. In chapter 5, a multi-sensor missile guidance image pattern recognition problem is described and the results of tests performed on a data base consisting of visible and radar scenes are presented. In chapter 6, we utilize a high resolution infrared image data base of key objects, specifically tanks, in a terminal guidance pattern recognition problem. In all of these scenarios, with new OPR techniques and

refinements in existing techniques, successful pattern recognition was obtained by optical computing systems. These systems are most promising for future advance missile guidance applications.

A summary paper of coherent OPR research is included as chapter 8. A list of the 14 papers published in the past year and 22 talks presented in the past year on our AFOSR sponsored research are listed in chapters 9 and 10.

CHAPTER 2

PERFORMANCE EVALUATION OF SPATIAL LIGHT MODULATORS

Reprinted from APPLIED OPTICS, Vol. 18, page 2445, July 15, 1979
Copyright © 1979 by the Optical Society of America and reprinted by permission of the copyright owner.

Performance evaluation of spatial light modulators

David Casasent

An experimental test procedure and associated theoretical formulations are described for the evaluation of spatial light modulators (SLMs) for coherent optical computing. The experimental data included were obtained by us on Hughes liquid crystal and photo DKDP SLMs among others. However, in this paper we address only the general procedures to be used to evaluate SLM performance. The detailed aspects of these tests and their relationships to specific SLMs will be covered in separate papers.

I. Introduction

Optical computing[1] offers the attractive features of parallel processing in real time and thus has been of considerable research interest. It has long been recognized that to realize these advantages of such systems, real-time, reusable, 2-D input and often filter plane transducers are essential. These components are referred to as spatial light modulators (SLMs).[2-4] Our present concern will be with the experimental procedures we feel should be used in the evaluation of SLMs. By this approach we hope to clarify many of the misconceptions present concerning the use of SLMs, interpreting the published specifications for these SLMs, devising appropriate acceptance tests for these SLMs, and the procedures to be used to perform these tests.

The appropriateness of various tests depends on and varies with the SLM used as well as the intended application. Space does not permit an extensive discussion of all SLMs[2-4] or of all optical computing applications,[1] and certainly not extensive discussions of when each test is appropriate. The reader will thus have to be content with general remarks (the purpose of this paper). Experimental results of various test methods applied to the Hughes hybrid field-effect liquid crystal,[5] photo KD*P (deuterated potassium dihydrogen phosphate),[6-8] and the Prom[9] light valves will be included. The discussions will be such that general conclusions and procedures to be used emerge that are of use in general SLM evaluation. Specific discussions of these data for each individual SLM will be discussed in future papers.

The author is with Carnegie-Mellon University, Department of Electrical Engineering, Pittsburgh, Pennsylvania 15213.
Received 23 December 1978.
0003-6935/79/142445-09$00.50/0.
© 1979 Optical Society of America.

Brief descriptions of the three SLMs used are provided in Sec. II for completeness and to enable future issues to be better understood. We divide SLM performance criteria into three areas: sensitometry (Sec. III); modulation transfer function (MTF) (Sec. IV); and noise (Sec. V). This present paper concerns only optically addressed electrooptical SLMs. More detailed extensions to electron beam addressed SLMs and to phase modulated SLMs can be made and will be detailed later.

II. Electrooptical Optically Addressed SLMs

The three major devices that are representative of this class of SLM[1] are the LCLV (liquid crystal light valve),[5] photo KD*P,[6-8] and the Prom.[9] The LCLV consists of over twenty thin film and other layers. It basically consists of a photoconductor, mirror, light-blocking, and LCLV active material layers between two outer transparent electrodes. In operation, an ac voltage is applied between the electrodes, and the pattern to be recorded is incident on the photoconductor at λ_W, whereas readout is in reflection at λ_R from the LCLV side of the device.

The structure and operation of photo KD*P are similar except no light blocking layer exists, and a dc voltage is present across the electrodes. Other differences are that the polarity and value of this voltage are changed during the write (W), read (R), and erase (E) cycles. The major difference between the LCLV and the other SLMs is the lack of long term storage in the LCLV and the need for active erase mechanisms (apply the proper voltage to the electrodes and flooding the photoconductor with light of the proper λ) in the photo KD*P and Prom. Normally $\lambda_W \simeq 514$ nm and $\lambda_R \simeq 633$ nm. In all cases, readout through crossed polarizers is required.

The Prom differs from the prior SLMs in that the electrooptic crystal is both electrooptical and photoconductive. Since no photoconductor layer is present,

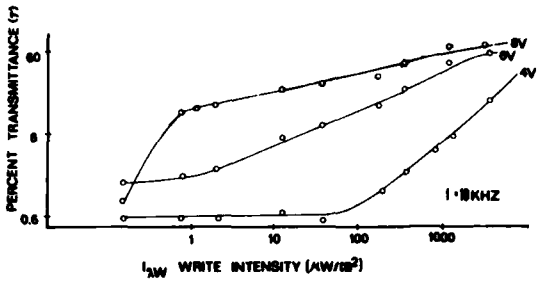

Fig. 1. Global sensitometry curves showing variation with voltage applied across the SLM.

insulating parylene layers are used to produce the required spatial voltage division across the active material proportional to the input λ_W irradiance. It is generally available only in the transmission rather than the reflection readout configuration. Even though no dielectric mirror is present within the SLM structure, it is still generally used in the reflex readout mode.

III. Sensitometry

The representatives of the optically addressed class of SLMs are all sensitive to either the input light irradiance (I) or the light energy (E). The first data required for any SLM is a sensitometry curve of $I_{\lambda W}$ (incident irradiance at λ_W) vs amplitude (t) or irradiance (τ) transmittance. The former curve ($I_{\lambda W}$ vs t) applies when coherent light is used for readout, whereas the latter curve ($I_{\lambda W}$ vs τ) is of use in projection display or similar applications when readout uses noncoherent light. For the LCLV, both the voltage V applied between electrodes and its frequency f affect sensitometry. Such data are shown in Fig. 1 for the LCLV. From these data, we see that the linearity of response, the dynamic range, the useful $I_{\lambda W}$ exposure range, and the $I_{\lambda W}$ threshold at which the device responds all vary with V and f. For the Prom and photo KD*P only V is variable because a dc voltage is applied.

We have found that V and f also affect the SLM noise and the spatial uniformity of the SLM's response. We have also found considerable difference between global sensitometry data (Fig. 1) (obtained by illuminating and reading a large SLM area) and local sensitometry data (Fig. 2) (obtained over a small region of the SLM). Response time, reciprocity data, and other information on the SLM's dynamic response are also of concern and often vary considerably from static data and vary also with the λ_W illumination range used and the address time per point.

A schematic of the basic sensitometry measurement system used is shown in Fig. 3. The vertically polarized λ_R light from a He–Ne laser incident on the polarizing beam splitter (PBS) is reflected toward the SLM. With $I_{\lambda W} = 0$, the λ_R light reflected from the SLM is also vertically polarized and $I_{\lambda R} = 0$. As $I_{\lambda W}$ increases, the elliptical polarization of the λ_R light reflected from the SLM increases and so does the reflected $I_{\lambda R}$ component that passes through the PBS. To obtain local sensitometry data, the spatial variation of such data, and the effect of V and f choices on noise, linearity, and dynamic range, we used apertures A_1 and A_2 shown in Fig. 3. For the LCLV, we illuminated the photoconductor side of the LCLV through only one of the 3-mm² regions of A_1 and measured $I_{\lambda R}$ in all nine 3-mm regions of A_2 as V, f, and $I_{\lambda W}$ were varied. We denote $I_{\lambda R}$ in the corresponding 3-mm² region of A_2 as signal and the $I_{\lambda R}$ value in all other regions of A_2 as noise.

A summary of our results for the LCLV follow. Less noise was observed as f was decreased and V was increased. As f was lowered, the noise tracked the signal at a lower rate. Most important were the large spatial differences we found in the voltage V_T and irradiance $I_{\lambda WT}$ threshold differences (at which $I_{\lambda R}$ changed). Large differences in V_T and $I_{\lambda WT}$ for signal and noise are desirable. For the LCLV, we found V_T to be lower at low f with larger signal and noise thresholds at $f = 1$ kHz than at 10 kHz and with noise tracking the signal slower at lower f values. The local sensitometry data

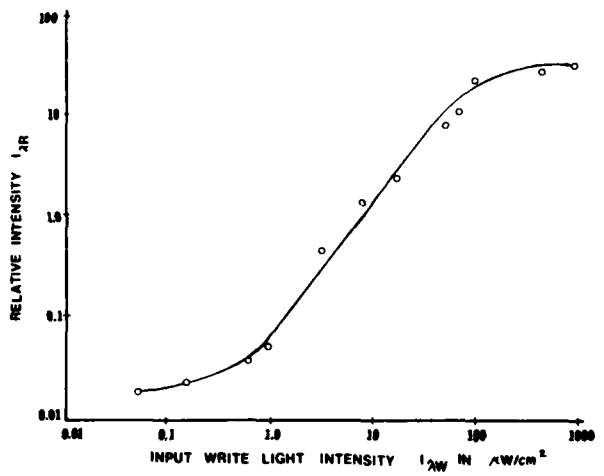

Fig. 2. Representative local sensitometry curve.

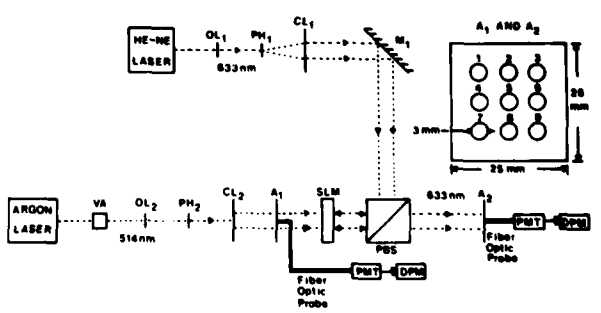

Fig. 3. Schematic diagram of the SLM global and local sensitometry data acquisition system.

for a 3-mm^2 region of the LCLV were shown in Fig. 2. The large 1500:1 contrast ratio and 30,000:1 dynamic range shown in Fig. 2 are misleading, since spatial sensitometry variations make the global values (Fig. 1) for such parameters much less. We have found these spatial variations to be equivalent to horizontal shifts of the sensitometry curve or effectively to changes in $I_{\lambda WT}$ due to spatial variations in the photoconductor, CdTe/CdS heterojunction diode, and LC thickness variations. Thus only global sensitometry data should be used, with local sensitometry data being of use in determining the reasons for the obtained performance and the spatial response uniformity of the device.

The importance of SLM sensitometry data as a first step in SLM testing and other aspects of such data can be seen from Fig. 1. From Fig. 1, we see that the dynamic range of the SLM increases with V. For our application, a large linear dynamic range was desirable, thus V = 4–6 V and f = 10 kHz were chosen as the SLM operating values. Other applications may require emphasis of other SLM features. Previously published[10] LCLV sensitometry data exhibited a knee in the curve (as in the 8-V curve in Fig. 1). However, as shown, proper selection of V and f can result in a linear t-E curve. This feature by which the shape of the SLM's sensitometry curve can be controlled is of potential use in various applications such as 2-D optical analog/digital conversion, halftone screening, homomorphic filtering, etc.

From Fig. 1, we find the global and hence useful linear dynamic range ($I_{\lambda W\ \max}/I_{\lambda W\ \min}$) of the SLM to be about 1000:1, the contrast ratio $I_{\lambda R\ \max}/I_{\lambda R\ \min}$ to be 70:1, and the desirable $I_{\lambda W}$ bias level (center of the linear portion of the curve) to be 70–100 μW/cm^2.

The photodetector used to measure $I_{\lambda R}$ places a lower limit on these curves. For our case, $I_{\lambda R\ \min}$ was 70 nW/cm^2, $t_{\min}$ was 0.78%, and $\tau_{\min}$ was 0.6%. The detector used in such sensitometry tests and the $I_{\lambda W}$ range used should of course be compatible with the levels present during the SLM's intended application. The 22% transmission loss observed ($t_{\max}$ = 78%, $\tau_{\max}$ = 60%) was attributed to incomplete reflections from the dielectric mirror within the LCLV structure, to nonideal alignment of the LCLV molecules, and to the inability of the device to rotate completely vertically polarized input λ_R light into horizontally polarized λ_R reflected light. Lens and PBS losses have been compensated for in the data of Figs. 1 and 2.

Because of the hybrid field effect used in the LCLV, the λ_R wavelength used must be matched to the thickness of the LC layer to optimize contrast ratio.[11,12] For other SLMs, λ_R must be chosen to reduce the destructive effects of reading on a stored image. For other SLMs operated with dc voltages, we have found the dielectric mirrors to pass considerable λ_R light thus degrading a stored pattern while it is being read. Although readout through a crossed polarizer/analyzer or PBS system is theoretically optimum,[11,12] we have found the use of separate polarizers and analyzers oriented slightly off from 90° to increase results and the flexibility of the measurement system.

For integrating or storage mode SLMs such as photo-DKDP, we have found that extra care should be taken in acquiring sensitometry data. Specifically, in the photo-DKDP light valve, we have observed a strong dependence of the photosensitivity of the Se photoconductor to the potential gradient present across it. As a result, when long exposure times and low $I_{\lambda W}$ light levels are used, the SLM's sensitivity to the initial and later photocarriers differs considerably. In such cases, one can obtain very different sensitometry data depending upon the write light exposure time used. As usual and here especially, the test conditions should duplicate those present in the SLM's actual application.

IV. Modulation Transfer Function (MTF)

The MTF of an SLM or any device used in an optical processor is one of the most important but seemingly least understood or most misused parameters. We have analytically and experimentally evaluated over eight different MTF tests. Only the most useful ones are discussed here. The appropriateness of various MTF tests depends upon the specific SLM and its intended system application. A discussion of MTF and definitions might appear too tutorial, but is vital to provide an adequate framework for the MTF data to follow.

A. Theoretical Formulation

We assume the pattern recorded on the SLM to be a sinusoid at spatial frequency u' (in 1-D for simplicity). We first clearly distinguish between amplitude m_A and irradiance m_I modulation by describing the SLM's transmittance by

$$t(x) = (1 + m_A \cos 2\pi u'x), \tag{1a}$$

$$\tau(x) = (1 + m_A \cos 2\pi u'x)^2, \tag{1b}$$

where t and τ denote amplitude and irradiance transmittance, respectively. If a reconstructed image of a test pattern recorded on the SLM is formed using the SLM as a relay and the detected output pattern is scanned, the measured modulation is

$$m = m_I = (I_{\max} - I_{\min})/(I_{\max} + I_{\min}), \tag{2}$$

where $I_{\max}$ and $I_{\min}$ are the measured quantities (the maximum and minimum irradiances in the reconstructed image). A binary image such as the 3-bar Air Force resolution chart is used as the test pattern in such a test.

If noncoherent illumination is used in the above imaging modulation test, the detected pattern (that is scanned to determine $I_{\max}$ and $I_{\min}$) is τ. If the image reconstruction is performed in coherent light, the detected pattern is $|t|^2$. Since $\tau = |t|^2$, no difference should result, and $m = m_I$ defined by Eq. (2) is obtained. In practice, the MTF and OTF of the associated imaging optics used affect the observed output patterns in the coherent and noncoherent illumination cases, respectively. Since the MTF of a system is superior to its OTF, coherent illumination is recommended for any such imaging test (when the modulation of the SLM alone rather than of the entire system, in-

cluding lenses, is desired). We have consistently obtained higher modulation values when coherent rather than noncoherent illumination was used.

Amplitude modulation m_A is the desired MTF parameter in coherent optical processing application. We can relate m_A to m_I as

$$m_I = \frac{A_{\max}^2 - A_{\min}^2}{A_{\max}^2 + A_{\min}^2} = \frac{2m_A}{1 + m_A^2}, \tag{3}$$

which follows directly from the definitions in Eqs. (1) and (2).

However, this relationship is valid only for monotone inputs, and m_I is best obtained in a coherent image reconstruction experiment. We can always obtain m_I from m_A using Eq. (3).

It is also possible and often preferable to measure m from the Fourier transform of Eq. (1). For this case, we use t in Eq. (1a) to describe the transmittance of the SLM. The amplitude of the Fourier transform of Eq. (1a) is

$$T(u) = A_0[\delta(u) + (m_A/2)\delta(u \pm u')]. \tag{4}$$

The irradiances I_0 and I_1 of the dc and each first-order term are easily measurable in the Fourier plane. From Eqs. (1)–(4), these are related to m and the measurable quantity I_1/I_0 by

$$I_0/I_1 = (m_A)^2/4, \tag{5a}$$

$$m_A = 2(I_1/I_0)^{1/2}, \tag{5b}$$

$$m_I = \frac{4(I_1/I_0)^{1/2}}{1 + 4(I_1/I_0)}. \tag{5c}$$

The classic MTF as defined is a plot of normalized modulation m_n:

$$m_n = \frac{m_{\text{out}}(u')/m_{\text{in}}(u')}{m_{\text{out}}(0)/m_{\text{in}}(0)} \tag{6}$$

vs the input spatial frequency u'. The measurable quantity in Eqs. (5) is m_{out}. It generally decreases as u' increases. One generally normalizes m by dividing it by its maximum value $m_{\text{out}}(0)$, which occurs at low or zero spatial frequency (for deformable SLMs with bandpass MTFs, alternate normalizations are required). Further normalization by $m_{\text{in}}(u')/m_{\text{in}}(0)$ is used when the modulation m_{in} of the recorded pattern is not 100% and when m_{in} varies with the recorded spatial frequency u'. Thus, for this classic MTF plot, m_n varies from 1 to 0 as u' increases from 0 spatial frequency.

For reasons we amplify later, we have found the use of an unnormalized m vs u' plot to be preferable. We thus plot m vs u', where

$$m = \frac{m_{\text{out}}(u')}{m_{\text{in}}(u')/m_{\text{in}}(0)}. \tag{7a}$$

For coherent optical systems, an unnormalized amplitude MTF m_A vs u' is used. Generally, we advocate that normalization by the input modulation not be used, rather a plot of

$$m = m_{\text{out}}(u') \tag{7b}$$

vs spatial frequency u' be provided and the constant input modulation be specified. For imaging applications in noncoherent readout light, an unnormalized irradiance MTF curve of m_I vs u' is appropriate. If m is measured in an image plane, Eq. (2) is used; if the measurement is made in a Fourier plane, Eq. (5) is used. In practice, MTF as defined is really a contrast transfer function (since the phase of the imagery is neglected). However, the above definitions have become common of late and relate directly to the intended device parameter we wish to describe and quantify. We will thus still refer to a plot of m vs u as MTF.

For deformable SLMs and phase modulators, the MTF has a bandpass response and $m_{\text{out}}(0) = 0$ and $m = 0$ if t is described by Eq. (1). Thus MTF as described by Eq. (6) is not usable for such devices. Rather, the diffraction efficiency η of these devices is specified. For these SLMs, η is the product of the fraction of the input light in one first-order usable for modulation and the amount of average input light that can be diffracted into one first-order. Thus

$$\eta = \frac{m_A^2/4}{1 + m_A^2/2} \cdot \frac{1 + m_A^2/2}{(1 + m_A)^2} = \frac{m_A^2}{4(1 + m_A)^2} \tag{8}$$

$$\eta = \frac{[1 - (1 - m_A^2)^{1/2}]^2}{[1 + m_A + (1 - m_A^2)^{1/2}]^2} \simeq \frac{m_n^2}{16}. \tag{9}$$

In Eq. (9), m_n is defined by Eq. (6), and $m_{\text{in}} = 1$ and $m_{\text{out}}(0) = 1$ are assumed. The final approximation in Eq. (9) is usually made. This is only valid for small m_n and is not appropriate since $\eta = 1/16$ when $m_n = 1$. However, Eq. (9) is still used to extrapolate MTF from η data since low η values look more impressive when expressed as an MTF.

B. Sensitometry Effects

Three aspects of SLM sensitometry affect MTF. From Figs. 1 and 2, we see that the device's $I_{\lambda W}$ region used should be linear if linear modulation is desired and should cover a large range if optimum modulation is of concern. To achieve either result, control of the average $I_{\lambda W\,\text{avg}}$ write light and/or the input bias light level $I_{\lambda W\,\text{bias}}$ is needed. The recording mechanism used to address the SLM in its intended actual application and the type of input data to be processed affect the bias level and contrast ratio that will actually be present in the input data. For example, reflective aerial imagery usually has a higher bias level and lower contrast than other imagery, whereas signal processing applications usually demand a large dynamic range and linear recording.

A second effect of SLM sensitometry arises when linear recording (a linear relationship between t and $I_{\lambda W}$) is of concern (e.g., as in many signal processing applications). In these cases, use of the proper region of the device's sensitometry curve is vital. The most appropriate method we have found for obtaining linear MTF data is interferometrically (Sec. IV.D) by measuring the second-order Fourier term (I_2) as well as I_0 and I_1. By adjusting the input bias and modulation levels until I_2 is 20 dB below I_1, we can insure that interharmonic distortion is below 1%; we then note that a 1% linear MTF results. Other I_1/I_2 ratios yield MTF data with other degrees of linearity.

The effect of gamma γ (the slope of the SLMs $\tau - I_{\lambda W}$ curve on log-log axes) on MTF is the final effect of sensitometry on MTF that we consider. To include this effect, we assume an irradiance transmittance for the SLM of the form

$$\tau(x) = \tau_0(1 + m_I \cos 2\pi u' x)^{-\gamma}. \tag{10}$$

The Fourier transform of the binomial expansion of $t = \tau^{1/2}$ can be manipulated to relate I_1/I_0 to m_I and γ by Ref. 9:

$$m_I = (4/\gamma)(I_1/I_0)^{1/2}. \tag{11}$$

From Eq. (11), we see that an SLM with $\gamma = 1$ yields twice the irradiance MTF of an SLM with $\gamma = 2$. In most cases, it is inappropriate to separate γ and MTF effects, except when comparing theoretical and experimental resolution data.

C. Imaging MTF

The most used and in some sense the simplest measure of SLM resolution and MTF is obtained by imaging a resolution chart (such as the 3-bar Air Force test chart) onto the SLM, reconstructing the image of the test pattern using the SLM as a relay device, and then scanning the reconstructed image with a photometric microscope. We then measure $I_{\min}$ and $I_{\max}$ for each group/element in the reconstructed image of the test chart; $m_{\text{out}}(u')$ is thus obtained from Eq. (2), and an MTF curve defined by Eq. (7b) not Eq. (6) is plotted. m_A or m_I is used depending upon the application.

Examples of several experimentally obtained unnormalized imaging MTF curves for the LCLV at different voltages and frequencies are shown in Fig. 4. The modulation of the imaging optics used was measured to be unity, whereas m_{in} for the test chart was found to be 0.9 out to 80 cycles/mm. The MTF data presented have been normalized for these values as in Eq. (7b). These initial MTF curves serve to demonstrate several vital aspects of MTF data. First and foremost, unnormalized MTF data must be used since m is then directly the fraction of the input light that is usable for modulation. To demonstrate this, we select the $m = 0.4$ point on both curves. This corresponds to some given amount of usable output light. From Fig. 4(a), we find that we can obtain this amount of light for an input spatial frequency of up to 19 cycles/mm; whereas for the V and f settings used in the Fig. 4(b) data, we can obtain this amount of light only up to 13 cycles/mm of input data. If both curves were normalized, such comparative data would not be present.

Another obvious remark concerning data acquisition is that the MTF data should be continued to low enough spatial frequencies that three approximately equal and constant modulation values result. This is of utmost importance if the MTF curve is normalized. The third issue concerns the SLM resolution one reads from such data. The limiting SLM resolution at $m = 0.05$ is often given but is rarely appropriate for use because of the negligible light levels available at this low modulation. Only a light budget analysis for the full actual system can answer what SLM modulation is necessary. We advocate the use of unnormalized MTF data and that the resolution be given at the $m = 0.5$ or 50% modulation point. In addition, we note that the input $I_{\lambda W}$ bias value and the true input modulation used be provided if any MTF data are to be of use at the system level. Examples of such data follow in Sec. IV.D.

Other peculiarities of MTF data depend on the specific SLM being tested. For the LCLV, we obtained MTF curves for various control voltages and ac frequencies and found the MTF to be better at higher (10-kHz) frequencies. This appears to be due to the increase in the ratio of the transverse-to-longitudinal impedance of the LCLV with frequency. Another specific feature of the LCLV is the effect that the λ_R choice has on the device's performance. To reduce the off-state transmittance of the SLM, the thickness of the LC layer must be properly adjusted, because the twisted nematic effect determines the off state. The thickness of the LC layer in the LCLV we used was optimized for $\lambda_R = 633$ nm. We can partly attribute the lower modulation and resolution obtained in Fig. 4(b) compared with Fig. 4(a) to the broadband λ_R light used in the one case. Other MTF tests performed on the LCLV with

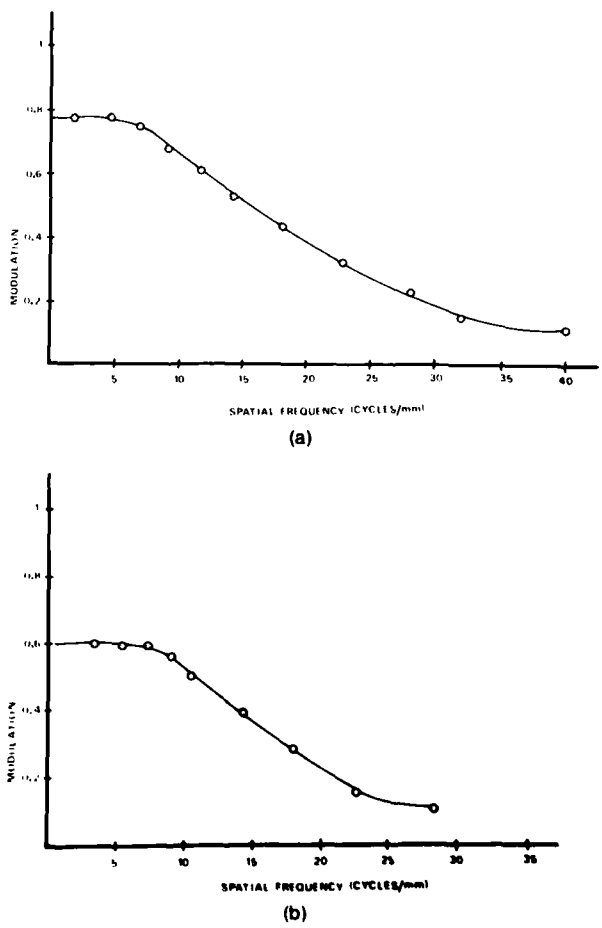

Fig. 4. Imaging MTF curves: (a) 6 V and 10 kHz with coherent $\lambda_R = 633$ nm light; (b) 3.5 V and 10 kHz with noncoherent filtered $\lambda_R = 620 \pm 10$-nm light.

λ_R = 514 nm yielded even poorer modulation and resolution.

Our objections to an imaging MTF test are many. The test is subjective and plagued by operator attitude and error. This is due primarily to the degree to which the input data can be focused onto the SLM. More important, since the test patterns used (3-bar Air Force chart) are binary, this type of test does not investigate the gray scale resolution or linearity of the SLM. Finally, the input bias light level and input modulation are not easily variable in such MTF tests.

D. Interferometric MTF

For the reasons noted above, interferometric MTF data are preferable to imaging MTF data for reasons of both experimental ease and data content. The interferometric MTF data acquisition system used is shown in Fig. 5. In this architecture, the interference pattern

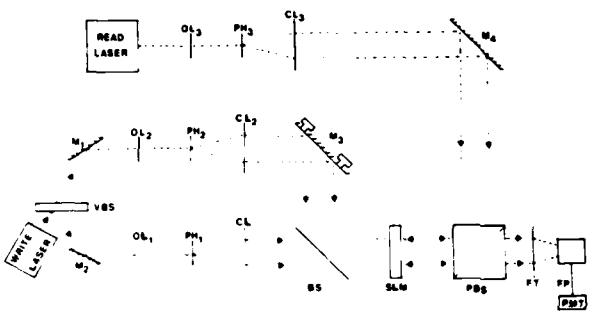

Fig. 5. Schematic diagram of an SLM interferometric MTF data acquisition system.

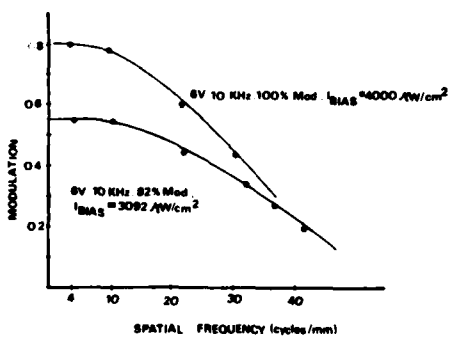

Fig. 6. Nonlinear interferometric MTF curves at different bias and input modulation.

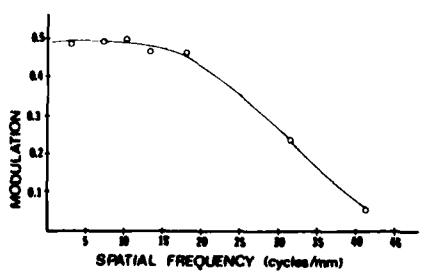

Fig. 7. Linear interferometric MTF curve with 1% SLM linearity.

of two plane waves of irradiances I_A and I_B inclined at an angle θ is recorded. The subsequent amplitude transmittance is

$$t = I_A + I_B + 2(I_A I_B)^{1/2} \cos 2\pi u' x, \tag{12}$$

where $u' = 4\pi(\sin\theta)/\lambda$ is the spatial frequency of the recorded fringe pattern in cycles/mm. From Eqs. (1), (12), and (2), we find

$$m_{\text{in}} = \frac{2(I_A/I_B)^{1/2}}{1 + (I_A/I_B)} = \frac{2R^{1/2}}{1 + R}. \tag{13}$$

From Eq. (13), we see that by varying the ratio R of the intensities of the two beams, we can control m. By controlling $I_{\text{avg}} = I_A + I_B$, we can vary the bias point chosen on the SLM's sensitometry curve. By varying θ by changing the tilt angle of mirror M_3, the spatial frequency u' can be changed. The Fourier transform of Eq. (13) can then be scanned by a fiber optic probe (FP), photometric microscope, and photomultiplier (PMT) system.

This system topology of Fig. 5 thus allows us to vary easily the bias level, spatial frequency u', and modulation m of the input fringe pattern. Of further concern is the fact that the sine wave pattern in Eq. (13) is automatically in focus over the entire thickness of the SLM, thus completely overcoming any input focusing errors that could arise in an imaging MTF system. To obtain the MTF of the SLM, we can monitor I_0 and I_1 in the Fourier transform of Eq. (13) for different u' input spatial frequencies and apply Eq. (5b) or Eq. (5c) to determine m. Equation (7b) is then used to obtain the MTF plot of m vs u'.

Two such MTF curves are shown in Fig. 6 with slightly different m_{in} and I_{avg} levels. These two curves vividly demonstrate many of the MTF remarks advanced earlier. The effect of a slight 18% change in m_{in} on MTF is seen to be dramatic. With a lower m_{in}, less of the SLM's sensitometry curve is used and the reduced m shown results. The need to specify MTF test conditions (I_{avg} and m_{in}) is thus apparent. Similarly, only through unnormalized MTF data, as shown, do these differences appear. In the lower curve in Fig. 6, we find a lower peak m (due to the lower m_{in}); but the resolution (at 50% of the peak m value) is found to be larger (37 cycles/mm) for the lower m_{in} = 0.82 case than for the larger m_{in} = 1.0 case (32 cycles/mm). However, the unnormalized MTF data of Fig. 6 clearly convey the point that more usable output light is always present with the larger m_{in} value. Such results would not appear in MTF data if the normalized MTF definition in Eq. (6) were used. Similarly, the relevance of these data would not be of use unless I_{avg} and m_{in} were specified as done in Fig. 6.

We refer to the data of Fig. 6 as a nonlinear MTF curve. A linear MTF curve for the same LCLV SLM is shown in Fig. 7. To obtain these latter data, I_2 was monitored as well as I_1/I_0. By keeping I_2 below I_1 by 20 dB (by reducing m_{in} and adjusting I_{avg} accordingly), we can ensure that the SLM's resultant MTF is linear within 1% (i.e., less than 1% interharmonic distortion). With I_{avg} adjusted to lie in the center of the linear por-

tion of the SLM's sensitometry curve of Fig. 1 and with m_{in} reduced to 0.79, the curve of Fig. 7 results. The resolution at $m = 0.25$ (50% of the peak $m = 0.5$ value) is seen to be 32 cycles/mm. The modulation at 32 cycles/mm is below that obtainable for nonlinear SLM operation in Fig. 6 as expected. Only such fully documented and unnormalized MTF data are of use in deciding on the performance to be expected of an SLM in a given application as well as in comparing the MTFs of different SLMs.

The effect of modulation on the performance of an optical correlator is rarely quantified, but is of major concern in determining the usable SLM resolution in a system scenario. For example, an irradiance modulation of 10% is equivalent to an amplitude modulation of 5%. The resultant peak intensity in one sidelobe in the Fourier plane pattern is 32 dB below dc. This represents an intolerable loss in most cases. Such light level budget analyses are needed for each specific application to determine the necessary system performance. The output detector used greatly affects such system data.

E. Depth of Focus

Interferometric MTF data are more reproducible than imaging MTF data and include gray scale and linearity information on the SLM. It has thus become the most used MTF data acquisition method. However, because of the infinite depth of field of the recorded fringe pattern (the feature that makes this MTF method easy to perform), this test may yield different results than one would obtain in the SLM's actual system application. The actual depth of focus of the interferometric fringe pattern is effectively the thickness of the photoconductor layer (10 μm) for photo-KD*P and the LCLV. However, the Prom crystal is thick (500–900 μm) and both electrooptic and photoconductive. For such devices, the depth of focus of the interferometric pattern is effectively the crystal's thickness.

Interferometric MTF data will be valid only if the SLM's actual data recording system has a depth of focus comparable with the thickness of the photoconductor or crystal (depending upon the SLM). In addition, for an SLM such as photo-KD*P with a 10-μm thick photoconductor layer, interferometric MTF data are only valid up to 50-cycle/mm input spatial frequencies (the reciprocal of 2×10 μm) and only if the depth of focus of the data recording system in the device's actual application exceeds 10 μm. When the SLM is used in the frequency plane and interference patterns such as a matched spatial filter[13] or joint transform[14] are recorded on it, the interferometric MTF is, of course, valid. When the SLM is used as an image plane transducer, the infinite depth of focus assumption is not always valid. If low f-number optics are used, care must be taken that the thickness of the photoconductor does not exceed the depth of focus of the actual recording optics used. For f-number optics with a 10-μm spot size, the depth of focus is

$$\text{depth of focus} = 2\,(f\text{-number})(\text{spot size}) = 80\ \mu\text{m}. \quad (14)$$

If the photoconductor's thickness (or the active crystal thickness for the case of the Prom) exceeds this 80-μm value, interferometric MTF test data are not appropriate. In actual use, the MTF will decrease because of overlap of the light cone away from focus. In summary, interferometric MTF data will yield the best possible SLM resolution and modulation. Whether such SLM performance is actually obtainable depends upon the specific way the SLM is used in the actual system application.

F. Alternate MTF Tests

The usefulness, ease of implementation, and reproducibility of over eight MTF tests were evaluated first-hand on over four different SLMs during this program. MTF tests that required sine wave input transparencies of various spatial frequencies and LFM Sayce charts of linearly varying spatial frequency were found to suffer from lack of inputs of adequate precision. Correlation-based MTF tests[15] were found to be plagued by low light levels and diffraction efficiency (i.e., the problem became one of measuring detector accuracy rather than SLM performance).

One attractive MTF test that is appropriate for evaluation of SLMs in system applications in which data are written sequentially on the SLM by a scanning recording device is the edge or gradient MTF test method.[16-18] In such a test, an edge is imaged onto the SLM, and its reconstructed image (using the SLM as a relay device), is scanned. These data are then smoothed and can be corrected for the SLM's sensitometry curve if appropriate. Differentiation of such an edge image results in the SLM's line spread function. The Fourier transform of this line spread function is then the SLM's optical transfer function, whose magnitude is the device's MTF. The operations of smoothing, sensitometry correction, differentiation, Fourier transformation, and magnitude calculation on the edge image are generally performed in digital electronics. This results in a rather indirect MTF calculation. This fact plus the requirement that the system be space-invariant in the image analysis domain (optical systems are in fact space-variant)[19-21] tend to reduce the potential appropriateness of this MTF analysis method. In time, dedicated hardware and software advances may change this observation.

V. Noise

The third and final aspect of SLM evaluation to be discussed is that of SLM noise. We distinguish four types of noise: distortions; phase; and scatter and signal-dependent noise.

A. Distortion

Distortion is of concern when linear recording is required. MTF data with control of the interharmonic distortion level can be measured by the linear interferometric MTF technique described in Sec. IV.D.

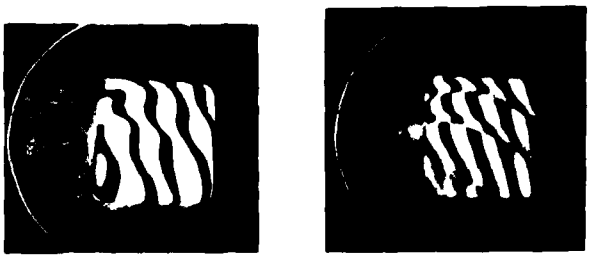

(a) (b)

Fig. 8. Interferograms of the OPD of an SLM: (a) 0 V; (b) 5 V, 6 kHz.

B. Phase Error

Phase errors are of utmost concern in coherent optical correlators. Slowly varying phase errors or linear phase errors are not of major concern except in optical correlators. Such error sources in coherent optical computers are best described by optical path difference (OPD) maps.[21-24] Such OPD plots must be provided for all input spatial frequencies and aperture sizes to characterize completely a coherent optical system.[22] To relate these phase errors to the accuracy of an optical processor, 2-D spatial OPD maps are necessary.[21] Techniques for easily acquiring such data have been previously reported.[23,24] Accurate analysis of such data requires one to model the optical processor and its components as a space-variant system.[19-21] Thus, to obtain quantitatively meaningful SLM phase error data, one must acquire spatial OPD data on the SLM rather than the rms OPD data characteristically available for such components. In summary, it is not the average phase error that matters, but rather how this phase error is distributed.

In obtaining any type of SLM data, even rms OPD, the test should be performed with voltage applied to the SLM [Fig. 8(b)], since often a considerably different OPD phase error results than if no voltage is applied to the device [Fig. 8(a)].

C. Scatter Level

The surface roughness and cosmetic imperfections of the SLM generally manifest themselves as random phase errors of high spatial frequency. These noise sources predominantly contribute to the system's background noise level or scatter level. We refer to this as scatter level noise. It directly affects the maximum obtainable system dynamic range. The extent of this noise source is most easily measured by imaging a square aperture onto the SLM and scanning its Fourier transform pattern. Such a cross-sectional Fourier scan is shown in Fig. 9(b). For comparison purposes, the Fourier transform of an empty square aperture obtained using the same lens system is scanned [Fig. 9(a)]. Care should be taken to extend the Fourier plane scan out to several hundred sidelobes until the pattern's exponential decrease stabilizes.

From Fig. 9(a), we find that the scatter level of the optical system alone [Fig. 9(a)] exceeds 40 dB at $u = 4$ cycles/mm and is within 1 dB of the theoretical value. Comparing Figs. 9(a) and 9(b), we see that the presence of the SLM (the LCLV for this data) results in an increased scatter level 3–5 dB above the theoretical value and above that of the optical system alone.

D. Signal-to-Noise Ratio (SNR)

Signal dependent noise or the ratio of signal to noise level (in the same spatial frequency band) is often of more concern. We have found two methods to be of use in obtaining such data. The first is to record a square-wave pattern on the device by imaging an accurate test pattern onto the SLM. A scan of the Fourier transform of this input square wave is shown in Fig. 10 for a 5-cycle/mm square wave recorded on the LCLV. This pattern shows Fourier components at both even and odd harmonics of the fundamental frequency of the square-wave grating. The amplitudes of these Fourier components are all within 1 dB of the theoretical values found from a Fourier series expansion of the input pattern. Our present concern is with the measurable null depth of this pattern. From Fig. 10, we see that the system's dynamic range, including all SLM noise, is a maximum of 52 dB even with an input signal present.

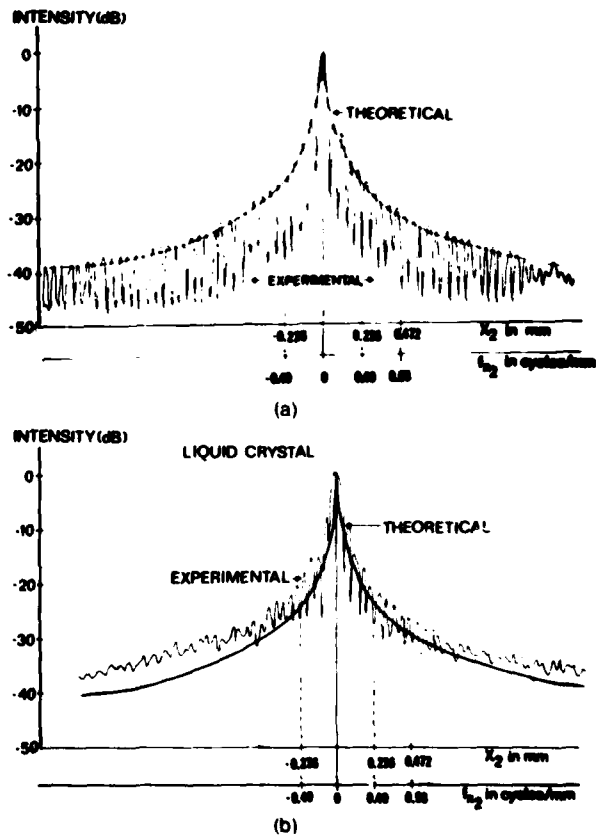

Fig. 9. Cross-sectional scan of the Fourier transform of a square aperture for scatter-level noise tests: (a) empty aperture; (b) SLM in aperture.

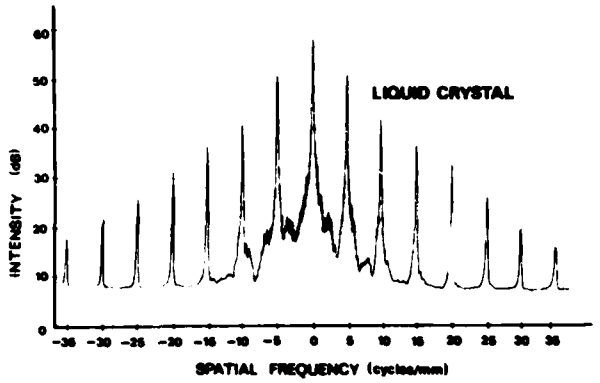

(a)

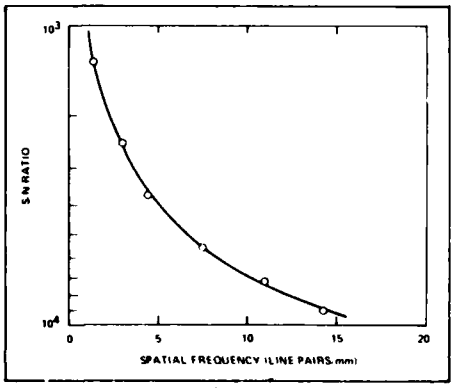

(b)

Fig. 10. SNR SLM test data: (a) cross-sectional scan of the Fourier transform of a square wave recorded on the SLM; (b) plot of SNR vs spatial frequency obtained from Fourier plane data of interferometrically recorded sine waves.[5]

Since the amplitude of increasing Fourier orders of the square wave decreases, whereas the noise level remains essentially constant, true SNR is not obtainable from such data. However, true SNR can be measured by interferometrically recording a sine wave on the SLM and investigating its Fourier transform pattern for various input spatial frequencies u'. The maximum obtainable I_1/I_2 ratio or the I_1 to scatter level ratio obtainable in the Fourier plane will then provide us with the SNR of the SLM vs spatial frequency u'. An example of such data is shown[5] in Fig. 10(b) for the LCLV. The increase in SNR with spatial frequency occurs because the system's scatter level decreases faster with u than the SLM's MTF. Care should be taken to measure such I_1, I_2 and scatter levels with an area photodiode detector whose size equals the diffraction limited spot size of the Fourier transform system used.

VI. Conclusions

As optical computing and SLM technology mature and as more coherent optical processing systems are fabricated and delivered, the specifications and testing of the SLM components (so vital to such systems) must be standardized. We feel the procedure described in this paper and demonstrated by experimental confirmation provide a necessary first step toward such ends.

Many agencies contributed to the studies summarized herein. These include the Ballistic Missile Defense Advanced Technology Center (contracts DASG-60-77-C-0034 and DASG-60-78-C-0054), the U.S. Army Engineer Topographic Lab (contract DAAK 70-78-C-0076), the Air Force Office of Scientific Research (contract AFOSR 75-2851B), and the Office of Naval Research (contract 366-005). The author recognizes James Morris and Sanjiv Natu for obtaining the experimental data contained herein and Demetri Psaltis, Thanh Luu, and B. V. K. Kumar for many valuable technical discussions.

References

1. Special Issue on Optical Computing, Proc. IEEE **65** (January 1977).
2. D. Casasent, Proc. IEEE **65**, 143 (1977).
3. D. Casasent, "Coherent Light Valves," in *Applied Optics and Optical Engineering*, R. Kingslake and B. J. Thompson, Eds. (Adacemic, New York, 1979).
4. Special Issue on Spatial Light Modulators, Opt. Eng. **17** (July 1978).
5. W. Bleha *et al.*, Opt. Eng. **17**, 371 (1978).
6. G. Marie and J. Donjon, Proc. IEEE **61**, 942 (1973).
7. G. Marie, J. Donjon, and J. Hazan, "Pockles Effect Imaging Devices and Their Applications," in *Advances in Image Pick-up and Display Vol. 1*, B. Kazan, Ed. (Academic, New York, 1974), p. 225.
8. D. Casasent, Opt. Eng. **17**, 365 (1978).
9. B. Horwitz and F. Corbett, Opt. Eng. **17**, 353 (1978).
10. J. Grinberg *et al.*, Opt. Eng. **14**, 217 (1975).
11. J. Grinberg and A. Jacobson, J. Opt. Soc. Am. **66**, 1003 (1976).
12. J. Bigelow and R. Kashnow, Appl. Opt. **16**, 2090 (1977).
13. A. Vander Lugt, IEEE Trans. Inf. Theory **IT-10**, 139 (1964).
14. J. Rao, J. Opt. Soc. Am. **57**, 798 (1967).
15. A. Grumet, Appl. Opt. **16**, 154 (1977).
16. R. Barakat, J. Opt. Soc. Am. **54**, 920 (1964).
17. B. Tatian, J. Opt. Soc. Am. **55**, 1014 (1965).
18. D. Dutton, Appl. Opt. **14**, 513 (1975).
19. G. Winzer and I. Kachel, Opt. Acta **20**, 359 (1973).
20. N. Brousseau and H. Arsenault, Appl. Opt. **14**, 1679 (1975).
21. T. Luu and D. Casasent, Appl. Opt. **18**, 791 (1979).
22. K. Preston, Jr., *Coherent Optical Computers* (McGraw-Hill, New York, 1972).
23. K. von Bieren, Appl. Opt. **12**, 1642 (1973).
24. D. Casasent and T. Luu, Appl. Opt. **17**, 2973 (1978).

CHAPTER 3

PHOTO-DKDP SLM STUDIES

202-14

New birefringence theory and used of the photo-DKDP spatial light modulator in optical data processing

D. Casasent, S. Natu, and T. Luu

Department of Electrical Engineering, Carnegie-Mellon University
Pittsburgh, Pennsylvania 15213

G. Lebreton and E. DeBazelaire
Gessy, University of Toulon, France

Abstract

The photo-DKDP spatial light modulator is found to be an excellent candidate real-time and reusable 2-D optically-addressed spatial light modulator. Extensive sensitometry, MTF, and other device data are reported with emphasis on a new field dependent photo-sensitivity and the importance of linear MTF data. A new spatial birefringent modulation transfer function is described and its use in obtaining more linear device response, bias level suppression, phase modulation and 1 msec erase time are noted. New real-time image processing, optical pattern recognition, and optical signal processing applications of this SLM are described with emphasis on the accuracy of the photo-DKDP based real-time experiments.

1. Introduction

The photo-DKDP spatial light modulator (SLM) has been in existence for six years. It is a most promising real-time and reusable 2-D optically addressed SLM for coherent optical data processing. Although it is basically well understood and extensively documented,[1-4] many details of its sensitometry and MTF data require additional description. These new issues include a charge carrier description of the device (Section 3), the importance of the $\mu\tau$ product and voltage dependent sensitometry of the Se photo-conductor on charge generation in the device (Section 4), and its linear gray scale MTF and use of the proper MTF data acquisition techniques (Section 5). Other SLM performance specifications such as storage, optical quality, and scatter level are noted in Section 6. A new polarization description of the spatial birefringent modulation in this SLM leads to new and more linear device response and to new write and erase methods with the ability to suppress input bias levels and achieve erase times below 1 msec (Section 7). These new photo-DKDP device physics and device operation issues are followed by the highlights of several new application experiments performed using this SLM (Section 8). These include image subtraction, optical pattern recognition, and optical signal processing, with emphasis on comparison of film based and theoretically expected results to real-time experimentally obtained ones.

2. Device construction and operation

The photo-DKDP SLM is shown schematically in Figure 1 and detailed fabrication issues are included in Table 1. The general operation of this device is well-known,[1-4] but it summarized here for completeness. The SLM is optically-addressed by a spatially modulated input light distribution or a sequentially modulated scanning light pattern. The device is written on in λ_W light (usually 440-514nm) from the Se photo-conductor side and read and reflection in λ_R light (usually 633nm) from the DKDP side. In its normal mode of operation, the readout light I_I is linearly polarized along the y axis (at 45° to the crystal's induced x' and y' electro-optic axes). The modulated readout light intensity I_O is monitored through a crossed linear polarizer oriented along the x axis.

Table 1. Fabrication of the photo-DKDP SLM

Component	Specification
E_1	Gold
Se	12μm, n = 2.8 at 633nm, ε = 6
M	9 layers λ/4 of CaF_2 and ZnS. T_R = 0.985 and T = 0.001 at 633nm
DKDP	Wedged (320-0μm), 35x28mm², ε_c = 650 and $V_{\lambda/2}$ = 300v at $\Gamma - T_C$ = 0.5° and 633nm
E_2	In_2O_3, T_T = 0.98, T_R = 0.01, T_A = 0.01 at 633nm
Substrate	CaF, wedged (6 - 5.17 mm), 1°30'
Readout window	SiO_2, wedged 3°

Casasent 1

After writing, a spatial voltage distribution V is produced across the DKDP layer proportional to the spatial write light input distribution I_i. By the Pockels effect, the output light intensity I_0 (through a crossed polarizer) is related to the applied voltage by[5]

$$I_0 = I_i \sin^2[(V/V_{\frac{1}{2}})\pi] , \tag{1}$$

where $V_{\frac{1}{2}}$ is the crystal's halfwave voltage. The DKDP is held at its Curie temperature of approximately -52°C by Peltier cells around the circumference of the device. This decreases the halfwave voltage to approximately 300 volts and greatly improves the device's resolution, uniformity and storage properties.[2,6,7]

3. Charge carrier description

A description of the operation of the photo-DKDP SLM in terms of the hole and electron charge carriers is necessary to fully analyze and describe the sensitometry, readout, and erase operation of this SLM. Such a description has not previously been provided and in fact the applied voltage polarity noted in many of the papers describing this SLM are conflicting. In Figure 2, we show the voltage distribution (vertical) vs. distance (horizontal) across the various device layers for the four different states of device operation for both bright (BR) and dark (DK) (illuminated and non-illuminated) regions of the device.

Initially, $+V_0$ is applied (with E_1 positive). With no $I_{\lambda W}$, the voltage distribution is as shown in Figure 2a (most of the applied V_0 appears the Se photo-conductor layer). When the Se photo-conductor is illuminated with λ_W light, hole and electron charge carriers are generated. With $E_1 = +V_0$, the holes conduct and move to the mirror M, decreasing the voltage at M and increasing the voltage drop across the DKDP in BR areas (see Figure 2b). When the electrodes E_1 and E_2 are shorted ($V_0 = 0$), a large $+V_1$ appears across the DKDP in BR areas and a smaller $+V_2$ in DK areas. With crossed output polarizers, a positive output image results. During readout, no major carrier conduction occurs because M blocks the λ_R light and the Se is much less sensitive to the λ_R wavelength light that leaks through M. For erasure, the Se side of the SLM is uniformly flooded with λ_E light (in the wavelength region λ_W) with $V_0 = 0$. This λ_E illumination generates holes and electrons in the Se. This causes the holes trapped at M during writing to migrate back to E_1; equivalently, the electrons at E_1 can migrate to M. Both processes decrease the positive V_1 voltage at M and thus remove the writing charge stored there.

We term the above process positive writing. Writing with $-V_0$ on E_1 is also possible and is refered to as negative writing. The charge carrier description of operation is similar for this case. We note that in positive writing, writing is by hole conduction and erasure by electron conduction. Conversely, in negative writing, writing is by electron flow and erasure is by hole flow. This is of concern since hole conduction is better than electron conduction in Se. A new feature of this SLM that we will discuss in Section 4 is the increase in the conduction efficiency and photo-sensitivity of the Se when a field is present across the Se. These and other issues contribute to the reasons for the new write and erase schemes to be described in Section 7. The different fields present across the Se in the different cases (Figure 2) are thus of importance when analyzing the different device operating modes. For readout, 0V is preferable for best contrast. To see this, attention should be given only to the DK regions and the degrading effects of λ_R light leakage through M should be considered. For long term dark storage, application of $+V_0$ to E_1 (after writing with $+V_0$ on E_1) appears preferable.

4. Sensitometry effects

4.1 Sensitometry

Sensitometry data is the first information necessary for an optically addressed SLM. In Figure 3 we shown sensitometry data obtained for positive and negative writing on photo-DKDP. These data were obtained using a constant $I_{\lambda W} = 18 uW/cm^2$ illumination from an argon laser with $\lambda_W = 514nm$ and a low $I_{\lambda W} = 20 uW/cm^2$ readout light intensity. A low $E_T = 0.5 uJ/cm^2$ threshold was observed for both cases with a far lower exposure needed to reach 80% saturation for positive writing ($E_{0.8} = 75 uJ/cm^2$) than for negative writing ($290 uJ/cm^2$). From these data, we also find the dynamic range of the device to be 560/0.5 or above 1000:1 and its contrast ratio to be above 100:1. The superior sensitivity obtained for positive writing is due to the better hole condition in Se. In the photo-DKDP, the image is stored in the photo-conductor. This is contrary to the case of operation of the LCLV[8] and other SLMs. We now discuss the Se photo-conductor in some depth.

4.2 Quantum efficiency

The quantum efficiency η with which photo-carriers are generated in Se depends on the field E across the Se according to[9,10]

$$\eta = \eta_0 \exp[-E_0/kT + B_0 E^{\frac{1}{2}}/kT] , \tag{2}$$

where η_0, B_0, and E_0 are constants and T is temperature. The initial field across Se is approximately 100v. For a 10um Se layer, the field is $10^5 V/cm^2$ and $\eta \approx 20\%$. However, our present concern lies in the fact that during a long writing exposure, the voltage across the Se decreases. Thus, photo-electric conversion in Se will be better for the initial portion of exposure (when a large E exists) then for latter parts of the exposure (when E is less).

Comment 2

4.3 Charge carrier effects

Next we consider the charge transfer efficiency R in Se. This is proportional to

$$R = \tau/t_R = \mu\tau(V/d^2) \ , \tag{3}$$

where τ is the lifetime and t_R is the transit time of the charge carriers. For a Se of thickness d, the drift velocity is $v = \mu V/d$ and $t_R = d^2/\mu V$ from which (3) results. For d = 10μm, t_R = 0.5μsec for holes and a far larger 100μsec for electrons as noted earlier.

From (3), we see that R increases with V (recall from (2) that η also increased with V). Thus, we expect better sensitivity in the photo-DKDP for short exposures than for long ones. Moreso, static sensitometry tests (such as the ones presented in Figure 2) using long T_W exposure times will yield different results (inferior to those obtained dynamically with short T_W exposure times). Thus, proper SLM test and evaluation procedures are important because of the voltage dependent sensitometry of the Se photo-conductor used.

4.4 μτ product

For exposure times larger than the transit times, charge q is accumulated at M as

$$q = (N_0 eV\mu\tau/L^2)[1-\exp(-t)] \ . \tag{4}$$

For large T_W, the exponential term is zero and q is proportional to the μτ product. For holes, this is $1.3\times10^{-6}cm^2/V$, whereas for electrons it is four times less or $3.2\times10^{-7}cm^2/V$. We thus expect holes to be more efficient than electrons during writing and hence positive writing to be better than negative writing. From Figure 3 at low T_W = 0.3sec, we find a 4:1 difference in sensitivity between positive and negative writing (in excellent agreement with the predicted values). For longer exposures, the difference is less, thus indicating a field and carrier dependence for η and the μτ product.

4.5 Instituo image subtraction and addition

One of the new applications of this SLM with which we are concerned is the subtraction of two frames of data for purposes of edge enhancement preprocessing[11] and for image registration for track assembly analysis.[12] The different sensitivity for hole and electron conduction and the field dependent sensitometry of this SLM are of practical concern in such interframe operations. The factor of four difference in the μτ product of the charge efficiency has been noted by others.[9,10] The solution to this problem is first the use of low exposure times, thereby decreasing the time dependence of sensitometry on the time varying field across the Se. In Figure 4, we show the transmittance vs. exposure curves for DKDP for various μτ products.[1] These curves indicate that by properly doping the material to obtain μτ products in the range of 3×10^{-7}-10^{-5}, μτ variations by even a factor of 10 will have little effect on transmittance. With the much smaller 3×10^{-7}-10^{-8} μτ products in our photo-DKDP SLM, small μτ differences result in large transmittance differences as seen in the lower curves of Figure 4.

5. Modulation transfer function (MTF)

5.1 Introduction

The resolution of any SLM is one of the parameters of utmost concern. As we have noted:[13-15] (1) unnormalized MTF data is preferable to better convey true device performance and to better compare different SLMs, (2) interferometric MTF data is more reliable and preferable, (3) linear MTF data is vital when accuracy is of concern, (4) voltage dependent sensitometry effects must be considered in properly selecting bias levels for MTF experiments, (5) the depth-of-focus of the optics and associated addressing system used in practice must be compatible with those used during the MTF data acquisition experiments. In this Section, we briefly describe these five issues and include our MTF data obtained on the photo-DKDP together with its comparison to the theoretically expected results.

5.2 MTF techniques

An MTF curve is a plot of contrast ratio vs. spatial frequency. As noted,[13] the use of unnormalized MTF data ($m = m_{out}(u')$ vs. u' rather than $m_{norm} = m_{out}(u')/m_{out}(0)$ vs. u') is preferable for more valid comparison between SLMs. A constant 100% input modulation is assumed and the exact test conditions must be noted. Care should also be taken to obtain at least three approximately constant low u' m_{out} values before ceasing data acquisition. From a two year program involving first-hand experiments on many SLMs, we have found interferometric MTF data to be far more reliable and useful than any other form of SLM resolution measurement. Because the interferometric pattern is in focus over the entire thickness of the SLM, operator errors are greatly reduced. In addition, by restricting the input modulation, monitoring the (I_0), first (I_1) and second (I_2) order terms in the Fourier transform pattern, second harmonic distortion can be controlled and gray scale and linear MTF data can be obtained. As noted in Section 4, when voltage dependent sensitometry effects are present, the sensitometry and MTF experiments must be conducted similarly to properly determine the corresponding bias level to be used. In Sect. 7, the new Bessel transfer function derived for this SLM indicates the origin of the harmonic distortion.

5.3 Depth-of-focus effects

The first major shortcoming of interferometrically obtained MTF data is its applicability to different SLM uses, such as when the input data is scanned or imaged onto the SLM in practice. Specifically, the lens system and data recording technique actually used must have the depth-of-focus and focusing accuracy of the interferometric recording method if the results of the MTF experiment are to be of use. Interferometric MTF data yields the largest possible SLM resolution; whether this resolution and performance are obtainable in practice depends upon the optical system and addressing method employed.

If the photo-conductor in the SLM is d μm thick, the associated imaging lens must have a depth-of-focus above d μm. The spatial frequency limit for such a system is[16] $f_L/D \cdot \delta f_L$ cy/mm. Conversely, if the depth-of-focus of the lens used is d_L, then d_L should be less than d μm and MTF data beyond the same ν_{max} limit noted above should not be used. This brief discussion assumes that the photo-conductor is active throughout its entire volume and thickness and ignores photo-conductor response variations normal to the optical axis. The depth-of-focus of a lens of focal length f_L and aperture D used at a wavelength λ is

$$\delta f_L = 8\lambda(f_L/D)^2 \ . \tag{5}$$

The uncertainty in the location of the focus in the plane normal to the optical axis is

$$\delta y = (\lambda/4)(f_L/D) \ . \tag{6}$$

The corresponding spatial frequency at which problems will be encountered in the use of such a lens is

$$\nu_{max} = 1/(2\delta y) \ . \tag{7}$$

With properly selected lenses used in the actual recording system, these problems can be avoided. For the photo-DKDP, lenses with $f_L/D = f\# = 1.4$ allow us to reach a spatial frequency limit of $\nu_{max} = 2200$cy/mm. The above analysis has assumed diffraction limited systems and clearly other system aberrations will dominate such a process before this limit is reached.

5.4 MTF data

Interferometric MTF data were obtained on the photo-DKDP with a bias exposure point in the central linear region of the sensitometry curve chosen (see Figure 3). Input modulation was increased while monitoring I_0, I_1, and I_2. I_2 was kept 20dB below I_1, thus insuring less then 1% interharmonic distortion. The resultant I_1/I_0 measured values vs. u' were converted to output amplitude modulation using[13]

$$m_{out} = \frac{4(I_1/I_0)^{\frac{1}{2}}}{1 + 4I_1/I_0} \ . \tag{8}$$

The MTF curve of Figure 5 results. From it, we find a maximum modulation of 90% and a resolution at 50% of the peak modulation of 16cy/mm. Note that this MTF data includes gray scale and linear recording issues and applies for less than 1% distortion.

5.5 Comparison to theory

Roach[17] and others[18,19] have analyzed the resolution of such SLMs. They have solved the Laplace Equation in the DKDP, M, and Se regions subject to the correct boundary conditions and assumed a surface charge density σ of unity and spatial frequency ν

$$\sigma = \sigma_0 \cos 2\pi\nu x \ . \tag{9}$$

They found the resultant voltage across the DKDP to be

$$V = V_2(\nu) \cos 2\pi\nu x + \text{Bias} \tag{10}$$

where

$$V_2(\nu) = \frac{\sigma_0/2\pi\nu\varepsilon_0}{(\varepsilon_z/\varepsilon_x)^{\frac{1}{2}} \operatorname{Coth}[(\varepsilon_x/\varepsilon_y)^{\frac{1}{2}} 2\pi\nu a] + \varepsilon_0 \operatorname{Coth}(2\pi\nu b)} \ , \tag{11}$$

in which a is the thickness of the DKDP and b is the thickness of the mirror. From (11), we see that $V_2(\nu)/V_2(0)$ decreases as ν increases. A plot of V_2/V_0 vs. ν is the amplitude modulation or MTF. The corresponding theoretical curve is shown in Figure 6. It is seen to be in excellent agreement with the experimental curve obtained in Figure 5.

6. Other photo-DKDP tests

6.1 Introduction

In the following Subsections, we describe several additional tests performed on the photo-DKDP SLM.

6.2 Dark storage

The dark storage of the photo-DKDP ($I_{\lambda R} = 0$) is determined by the time constants of the Se and the DKDP[1,20]

$$\tau_{Se} = 53\text{sec}, \ \tau_{DKDP} = 2671\text{sec} . \tag{12}$$

Using an RC model for the photo-DKDP, we find an expected dark DK time constant of τ_{DKDP}. Since intensity is measured in all experiments and since $I \propto V^2$ at low V, the measured time constant is expected to be $\tau/2 = 1335$ sec. Experimental data obtained by recording a 5cy/mm squarewave pattern on the DKDP and measuring the I_0 and I_1 Fourier components vs. time confirmed the theoretical predictions. I_0 and I_1 were found to decay at the same rate indicating that dark storage decay results in a loss of charge and hence output light without a loss of definition or modulation (I_1/I_0). The measured dark decay time constant was $\tau = 1500$sec, in good agreement with the predicted value of 1335sec. For longer storage times, an alternate model is necessary.

6.3 Readout decay

Under readout ($I_{\lambda R} \neq 0$) the stored pattern is expected to decay faster and differently than under dark storage. Using $I_{\lambda R} = 50\text{uW/cm}^2$, the decay time constants for the zero-order τ_0 and first-order τ_1 Fourier terms were measured to be

$$\tau_0 = 1400\text{sec}, \ \tau_1 = 1100\text{sec} . \tag{13}$$

These values are less than the dark storage decay time constants as expected, but are still quite long. Since $\tau_1 < \tau_0$, we see that the modulation (I_1/I_0) of the recorded data decreases under readout (only by about 10%), whereas it remained constant under dark storage. Thus, we conclude that no appreciable readout error effects will arise and that long 15min times are acceptable with this SLM.

6.4 Erase time

Erase time in our experiments were much longer (4sec using a broadband 8mW/cm^2 arc lamp λ_E source). This was due to the voltage dependent sensitometry noted earlier, to the low $I_{\lambda E}$ intensity available and to the broadband nature of the λ_E source used. Erase times of 1msec are possible with alternate techniques as we describe in Section 7.

6.5 Optical path difference

The optical quality of an SLM is of concern in coherent optical data processing applications. The wedge present in the DKDP, the non-uniform temperature of the target, and the optical quality of its surface limited the rms OPD phase quality of the photo-DKDP unit we tested. Over its central $2\text{x}2\text{cm}^2$ area, the phase error was $\lambda/4$. Interferometric tests are usually used to obtain such data, although point-by-point OPD information is more useful in estimating the effects of such OPD errors on system performance.[21,22]

6.6 Scatter level

The scatter level of an SLM is another factor that limits the processing gain obtainable using it and its ability to process signals with low SNR. To obtain scatter level data on the photo-DKDP, a $7\text{x}7\text{mm}^2$ input aperture was used. The Fourier transform pattern for this input was scanned with all components in place (except the photo-DKDP itself) and a scatter level or optical system maximum dynamic range of 52dB was measured. The same experiment was repeated with the input aperture imaged onto the photo-DKDP. The observed scatter level was 50dB. Thus, use of the photo-DKDP in coherent optical data processing systems appears to be most excellent and should introduce less than 2dB of noise.

7. New formulations of spatial birefringence and operation

7.1 Introduction

G. Lebreton and E. de Bazelaire at Gessy Laboratories of the University of Toulon have considered the operation of the photo-DKDP SLM in depth. A new transfer function for the device with attention to its polarization effects has been produced (Section 7.2), and has resulted in an improved response linearity (Section 7.3) and was experimentally verified (Section 7.4). The diffracted light from such a device was shown to be of constant polarization independent of the input modulation or spatial frequency. This formulation also resulted in new write and read methods (Section 7.6) with the ability to suppress the input bias level (Section 7.5) and achieve faster (≈1msec) erase times. The intent and application of this device being considered in France is as the real-time input transducer for radar and sonar signal processing applications.

The classic approach[5,16] to the analysis of the spatial birefringent modulation of the photo-DKDP uses particular cases of the well-known amplitude and phase modulation. However, a complex analysis[23] involving an extensive study of the effects of polarized light in this SLM and experiments performed using an ellipsometer provided several new results which indicate that modifications to the traditional description of the spatial birefringent modulation in the photo-DKDP and other SLMs are in order. These results are summarized below and discussed in subsequent Subsections.

(1) In a Poincare sphere description,[24] the diffracted light is a symmetric version of the undiffracted light with respect to the birefringent axis of the modulating crystal. This theory[25] was verified by experiment.[26] A particular case of the above theorem follows in (2).

(2) When the Poincare sphere representation of the incident light lies on the circle normal to the crystal's birefringent axis, the polarization of the diffracted light is orthogonal to that of the input light.[27] The conclusion is that when properly oriented linearly polarized incident light is used, the polarization of the diffracted light will be linear and orthogonal to the polarization of the incident light and to the polarization of the zero-order diffracted light. This effect has also been observed in shear mode acousto-optic SLMs[28] and in BSO.[24]

(3) The polarization of the diffracted light noted in (2) is independent of the amplitude and spatial frequency of the input modulating signal. Only the angle of diffraction depends on the input spatial frequency.

(4) The amplitude of the diffracted light is described by a Bessel function (as in conventional phase modulation), and not by the classic crossed polarizer modulation expression.

(5) This leads to a new transfer function with improved output linearity and to new write and read modes of operation for the SLM.

7.2 New spatial birefringence transfer function

We can view the incident readout light to be propagating in the z direction with equal electric field vectors in the (x,y) plane. Elliptical polarization can be described by linearly polarized orthogonal components A_x and A_y on the fast and slow electro-optic axes of the crystal.

$$A'_x(x,y) = A_x \exp[j\phi_x(x,y)] \tag{14a}$$

$$A'_y(x,y) = A_y \exp[j\phi_y(x,y)] \ . \tag{14b}$$

Since any spatial modulated signal can be represented (along x and y) by a Fourier integration and since optical Fourier transform systems are linear, we restrict attention to one sinusoidal component of the signal with amplitude a, bias level V_0 and spatial frequency f_0. The voltage across the DKDP for such a signal is

$$V(x) = (a/2)V_0 \sin(2\pi f_0 x) \tag{15}$$

and the corresponding phase modulation terms in (14) are

$$\phi_y = -\phi_x = (\pi/\lambda)n_0^3 r_{63}(a/2)\ V_0 \sin(2\pi f_0 x) = (\phi/2) \sin(2\pi f_0 x) \ . \tag{16}$$

The A' terms in (14) can then be expressed as a series of Bessel functions J_n of the first kind. Since J_0 is an even function and all other J_n are odd, the total diffraction pattern (after filtering of harmonic frequencies) can be described by

$$[A'(f_x)] = (A_x+A_y)\{J_0(\phi/2)\ \delta(f_x) + (A_x-A_y)\{J_1(\phi/2)\ [\delta(f_x-f_o) + \delta(f_x+f_o)] + \ldots\} \tag{17}$$

From (17) we see that: (1) the polarization of the zero-order diffracted pattern (first term) is the same as the polarization of the incident light. We also see that: (2) the polarization of the first-order diffracted or modulated light (second term) has a polarization that is symmetric with respect to the polarization of the incident light with respect to the birefringent axis in a Poincare sphere description of the process, (3) the input spatial frequency affects only the angle of diffraction, and that (4) the amplitude of the diffracted light is related to the input by Bessel functions as in the classic phase modulation case.

7.3 Linearity of response

From (17), we see that the amplitude of the diffracted light is related to the phase by Bessel functions $J_n(\phi/2)$ rather than by the conventional $\sin(\phi/2)$ equation. This new transfer function implies that the actual linearity of the device is far better than one would expect using classic relationships. $\Delta\phi$ linearity error for the two transfer functions is summarized in Table 2 (the phase value noted is the total delay between both components of the input wave).

Table 2. Linearity of ϕ for $\sin(\phi/2)$ and $J_n(\phi/2)$ Modulation

ϕ	$\pi/3$	$2\pi/4$	$\pi/2$	$2\pi/3$	π
% linearity in $\Delta\phi$, $J_1(\phi/2)$ Modulation	1%	2%	3%	7%	22%
$\sin(\phi/2)$ Modulation	2%	4%	8%	18%	57%

7.4 Ellipsometer experiments

From Table 2, we see that the new transfer function indicates far better linearity in response of this SLM than did prior classic formulations. Such excellent linearity is vital in the use of this SLM in signal processing applications. Such differences are not usually observed experimentally with small angle modulations since they appear only in the third-order of a Taylor series expansion of the 2 functions. In the normal experiments performed with cross polarizers, the input polarization is not always linear and only the projections of the modulated elliptically polarized output signal on two orthogonal axes can be measured. Since many elliptical polarization outputs can yield similar projection data, accurate analysis of the modulation obtained is not possible. To experimentally verify the remarks advanced in Section 7.2, an ellipsometer was constructed using a rotating $\lambda/2$ plate and a fixed linear polarizer. This allowed the ellipticity and orientation of the axes of the ellipse to be accurately determined. The variable birefringence of the photo-DKDP was measured without spatial input modulated signals for different bias voltages from ± 160 volts with a saturated input illumination level. The time of exposure was also varied for ± 150 volt bias levels with constant $I_{\lambda W}$ power used. From direct measurements with circularly polarized input light, the exact angle $\theta + \pi/4$ in the Poincare sphere model was determined. More accurate measurements were then performed with the input light linearly polarized at 45° to the crystal's birefringent axes. From these data, the ellipticity was determined. No intermediate optical system was used to avoid parasitic birefringence effects.

The performance of the photo-DKDP with spatially modulated input light is quite different and is not directly describable using the same Poincare sphere description. Tests performed with a 100 μm period Ronchi ruling and vertically polarized readout light showed the polarization of the zero-order to be vertical and that of the higher order terms to be horizontal (independent of the depth-of-modulation of the input). This verifies the theory advanced in Section 7.2. In the above experiments, the bias level of the input signal was cancelled as explained in Sections 7.5 and 7.6. When this was not done, the polarization of the zero-order spot was elliptical and related to the depth-of-modulation of the input signal by the Poincare sphere model.

7.5 Input bias level suppression

Several authors[29] have noted that a suppression of the zero-order diffracted light can be obtained by illuminating the SLM with a uniform light distribution equal to the average amplitude of the image with the opposite polarity V_0 applied to the crystal. Since the zero-order diffracted light is described by

$$A_0 = \delta(f_x)[A_x \exp(-j\phi/2) + A_y \exp(j\phi/2)] \ , \tag{18}$$

and since the polarization of this term is different from that of the diffracted light (Section 7.2), it cannot be fully cancelled (using cross-polarizers) by the indicated second uniform exposure.

7.6 New write, erase, and bias level suppression operation

New erase and write modes of operation are necessary to achieve optimum performance in this SLM. These are suggested by the new polarization formulation advanced in Section 7.2. All results have been experimentally verified. The technique used is to write the original image with $+V_0$ applied to E_1 as before. During erasure, the applied voltage to E_1 is reversed to $-V_0$ and a strong erase photo-flash is applied. This causes the voltage at M due to BR and DK areas of the crystal to both saturate to the <u>same</u> large negative V_1 value. Of concern and note is the fact that both the DK and BR crystal regions now have the same voltage value at M and that this value is a constant for all cases and independent of the image used. When a new image is recorded with $+V_0$ applied, an input bias illumination level equal to the constant saturation level V_1 present is used. This results in the recording of a zero mean pattern on the photo-DKDP and full use of the phase modulation theory described in Section 7.2. This new write and erase procedure avoids the multi-step process previously employed, fully cancels the bias level of the input data, and allows faster erase time and cycle times for this SLM and results in the full use of the Bessel phase function modulation features noted in Section 7.2 with their associated other advantages.

8. Applications

8.1 Introduction

The purpose of any SLM is to serve as the real-time and reusable transducer for diverse optical computing applications. In the following Subsections we briefly summarize several of the new applications to which we have applied the photo-DKDP SLM. These data are more fully described in [14]. They are of particular

interest because of the comparison between theory and experiment and between the use of film inputs and real-time SLMs.

8.2 Edge enhancement preprocessing and image registration for track assembly

Edge enhancement preprocessing is a useful step in the correlation of multi-sensor imagery.[11] By exposing the photo-DKDP to two successive patterns with different polarities of applied voltage present between each exposure, the subtraction of the two 2-D images results. This is also of use in image registration for track assembly.[12] If the two images are defocused versions of the same image, the resultant difference image is an edge-enhanced version of the original one. This operation is of use in preprocessing for multi-sensor image pattern recognition. Initial tests on the use of the photo-DKDP SLM for both of these operations[14] have been most promising.

8.3 Optical pattern recognition

The input, reference and output correlation patterns obtained using the photo-DKDP SLM as the input plane transducer in a conventional matched spatial filter frequency plane correlator are shown in Figure 7. The location of the output correlation peak is seen to be proportional to the location of the reference function within the input scene. We have experimented with the use of this technique and the photo-DKDP SLM in missile guidance and optical word recognition (OWR) applications. An OWR experiment in which there were 4 occurences of the reference word was repeated using inputs on both film and on the photo-DKDP. The resultant I_p values for the four output correlation peaks were 30, 28, 28, 27 when the photo-DKDP was used and were remarkably similar, 37, 34, 32, 29 when film inputs were used. The widths of the output correlation peaks in this OWR example were also compared. The theoretical width was computed to be 63 um. The width obtained using the photo-DKDP inputs was 90 um, whereas 60 um widths resulted when film inputs were used. The low modulation of the photo-DKDP at the stroke width of the characters used appears to be the source of the larger correlation peak widths obtained using the real-time transducer.

8.4 Optical Signal Processing

The output correlation pattern obtained using photo-DKDP in a crossed input ambiguity function processor is shown in Figure 8 for a simple double-pulse signal. The width in doppler of the optically produced outputs were seen to be 0.173 mm (versus a theoretical 0.17 mm value). The width in range of the output was 7.25 mm (versus a theoretical 7.20 mm value). The peak to side lobe ratio measured was 4.3 (versus a theoretical value of 4). These experimental results were thus in excellent agreement with those predicted by theory. Similar excellent performance was obtained when the photo-DKDP was used as the real-time SLM in a passive ambiguity surface detection application[14] and in correlations of active sonar signals.[25]

Acknowledgments

The support of the AFOSR (Grant AFOSR-75-2851) and the Office of Naval Research (Contract NR-366-005) and Gessy (University of Toulon) for the research reported upon here is gratefully acknowledged.

References

1. Donjon, J., et al., IEEE, ED-20, 1037 (1973).
2. Marie, G. and Donjon, J., Proc. IEEE, 61, 942 (1973).
3. Dumont, F., Hazan, J., and Rossier, D., Phillips Technical Review, 34, 274 (1974).
4. Marie, G., et al., Chapter in Advances in Image Pickup and Display Devices, (B. Kazan, ed., Academic Press, New York, May 1974), pp. 225-302.
5. Billings, B. H., J. Optical Society of America, 39, 797 (1949).
6. Casasent, D., IEEE, ED-20, 1109 (1973).
7. Casasent, D. and Keicher, W., J. Optical Society of America, 64, 1575 (1974).
8. Bleha, W., et al., Optical Engr., 17, 371 (1978).
9. Hartke, J. L. and Regensburger, P. J., Physics Review, 139, A970 (1965).
10. Pai, D. M. and Ing., S. W., Jr., Physics Review, 173, 729 (1968).
11. Casasent, D. and Munoz, D., SPIE, 201 (1979).
12. Wald, L., et al., SPIE, 207 (1979); Casasent, D., et al., SPIE, 201 (1979).
13. Casasent, D., Applied Optics (July 1979).
14. Casasent, D. and Luu, T., Applied Optics (September 1979).
15. Casasent, D., et al., BMDATC Report on Contract DASG60-78-C-0054 (April 1979); Casasent, D., et al., ETL Report on Contract DAAK70-78-C-0076 (June 1979).
16. Born, M. and Wolf, E., Principles of Optics, (McMillan, New York, 1964), pp. 436-440.
17. Roach, W., IEEE, ED-21, 453 (1974).
18. Donjon, J., et al., Acta. Electronica, 18, 187 (1975) (French).
19. Marie, G., Ferroelectrics, 10 (1976).
20. Tabak, M. and Warter, P., Physics Review, 173, 899 (1968).
21. VonBieren, K., Applied Optics, 12, 1642 (1973).
22. Luu, T. and Casasent, D., Applied Optics, 18, 791 (1979).
23. De Bazelaire, E., Ph.D. Thesis, CNRS A010522, Paris (1974).
24. Herriau, J., et al., Applied Optics, 17, 1851 (1978).
25. Lebreton, G., et al., IOCC, 101 (London, 1978).

26. Lebreton, G., Ph.D. Thesis, Orsay, 2390 (1978).
27. De Bazelaire, E. and Lebreton, G., Coll. GRETSI, Nice (1977), p. 80/1-5.
28. Dixon, R. W., IEEE, OE-3, 85 (1967).
29. Hazan, J., Acta. Electronica, 18, 201 (1975).

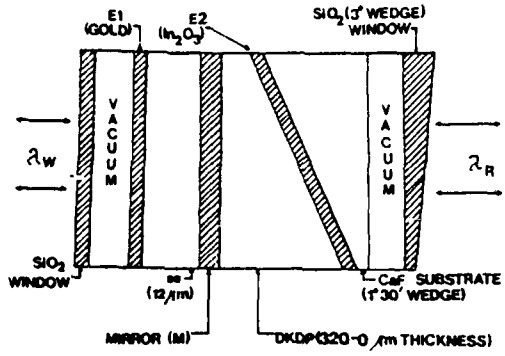

Figure 1. Schematic diagram of the photo-DKDP spatial light modulator.

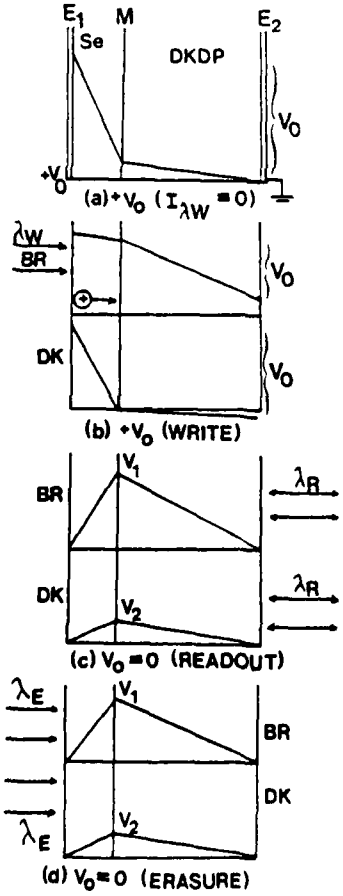

Figure 2. Voltage versus distance distribution in the photo-DKDP SLM at different steps of operation and for a bright (BR) and dark (DK) (illuminated and unilluminated) regions.

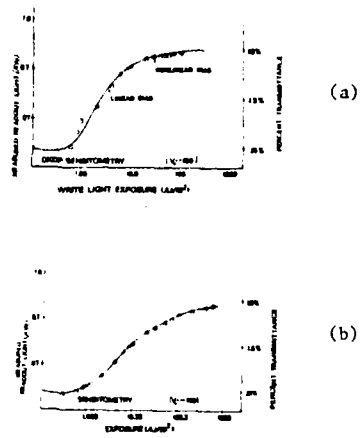

Figure 3. Sensitometry data for the photo-DKDP SLM.
(a) Positive writing with $+V_0$ applied to E_1 during writing;
(b) Negative writing with $-V_0$ applied to E_1 during writing.

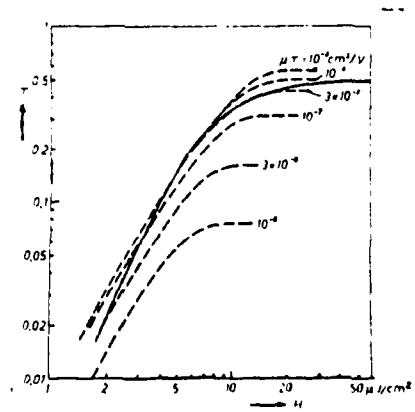

Figure 4. Transmission versus exposure for the photo-DKDP SLM for different μτ carrier products.[1]

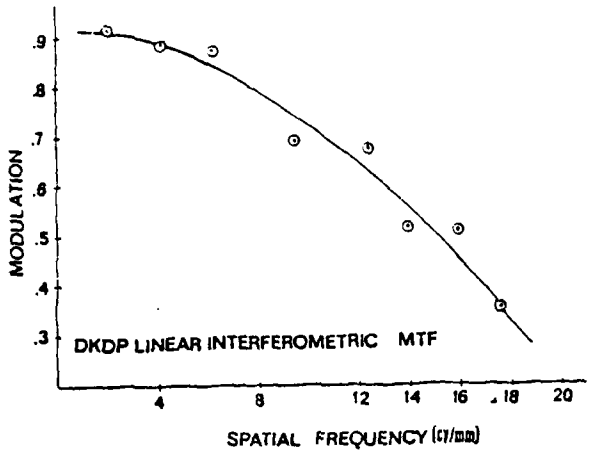

Figure 5. Experimental nonlinear MTF (unnormalized) for the photo-DKDP SLM including gray scale and with less than 1 percent harmonic distortion.

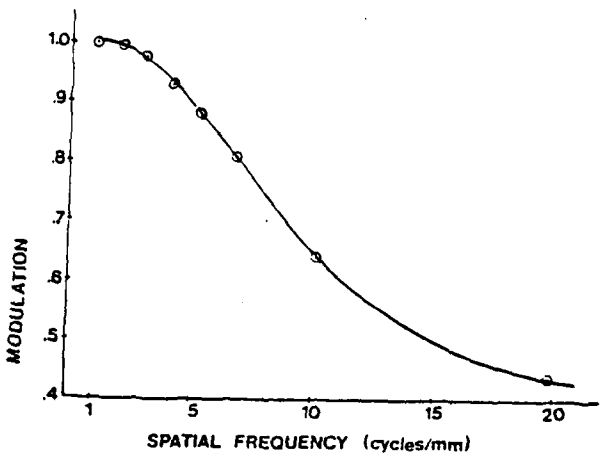

Figure 6. Theoretical MTF curve for the photo-DKDP SLM.

(a)

(b)

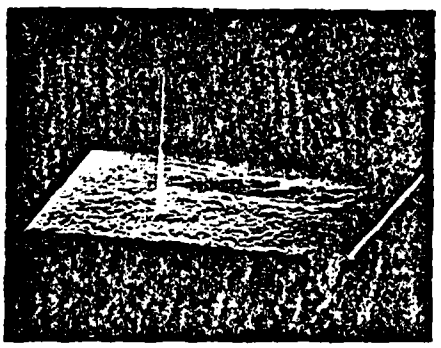

(c)

Figure 7. Real-time optical pattern recognition using the photo-DKDP SLM. (a) Input; (b) Reference; (c) Output correlation pattern.[14]

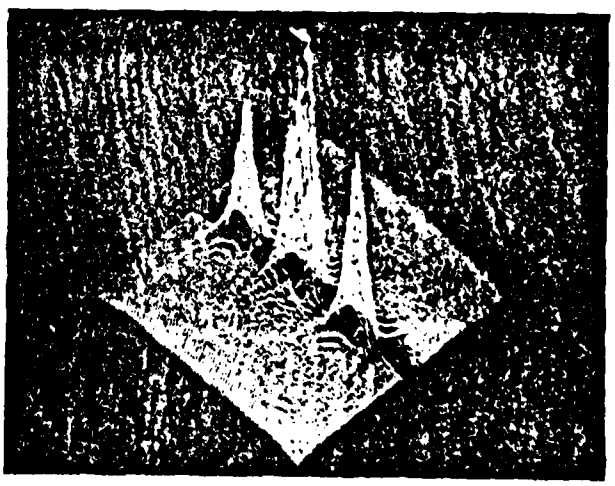

Figure 8. Real-time optical signal processing using the photo-DKDP SLM as the input transducer for a crossed input ambiguity function processor.[14]

CHAPTER 4

HYBRID OPTICAL/ELECTRONIC PROCESSOR

Reprinted from APPLIED OPTICS, Vol. 17, page 3418, November 1, 1978
Copyright 1978 by the Optical Society of America and reprinted by permission of the copyright owner.

Equalizing and coherence measure correlators

David Casasent and Alan Furman

A correlator is described that combines optical and electronic processing. The optical section is the first Fourier transform taking stage of a joint transform correlator; its output is electronically processed by a modified spectrum analyzer. Increased flexibility and various processing operations beyond those normally possible in an optical system result.

I. Introduction

The importance of the correlation operation in image and signal processing is well accepted. Many diverse optical correlator systems have been devised,[1-7] beginning with the holographic matched filter correlator,[1,2] that enable this correlation operation to be performed in parallel on 2-D imagery or multichannel 1-D data and at high throughput rates. The basic optical system which we chose to modify is the joint transform correlator (JTC).[3-5] Rau[6] had previously suggested detection of the joint transform of two functions (placed side by side in the input plane) by a vidicon camera. A spectrum analyzer was applied to the camera's video signal, yielding the correlation of the two inputs in a demonstration of optical character recognition. In temporal offset correlation, Macovski and Ramsey[7] devised a method whereby a video signal equivalent to the above one was produced by transforming the coherent superposition of the two images (fully overlapping) after having frequency-shifted the light used to illuminate one of the images. The transform plane intensity then contains a temporal ac term composed of a carrier (at the shift frequency) modulated by the complex transform product. Since the width of the input format is reduced typically by a factor of 3, the transform plane detector spatial resolution required is reduced proportionally; however, because an ac (in time) intensity distribution must be detected, a nonintegrating (e.g., image dissector) detector must be used.

In the system to be described herein, the joint transform detection system is modified, and an equalizing correlator produced that enables compensation of various types of signal distortions to be realized. A theoretical description (Sec. II) of the electronic readout joint transform correlator and experimental demonstrations of it (Sec. III) are followed by similar sections for the equalizing correlator (Secs. IV and V). We conclude with a discussion of other extensions of this system including a coherence measure operation (Sec. VI).

II. Electronic JTC Readout; Theoretical

The conventional joint transform correlator[3-5] is reviewed first. In this system, the two functions f and g to be correlated, both assumed to have a width of b, are placed side by side in the input plane P_0 with a center-to-center spacing $2b$.[8] We represent the transmittance of P_0 by

$$t_i(x) = f(x + b) + g(x - b). \tag{1}$$

We use 1-D notation both for simplicity and because we will deal mainly with 1-D processing in this paper. The Fourier transform plane intensity distribution (modulus squared of the transform of t_i) is

$$I_1(u) = |F(u)|^2 + |G(u)|^2 + 2|F||G| \cos[4\pi ub + \phi(u)], \tag{2}$$

where F and G are the Fourier transforms of f and g, and the coordinate x_1 of the transform plane P_1 is related to the spatial frequency u by $u = x_1/\lambda f_L$. The focal length of the transform lens is f_L, and the phase term $\phi(u) = \arg G(u) - \arg F(u)$ equals the difference between the phases of the transforms of the two functions.

This Fourier transform distribution is recorded on an optically addressed spatial light modulator (SLM),[9] and the SLM is now read by illuminating it with a plane wave. Assuming that the SLM's amplitude transmittance is approximately a linear function of writing intensity I_1, we obtain at the output plane P_2, upon forming the Fourier transform of this transmittance.

$$u(x_2) = f \circledast f + g \circledast g + f \circledast g * \delta(x_2 + 2b) + g \circledast f * \delta(x_2 - 2b), \tag{3}$$

where $\circledast$ denotes correlation, and $*$ denotes convolution.

The authors are with Carnegie-Mellon University, Department of Electrical Engineering, Pittsburgh, Pennsylvania 15213.
Received 30 January 1978.
0003-6935/78/1101-3418$0.50/0.
© 1978 Optical Society of America.

Fig. 1. Schematic of the basic electronic JTC system.

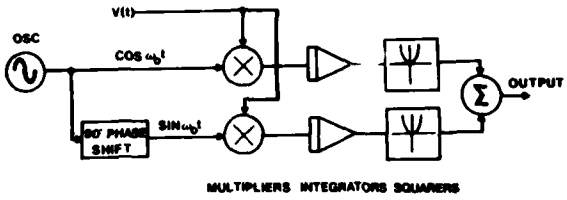

Fig. 2. Block diagram of the electronic section of the basic electronic JTC system.

This is the desired correlation of the input functions centered at $x_2 = \pm 2b$ (assuming equal focal lengths for both transform lenses).

In the electronic readout JTC system, the intensity distribution in Eq. (2) is converted to an electrical time function (video signal) by a scanning photodetector as shown in Fig. 1, and the second transform is produced in modified form electronically as shown in Fig. 2. We represent the output electronic signal from the detector at P_1 in 1-D by

$$v(t) = RI_1(u), \tag{4}$$

where R is the detector's responsivity in volts/unit intensity, s is the detector's scanning speed, and hence $x_1 = st$, and $u = st/\lambda f_L$. This video signal $v(t)$ is multiplied by quadrature sinusoids $\sin(\omega_0 t)$ and $\cos(\omega_0 t)$, these two separate products integrated, and the integrals squared and summed. We then obtain a new output:

$$\begin{aligned} v'(\xi) &= \left[\frac{1}{T}\int_{-t_0}^{t_0} v(t)\cos\omega_0 t\,dt\right]^2 + \left[\frac{1}{T}\int_{-t_0}^{t_0} v(t)\sin\omega_0 t\,dt\right]^2 \\ &= \left(\frac{R\lambda f_L}{sT}\right)^2 \left|\int_{-u_0}^{u_0} I_1(u)\exp(j2\pi u\xi)du\right|^2 \\ &= \left(\frac{R\lambda f_L}{sT}\right)^2 |\mathcal{F}^{-1}[I_1(u)\,\mathrm{rect}(u/2u_0)]|^2 \\ &= \left(\frac{R\lambda f_L}{sT}\right)^2 |\mathrm{sinc}(2u_0\xi) * [f \circledast f + g \circledast g + g \circledast f * \delta(\xi - 2b) \\ &\quad + f \circledast g * \delta(\xi + 2b)]|^2, \end{aligned} \tag{5}$$

where T is the time constant of the integrator (the product of a resistance and capacitance in the typical op amp integrator), $2t_0$ is the line scan time, $u_0 = st_0/\lambda f_L$, and $\xi = \omega_0 \lambda f_L/2\pi s$. The sinc function in Eq. (5) represents the finite frequency bandwidth of the correlator system. If the transform plane P_1 is repetitively scanned, the integrators in Fig. 2 are discharged to zero initial value after each line, and the oscillator's frequency ω_0 (and hence correlation shift parameter ξ) are incremented between scans, the desired output correlation of the two input functions results.

A. Anatomy of the Joint Transform Pattern

We now examine the joint transform intensity waveform at P_1 of Fig. 1 as the input functions f and g are changed as an aid in visualizing the examples and system extensions to follow. From Eq. (2), we see that $|F|^2 + |G|^2$ is the slowly varying part of the output video signal. The important part of this signal is a cosine function at a frequency $2b$, phase modulated by the difference between the phases of the transforms of the two functions and its strength proportional to the product of their magnitudes.

We assume approximately equal power spectra $|F| \simeq |G|$ in all cases to simplify the analysis. For the case of equal inputs $f = g$, the expected output is the autocorrelation, $\phi = 0$, and Eq. (2) becomes

$$I_1(u) = 2|G|^2(1 + \cos 4\pi ub). \tag{6}$$

The recorded fringe pattern or cos[ ] term thus has 100% amplitude modulation. If one input function is displaced away from the other in P_0, i.e., the separation between f and g is increased (say to $2.5b$), then the frequency of the fringes increases to $2.5b$. With $f = g$, Eq. (2) now becomes

$$I_1(u) = 2|G|^2(1 + \cos 5\pi ub) = 2|G|^2[1 + \cos(4\pi ub + \pi ub)]. \tag{7}$$

From the second formulation in Eq. (7), we see that we can also view this as the addition of a linear phase term whose slope, or derivative with respect to u, is proportional to the shift in the location of g in P_0 and thus contains data on the location of g in f.

If $f \neq g$, the fringe pattern is no longer a pure cosine. Equation (2) describes the resultant electronic output from the plane P_1 detector; phase modulation $\phi(u) \neq 0$. The power spectral density at the carrier frequency $2b$ is now decreased. This spectral component is the correlation, and hence the loss in this component due to $\phi \neq 0$ causes an associated loss in signal-to-noise ratio (SNR) of the correlation output.

If $f(x) = ag(x)$, f and g are identical except for a decreased strength for f by a factor a. The detected pattern is now

$$I_1(u) = |G|^2(1 + a + 2a\cos 4\pi ub). \tag{8}$$

As seen, the modulation is reduced with the amplitude of the information-bearing ac term reduced proportional to the decreased strength of f.

By electronically introducing phase modulation into $v(t)$, one can compensate for phase differences between F and G such as those due to signal propagation differences and P_1 detector scanning errors. By sensing the level of the ac signal in Eq. (8), the presence of differences in the strengths of the input functions can be found and compensated for. We discuss such extensions of this electronic readout JTC system later and for now only note that considerable information on the

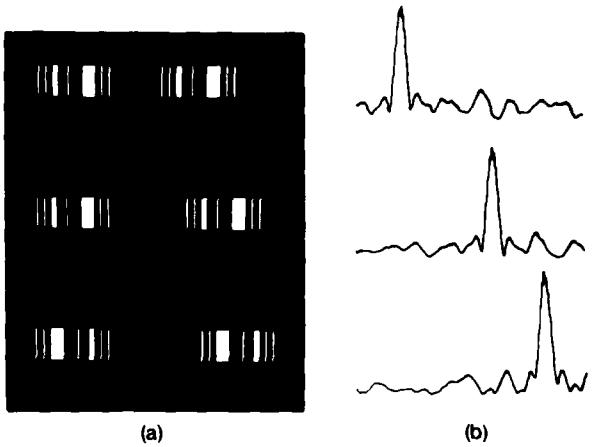

Fig. 3. Example of pulse-coded waveform correlation: (a) input transparency; (b) correlation output.

similarity as well as the relative positions and strengths of the two input functions may be extracted from the amplitude and phase of the ac fringe signal.

III. Autocorrelation Experiments

The optical system of Fig. 1 was used. A 50-mW He–Ne laser source at $\lambda = 633$ nm and equal focal lengths $f_{LS} = f_{LC} = 381$ mm for the spherical and cylindrical lenses provide unity vertical image magnification ($f_{LS}/f_{LC} = 1$) from P_0 to P_1 with the horizontal transform of the input pattern on each line appearing at the corresponding horizontal output line (with an effective lens focal length $f_L = 381$ mm). A linear self-scanned CCD-addressed photodiode array (Reticon CCPD-1728) with 1728 16-μm square photodiode elements on 16-μm centers was used as the output detector. This circumvented the geometric distortion and MTF problems associated with vidicon and similar detectors. The array's 27.6-mm length covered ±114 cycles/mm of spatial frequency.

To simplify the output electronic system, a Tektronix 3L5 spectrum analyzer with 571B mainframe was used to convert the video signal into the desired correlation. In this system, the video signal $v(t)$ is heterodyned with an oscillator, and the product is bandpass filtered and peak detected. For a fixed oscillator frequency, the final output is the amplitude of the input frequency component at the difference of the oscillator frequency and the center frequency of the bandpass filter. As the oscillator frequency is swept, the output is the spectral amplitude density of the input in time. While this system does not explicitly realize Eq. (5), it provides an equivalent output.

Since transform lens focal length and detector resolution were fixed, the input size had to be adjusted to accommodate the latter. If the full width of a joint transform input is $3b$ (where the physical size of each input is b with a center-to-center input plane separation $2b$), then one must use a transform plane sampling interval of $u_s < 1/6b$. For various practical reasons we used $u_s = 1/12b$, oversampling by a factor of 2. The detector sampling interval of 16 μm results in $u_s = 0.132$ cycles/mm and a nominal input width of $3b = 3.77$ mm.

To demonstrate the use of this system in the correlation of pulse coded signals, a pseudorandom, twenty-pulse, feedback shift register code was generated by a computer program. The bit sequence used was 1,0,1,0,1,1,1,1,0,0,0,1,0,0,1,1,0,1,0,1. Bar pattern input images in the JTC input format (see left side of Fig. 3) were recorded with a Xerox Graphics Printer and photoreduced 200:1. Actual full widths ranged from 3.3 mm (top) to 4 mm (bottom). Input patterns with three different separations corresponding to three different signal range delays and the corresponding electronic analysis system outputs are shown in Fig. 3. As predicted by Eq. (5), the frequency of the cosine carrier increases as the separation between the inputs (or effectively the target range delay) increases. The corresponding frequency (horizontal axis in Fig. 3) or horizontal displacement at which the output correlation peak occurs is analogous to the target range, time of arrival τ, or shift necessary between the two input functions to achieve maximum correlation

$$p(\tau) = \int g(t) f(t + \tau) dt. \tag{9}$$

As shown in the right side of Fig. 3, the location of the output autocorrelation peak shifts to the right as the separation or range delay between the input signals increases. The middle peak represents a temporal carrier frequency of 150 kHz in $v(t)$.

Similar experimental demonstrations of this correlator were obtained for text and aerial imagery inputs. The results for the aerial input case are shown in Fig. 4. The objective here was to determine the location of the reference object g (the airfield) in various input patterns f. This pattern recognition operation is appropriate for a missile guidance application.[10] The shifted location of g in f in the sequence of three ground

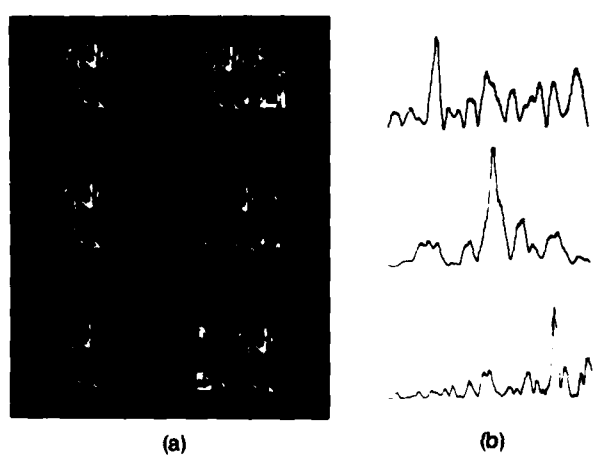

Fig. 4. Example of pattern recognition on aerial imagery: (a) input transparency; (b) correlation output.

image sensor data frames shown in Fig. 4 is intended to represent the drift of the projectile or missile off course. As shown in Fig. 4, the coordinate of the output correlation peak is proportional to the location of the reference object in the input data and hence provides the data necessary to correct the flight path of the projectile or missile.

IV. Equalizing Correlator; Theory

In the conventional JTC system, the output is the correlation of the two input functions f and g (with no convenient way to modify the operation performed). If these functions are the same except that one of them, say $f(x)$, has been acted upon by a linear space-invariant system, described by an impulse response $h(x)$, then $f(x) = g(x) * h(x)$, and the correlation output from the JTC becomes

$$f(x) \circledast g(x) = [g(x) * h(x)] \circledast g(x) = h(x) * [g(x) \circledast g(x)]. \quad (10)$$

The effect of the convolution with $h(x)$ shown in Eq. (10) is usually a degradation of the output correlation. The correlation peak is weaker and less sharply defined, and the output SNR is less than that of the autocorrelation case $g(x) \circledast g(x)$. By suitably modifying the basic optical/electronic correlator, one can neutralize the effect of this type of signal distortion when the distorting transfer function is known *a priori* or can be estimated. This capability follows from the access, for electronic modification, to the joint transform pattern video signal afforded by the hybrid correlator system. Compensation for linear time-invariant distortion is known as equalization in the communications field;[11] hence we refer to our new system as an equalizing correlator.

To see how this equalization can be accomplished, we examine the video signal (ac term of interest only) that results when $g(x)$ and $g(x) * h(x)$ are the inputs:

$$v(t) = 2R\left|G\left(\frac{st}{\lambda f_L}\right)\right|^2\left|H\left(\frac{st}{\lambda f_L}\right)\right| \cos\left[2\pi\left(\frac{2sb}{\lambda f_L}\right)t + \arg H\left(\frac{st}{\lambda f_L}\right)\right] + \text{etc.}, \quad (11)$$

where $H(u) = \mathcal{F}[h(t)]$ is the distorting transfer function. If this signal is fed to a phase modulator while a temporal voltage waveform $-\arg H(st/\lambda f_L)$ is applied to its phase control input, the distorting term $\arg H(st/\lambda f_L)$ is removed from the cos factor. Equivalently we can phase-modulate the heterodyne oscillator; this latter method is easier to implement electronically. Similarly, if $v(t)$ and another signal $|H(st/\lambda f_L)|^{-1}$ are electronically multiplied, the product will be free of the multiplicative distorting factor $|H|$ in Eq. (11). Fourier-transforming the resulting signal will yield the autocorrelation of g.

Arbitrary linear space-invariant filtering can be performed on the correlation output by such a system; equalization of input distortion is a special case of this. Since the system's filtering function is determined by a pair of voltage waveforms, it can be changed with the ease and speed with which a signal generator can be reprogrammed. The equalizing correlator can thus be used in the processing of radar or sonar signals degraded by the propagation path or medium[12] and for the compensation of imperfections in optical processor system elements. In the latter category are nonuniform transform plane scanning speed and a restricted class of transform plane lens errors, namely, those equivalent to applying different space-invariant filters to the two inputs f and g. If the distorting function is known *a priori*, direct correction is possible. In more realistic situations, some knowledge is available of the expected degradations, or various degradations can be assumed, and the system's performance improvement can be used to judge the appropriateness of the assumed degradation on an *a posteriori* basis.

V. Equalizing Correlator; Experiment

To demonstrate the equalization concept, we correlated a distorted signal against the original signal and applied equalization to recover the correlation peak. The formatted pair of inputs is shown in Fig. 5(a). The original signal [left side of Fig. 5(a)] was the pseudorandom pulse train used in the autocorrelation experiments. The distorting transfer function H was of unit

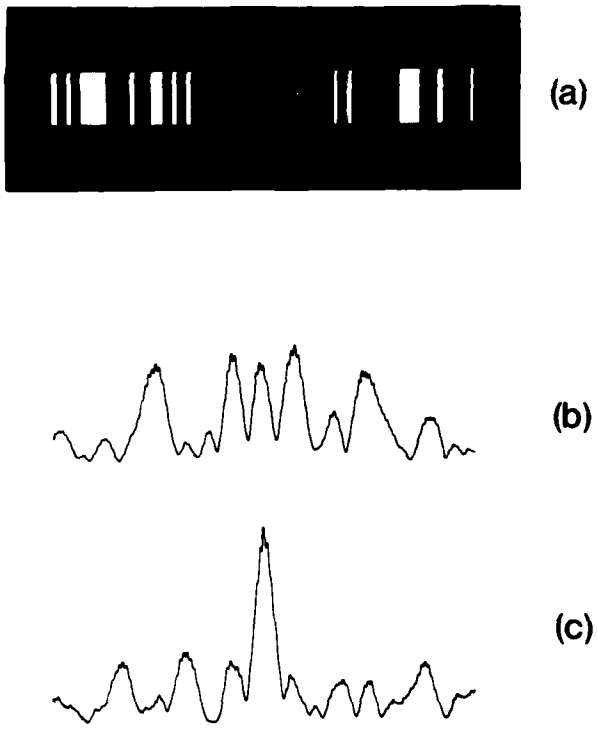

Fig. 5. Example of equalizing correlation: (a) phase-distorted input and reference signals; (b) conventional correlation output; (c) equalizing correlator output.

magnitude, while its phase part, shown in Fig. 6, consisted of five rectangular pulses of magnitude π with a baseline of zero. The distorted input pattern was generated by numerically convolving the undistorted input with $h(x)$, thresholding the resulting signal, and computer-graphically printing and photoreducing this hard-clipped waveform [right side of Fig. 5(a)]. The conventional correlation of these two patterns is shown in Fig. 5(b). Positional resolution and SNR are both seen to be poor. The correlation output with equalization circuitry in operation is shown in Fig. 5(c)—a clear correlation, with greatly enhanced SNR and position-measurement accuracy.

The particular transfer function H used in this demonstration was chosen to simplify the video signal processing circuitry. The distorted video output signal was fed to a phase modulator, which reversed the polarity of the video signal at appropriate times to realize modulation by $-\arg H$. A pulse generator was used to produce the five-pulse sequence (of the same form as Fig. 6) that was used to control the modulator.

This equalizing correlator system is another method by which the flexibility and repertoire of operations achievable on an optical processor can be increased. Matched spatial filter weighting and synthesis control,[2,13] hybrid optical/digital processing,[14] and space-variant processing[15,16] are other methods by which the flexibility of an optical correlator can be extended.

VI. Extensions and Discussion

Another use of the general optical/electronic JTC is in the normalization of correlations. Correlation degradation can arise when one of the input signals to be correlated is reduced in strength by a factor a from that of the other input function. The degraded joint transform pattern for this case is described by Eq. (8). The amplitude $2a$ of the cos term in the video output signal can easily be measured and used to control the vertical scale in the output patterns [Figs. 3(b), 4(b), and 5(c)]. This results in a normalized output correlation pattern independent of changes in the strength of the input signal. Other nonlinear processing operations such as generating the logarithm of the spectrum (as required in cepstral processing) can also be realized using such a system.

A. Carrier Period Variance and Coherence Measure

The presence or absence of a correlation and its positional coordinate are often of primary concern rather than the actual shape of the correlation function. We therefore now consider another new optical/electronic system, which we shall call a coherence measure correlator, that greatly improves the speed at which the correlation/no correlation decision can be made along with ways of implementing it. We conclude this section with a discussion of how it can be applied in range/Doppler multichannel signal processing. This system uses the configuration of optics and scanning detector shown in Fig. 1. However, the video signal is now operated on by a different kind of electronic processor than that discussed so far.

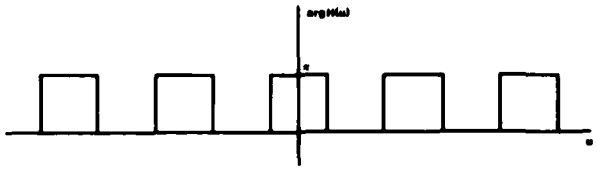

Fig. 6. Distorting phase transfer function used in the equalizing correlator experiment.

As was pointed out in Sec. II, phase modulation of the fringe pattern causes a correlation loss, whereas a coherent uniform fringe frequency (identical inputs) produces a large output correlation. Thus, by measuring the coherence, or spectral purity, of the video signal, the electronics can detect an autocorrelation, or match of the input functions, or compute the degree of similarity between them. Several qualitatively related properties of the video signal may be used as coherence measures, namely, carrier period variance, carrier phase modulation or phase variance, and instantaneous frequency variance. The smaller any of these quantities are, the greater the video signal coherence and hence the greater the degree of similarity.

We now describe how the carrier phase variance might be determined by electronic postprocessing of the video output described by Eq. (2). Bandpass-filtering Eq. (2) removes the first two terms and leaves $2|F||G| \cos[4\pi ub + \phi(u)]$. The amplitude modulation present on this cosine fringe carrier can be removed by a limiter leaving as the output the phase-modulated carrier $\cos[4\pi ub + \phi(u)]$. If this signal is fed to a phase demodulator, we obtain a voltage output proportional to the phase modulation $\phi(u)$ on the carrier. Squaring this quantity and integrating it electronically over a line scan time yield a final output voltage proportional to the carrier's phase variance

$$\mathrm{var}[\phi(u)] = \int_{-t_0}^{t_0} \phi^2(u)du. \tag{12}$$

If a frequency demodulator is used instead of a phase demodulator, we obtain the instantaneous frequency variance

$$\mathrm{var}[\phi'(u)] = \int_{-t_0}^{t_0} [\phi'(u)]^2 du. \tag{13}$$

To compute the carrier (fringe) period variance over one detector line scan, we threshold the video signal into a digital pulse sequence we represent by $(u_1, u_2, \ldots, u_N)$ in which these u_n are the u values at which positive-going zero crossings of the phase-modulated carrier occur [i.e., where $\cos(4\pi ub + \phi) = 0$, and its derivative with respect to u is positive]. If this pulse sequence is then fed to a digital or combination analog/digital processor, the mean carrier period

$$\overline{\Delta u_k} = \frac{1}{N}\sum_{k=1}^{N} \Delta u_k = \frac{u_N}{N} \tag{14}$$

and the carrier period variance

$$\overline{(u-u)^2} = \frac{1}{N}\sum_{k=1}^{N} (\Delta u_k - \overline{\Delta u})^2 = \frac{1}{N}\sum_{k=1}^{N} \left(\Delta u_k - \frac{u_N}{N}\right)^2 \tag{15}$$

can be calculated, where $\Delta u_k = u_k - u_{k-1}$ is the carrier period at the kth cycle.

This electronic processor can take many forms. The mean and mean square pulse width over one line scan time can be calculated simultaneously. At the conclusion of the scan we subtract the square of the mean from the mean square pulse width. This yields the variance. An alternate simpler circuit to measure coherence is the phase-locked loop (PLL).[17] A PLL consists of a voltage-controlled oscillator (VCO) and a phase comparator. The latter compares the VCO's output with the input signal presented to the loop, and the phase comparator output is connected via a low pass filter to the control input of the VCD. When the loop is in lock, the VCD is forced to track the input signal, and its control input voltage indicates the instantaneous frequency of the input signal. The FLL thus behaves as an FM demodulator. In our case, the ac content (variance) of the VCO control voltage can serve as a coherence measure when the video signal is applied to the PLL's input.

Coherence measure processing requires a single line scan rather than repetitive scans, as do the system of Fig. 2 and its relative, the spectrum analyzer. The processor's output is computed almost immediately at the end of each scan. This improvement in efficiency is especially important when the 2-D nature of optical processing is exploited in performing multichannel 1-D signal processing.

An example of such processing is the correlation of two signals differing in Doppler. The first processing step in this case is to correlate one signal against a number of different doppler versions of the other signal, seeking the best match. The second step is to extract the range from the correlation of the optimally similar pair found in step 1. This processing operation can be implemented with the aid of the coherence measure correlator as follows: On successive horizontal lines in the input plane, signals are written in pairs, with one of the signals repeated and the other signal written in different doppler versions on each line. This array of spatial signals is Fourier transformed in the horizontal direction and imaged in the vertical direction by a spherical–cylindrical lens system. The horizontal joint transform fringe patterns on successive lines are sensed by a 2-D raster scanning detector. The coherence measure parameter is computed on-line for each scan line from the detector's video signal. The line which yields the greatest coherence indicates the optimal Doppler match; to determine range, only a 1-D transform (as in Fig. 2) of the one line with the largest coherence need be performed. Thus, range/Doppler processing can be performed in one scanner frame time by a relatively simple configuration of components.

The support of the Air Force Office of Scientific Research on contract AFOSR 75-2851 administered by the Air Systems Command and the Office of Naval Research on contract NR 350-011 for the work reported on herein is gratefully acknowledged.

References

1. A. Vander Lugt, IEEE Trans. Inf. Theory **IT-10**, 139 (1964).
2. A. Vander Lugt and F. B. Rotz, Appl. Opt. **9**, 215 (1970).
3. C. S. Weaver and J. W. Goodman, Appl. Opt. **5**, 1248 (1966).
4. J. E. Rau, J. Opt. Soc. Am. **56**, 1490 (1966).
5. C. S. Weaver *et al.*, Appl. Opt. **9**, 1672 (1970).
6. J. E. Rau, J. Opt. Soc. Am. **57**, 798 (1967).
7. A. Macovski and S. D. Ramsey, Opt. Commun. **4**, 319 (1972).
8. D. Casasent and A. Furman, Appl. Opt. **16**, 285 (1977).
9. D. Casasent, Proc. IEEE **65**, 143 (1977).
10. D. Casasent and M. Saverino, SPIE Proc. **118**, 11 (1977).
11. W. D. Gregg, *Analog and Digital Communications* (Wiley, New York, 1977).
12. Topical issue on Adaptive Optics, J. Opt. Soc. Am. **67**, 269–409 (1977).
13. D. Casasent and A. Furman, Appl. Opt. **16**, 1662 (1977).
14. D. Casasent and W. Sterling, IEEE Trans. Compt. **C-24**, 318 (1975).
15. J. W. Goodman, Proc. IEEE **65**, 29 (1977).
16. D. Casasent and D. Psaltis, Proc. IEEE **65**, 77 (1977).
17. F. M. Gardner, *Phaselock Techniques* (Wiley, New York, 1966).

CHAPTER 5

MULTI-SENSOR PATTERN RECOGNITION

Reprinted from SPIE Vol. 201—Optical Pattern Recognition
© 1979 by the Society of Photo-Optical Instrumentation Engineers, Box 10, Bellingham, WA 98225 USA

Statistical and deterministic aspects of multisensor optical image pattern recognition

David Casasent, Domingo Munoz
Carnegie-Mellon University
Department of Electrical Engineering
Pittsburgh, Pennsylvania 15213

ABSTRACT

A classification of multi-sensor imagery from the sensor's point of view is advanced. From this treatment, the statistical and deterministic contributions to a multi-sensor image correlation process are more clearly seen. The optimum preprocessing operation for several cases of multi-sensor image pattern recognition are noted and the use of weighted matched spatial filter synthesis as a one step optical pattern recognition correlator is described. Theoretical formulation and experimental verification of the result that edge enhancement preprocessing is not always optimum in a multi-sensor optical image pattern recognition system are presented.

1. INTRODUCTION

Performing pattern recognition on multi-sensor (MS) imagery arises: in the processing of satellite imagery for earth resources uses [1], in the registration of scenes [2,3], and in missile guidance [4,5] among other applications. In this paper, we present a new optical pattern recognition (OPR) approach to MS image pattern recognition (IPR). Our primary purpose is to determine the agreement between a given stored reference scene f(x,y) and a live sensed input image g(x,y). For the particular scenario to be considered, the input g is a radar image and the reference f is an aerial image. The specific problem is to optimize the SNR of the correlation in the presence of typical MS image differences.

In Section 2, we describe a new model for MS imagery and distinguish three cases of MS-IPR. In Section 3, we discuss the optimum preprocessing necessary for each case. In Sections 4 and 5 we present experimental confirmation of our theoretical formulation and discuss our resultant data.

This new model of the MS-IPR problem, the use of OPR and weighted matched spatial filter (MSF) synthesis in its solution, new OPR concepts (such as: statistical and deterministic OPR, statistical gradient polarization equalization), and new issues (such as: spatial structure distribution and gradient quality) represent the major new contributions contained in this work.

2. STATISTICAL AND DETERMINISTIC MS IMAGE MODELS

MS imagery (with all geometrical distortions removed) can be described by a set of feature vectors that are similar in both scenes (we refer to these as key objects) and by a set of different features (due to additive and multiplicative noise). Most PR research has only considered additive noise. The optimum processor for the additive white noise case is well known to be an MSF. In MS imagery, additive noise arises due to texture and scene detail present in one sensor's image, but absent in another's. Figure 1 shows an example of such an image pair.

We choose to include multiplicative noise (characterized by image contrast reversals of random polarity) in our description of MS imagery. More so, we choose to describe a scene from the sensor's point of view and to clearly distinguish between the scene itself (no sensor variations considered) and an image of the scene (obtained with a given sensor). The terms scene and image are defined as above.

If we consider the scene itself, it can be modeled as uncorrelated data (if it contains many features). In practical PR applications, the scene contains key objects. If there are only a few key objects and if they dominate the scene, the scene is highly correlated and thus more deterministic and less statistical. As the number of key objects in the scene increases (assuming uncorrelated and independent key objects), the scene becomes highly uncorrelated.

Contrast reversals are the dominant unique image feature germaine to MS image data. We thus choose to classify MS imagery as statistical or deterministic solely on the basis of contrast reversals and to model these contrast reversals as multiplicative noise. Thus, we will adopt definitions of MS imagery from the sensor's point of view, rather than for the scene itself. If a pair of MS images are dominated by contrast reversals, we refer to the scene as statistical (see Figure 2). We note that the distribution of the polarity of the gradient of such images are the statistical factor to which we refer. This leads to the vital aspect of statistical gradient equalization and to the key point that these random contrast reversals are the major generic characteristic of MS imagery. In some instances, neither the multiplicative noise (contrast reversals in Figure 2) nor the additive noise (see Figure 1) dominate and the resultant MS imagery is best described as deterministic with no noise (see Figure 3). The MS image data base used consisted of radar and aerial images of different scenes. The three image pairs to be reported upon are shown in Figures 1-3 and summarized in Table 1.

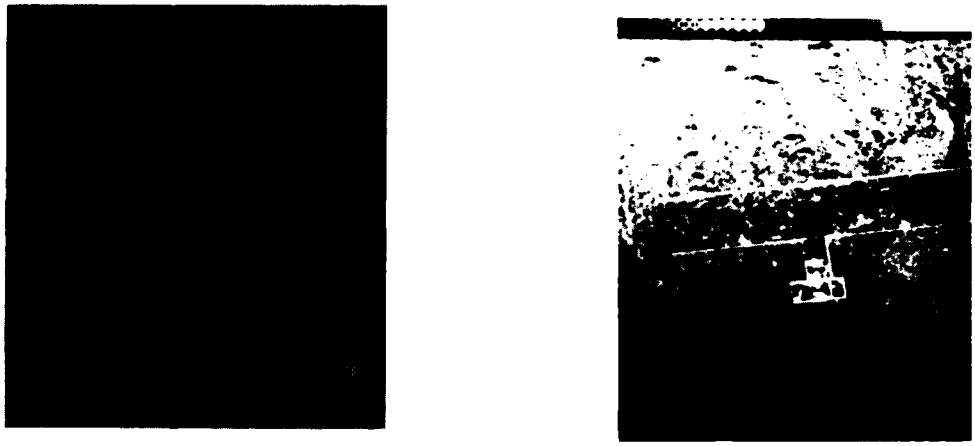

(a) (b)

Figure 1. Multi-Sensor Imagery Classified as Deterministic with Additive Noise. (a) Aerial Image, (b) Radar Image.

(a) (b)

Figure 2. Multi-Sensor Imagery Classified as Statistical. (a) Aerial Image, (b) Radar Image.

(a) (b)

Figure 3. Multi-Sensor Imagery Classified as Deterministic with No Noise. (a) Aerial Image, (b) Radar Image.

Table 1. Multi-Sensor Image Pattern Recognition Scenarios

Figure	Classification	Pre-Processing	Weighted MSF
1	Deterministic with Noise	Edge enhancement	High u^*
2	Statistical	band-pass, magnitude detection	Medium u^*
3	Deterministic, no noise	Same as Auto-correlation	Low u^*

We summarize these three MS image cases in Table 1. For completeness, we note the optimum digital pre-processing operation required for each case and the corresponding optical weighted MSF synthesis technique that is theoretically optimum for each case. These issues are discussed in Section 3. In these MS image definitions, we consider only scenes containing key objects (becasue of their information content), but we allow contrast reversals to occur within the key objects as well as within the scene's background.

3. THEORETICAL BASIS FOR MS-IPR

The most common pre-processing operation performed in MS-IPR is the edge enhancement or differentiation of the input images [2,3]. Such an isotropic contour operator [6] is:

$$I_1 = 1 - k^2 \nabla^2 , \tag{1}$$

where ∇^2 is the Laplacian. This operator enhances the edges of the scene and retains the polarity of the edges. The non-linear isotropic operator

$$I_2 = k^2 \left[\left(\frac{\partial}{\partial x} \right)^2 + \left(\frac{\partial}{\partial y} \right)^2 \right] \tag{2}$$

retains only the magnitude of the edges of a scene. It has been shown [20] that a differentiation pre-processing operator is not always optimum. Specifically, for highly uncorrelated scenes, no pre-processing is optimum; whereas for highly correlated imagery, the second derivative is the optimum pre-processing step [20].

When noise is present in the data, the above conclusions are not appropriate. In the presence of additive noise, the optimum pre-whitening filter can be shown to be [3]:

$$h_w = \frac{1}{2A\sqrt{\alpha\beta}} \left[\alpha\beta\delta(x,y) + \beta \frac{\partial}{\partial x} + \alpha \frac{\partial}{\partial y} - \frac{\partial^2}{\partial x \partial y} \right] , \tag{3}$$

where A, α and β are parameters describing the shape of the noise auto-correlation function. From (3), we clearly see that a derivative or gradient pre-processing operator is not sufficient, rather a weighted combination of no pre-processing, term 1 in (3), and differentiation, the last terms in (3), is seen to be optimum when noise is present.

Svedlow [3] found that a threshold gradient pre-processing operator, in which the polarity of the gradient was suppressed, performed best. We now see that this operation is preferable because it removes the statistical nature (the polarity of the gradient) of a MS scene (as defined in Section 2). Smith [7] utilized a linear system approach to the MS-IPR problem for the case of additive noise. He found that the product of a noise whitening filter and a weighted filter reflecting the target's SNR was optimum. These combined operations used by Smith [7] can be shown to be equivalent to a type of bandpass filter rather than the high-pass filter (edge enhancement) normally employed.

Adjunct spatial filters in front of the MSF in an optical correlator can perform the differentiation, bandpass filtering, and noise spectrum whitening operations noted above [8,9]. In optical character recognition correlation experiments, Winzer [8] found strong erroneous cross-correlations when high-pass filtering was performed. In light of the above formulation, we can see that this occurred because, in his optical character recognition case, the large number of characters in the input search scene corresponded to our case of a large number of key objects in the scene. As we noted in Section 2, the scene for this case is more statistical and less deterministic. For such cases, differentiation pre-processing alone is not adequate. This case is somewhat analogous to the missile guidance scenario of a key object surrounded by other structured objects. Synthesis of the proper phase of the differentiated scenes (the statistical gradient equalization concept noted in Section 2) is the major problem in such adjunct filtering schemes. A two stage optical system (in which the image is re-recorded before correlation) could be used to perform the gradient equalization step. By recording the magnitude of the gradient of the original image, the polarity information of the gradient, and hence the random or statistical nature of the image, is removed. We refer to this technique as statistical gradient polarization equalization. We will concentrate our attention on a single step MSF optical correlator and the use of weighted MSF synthesis to optimize the MS-IPR process.

The concept of weighted MSF synthesis is quite simple [10] and is best described using the frequency plane correlator [11]. In this system (Figure 4), the sensed image is placed at P_1. Its Fourier transform G is formed by L_1 at P_2. Stored at P_2 is the MSF with nominal transmittance proportional to F*. Leaving P_2 we find F*G and at P_3 we find the Fourier transform (denoted by the operator $\mathcal{F}$) of this product of two Fourier transforms or

$$\mathcal{F}[F^*G] = g \circledast f \quad , \tag{4}$$

which is the desired correlation (denoted by the symbol $\circledast$) of the two functions. Detailed analysis of the MSF synthesis process [10] will show that the exact transmittance of P_2 is

$$t = 1 + 1/K + (2/\sqrt{K}) \cos (2\pi\alpha x + \text{Arg } F) \quad , \tag{5}$$

where α is the spatial frequency determined by the angle between the signal and reference beams and

$$K = A^2/|F|^2 \tag{6}$$

is the beam balance ratio. In (5), we note that the fringe modulation is a maximum when K = 1.

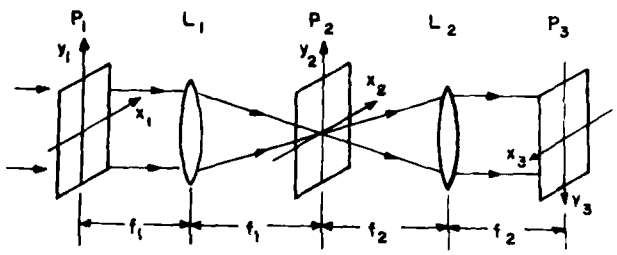

Figure 4. Optical Frequency Plane Correlator Schematic.

From (6) we note that K varies spatially (since F does) and hence so does the modulation. Thus, weighted MSF synthesis simply involves choosing the spatial frequency u^* we wish to optimize in the data. Low (high) u^* choices result in equivalently bandpass (high-pass) filtering functions for the MSF, with high u^* values resulting in the use of differentiated images in the correlation process. The origin of the entries in the last two columns in Table 1 should now be apparent.

A final aspect of MS-IPR deserves note at this point. We refer to the issues of edge quality and spatial structure and distribution. The first term refers to the fact that the derivatives of two images will differ considerably depending upon the sharpness of the edges in the original image. As a result, the gradient of one MS image may resemble a blurred version of another image of the same scene. When this effect occurs, statistical gradient polarity equalization effects are less important in the MS image correlation. Hard limiting is one often used pre-processing step for such MS problems. However, this operation does not appear to always be necessary. This conclusion arises because the low and mid-spatial frequencies associated with the relative distribution of the edges of the scene (i.e., their relative position with respect to one another) are preserved in all cases. We refer to this issue as spatial structure distribution and note that it often contributes more to the optical correlation than do the high frequencies due to the edges themselves. This is especially true in practical MS-IPR data, when resolution and geometrical differences are present between the two MS images being correlated.

4. EXPERIMENTAL CONFIRMATION

Auto-correlations and cross-correlations of all imagery in Figures 1-3 were performed with K set equal to 1 in four different spatial frequencies bands (see Table 2). A wedge-ring detector [12] was used to facilitate setting of K values. As a measure of correlation plane quality, we use

$$\text{SNR} = \frac{E^2\{c(0,0)\}}{\text{var}\{c(x,y)\}} \quad , \tag{7}$$

where $E^2\{\ \}$ is the intensity of the expected value of the correlation c, at the peak at registration (0,0) and where correlation noise is defined as the variance of the correlation at coordinates (x,y) far from registration.

Table 2. MSF Frequencies Bands Used

Band	Spatial Frequency (cy/mm)
B	2.1-2.8
C	3.4-4.4
D	5.1-6.4
E	7.4-9.3

After obtaining power spectra data for all imagery (using the wedge-ring detector), auto-correlations of all images of each scene were obtained using weighted MSF's with K = 1 in the four spatial frequency bands u* indicated in Table 2. For each scene, both positive and negative radar images were available as well as an aerial image. The result of the four auto-correlations (at four u* bands) for the image in Figure 2 are shown in Figure 5. Auto-correlation data for the other scenes were similar. In all instances, the optimum auto-correlation was found to occur for the MSF with K = 1 in u* band B. The lower SNR of the radar positive image was due to its decreased resolution compared to the corresponding radar negative image. From Figure 5, we also see that the auto-correlation of the aerial image generally yields less SNR than the auto-correlations of the radar images. This is due to the increased mid-spatial frequency textural data present in the radar images.

These auto-correlation experiments verified our earlier remarks on the more deterministic nature of an auto-correlation. These data also show the usefulness of weighted MSF synthesis in the optimization of auto-correlations. The variations of the correlation with u* of the MSF occur due to the statistics of the scene itself. Recall that neither additive noise nor phase reversals occur in the auto-correlation data and thus these variations in SNR with u* are due to the statistics of the scene itself, rather than to the MS features (such as additive or multiplicative noise).

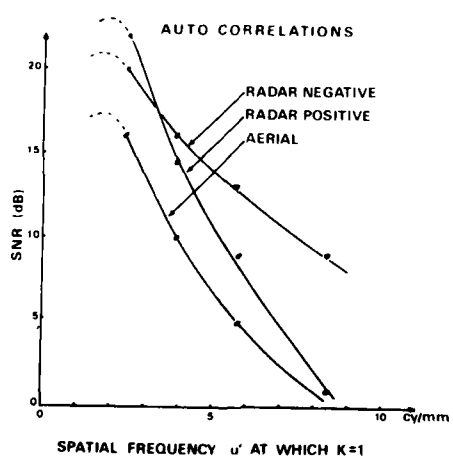

Figure 5. Auto-Correlation SNR versus u* for the Scene in Figure 2.

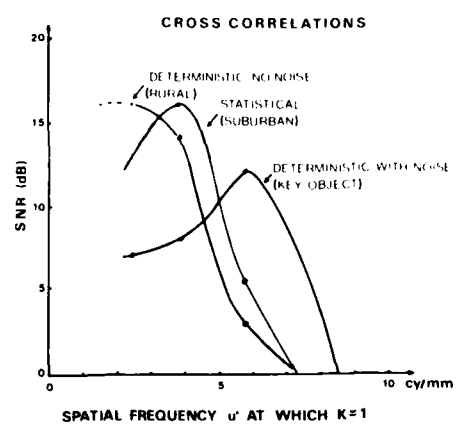

Figure 6. Cross-Correlation SNR versus u* for the Three MS Scenes.

The resultant optical cross-correlation experimental SNR versus u* data are shown in Figure 6. These experimental data were obtained using the images in Figures 1-3. In all cases, an MSF of the aerial scene served as the reference with the radar negative as the input pattern (this is the expected MS-IPR scenario). From these data in Figures 5 and 6 we observe that:

(1) Cross-correlation SNR can be optimized by proper choice of u*.
(2) The optimum u* for the cross-correlations differs from the u* found for the auto-correlations.
(3) Different u* values are optimum for each of the three scene classes .

5. DISCUSSION

A detailed analysis of the data in Figure 6 and the general theoretical remarks advanced earlier in Section 3 and summarized in Table 1 shows excellent agreement. The scene of Figure 1 (classified as deterministic with noise) was found to exhibit the optimum cross-correlation SNR with a large u* setting in band D. This high u* value is equivalent to emphasizing high spatial frequencies in the image. For such data in which additive noise is the dominant MS feature, the high-pass filtering preprocessing step should be more heavily weighted. The relative weighting is determined by the statistics of the noise as in (3).

For the scene in Figure 3, the cross-correlation SNR was found to peak at the same low u* band B setting that was found to be best for the auto-correlation case. This is as expected, since the different MS images of the scene in Figure 3 do not exhibit dominant additive or multiplicative noise. We thus classified this scene as deterministic with no noise.

For the scene of Figure 2 (classified earlier as statistical or dominated by contrast reversals), a mid-range value of u* equal to band C was found to be optimum. This mid-range u* setting (larger than the u* value (band B) found to be best for the auto-correlation and less than the highest u* setting (band D) corresponding to a differentiation or high-pass image filtering found to be best for the scene in Figure 1) is representative of a band-pass filtering MSF or equivalently to an MSF in which a weighted combination of no pre-processing and edge enhancement is used.

Another important aspect of MS-IPR is the use of histogram equalization [20]. In some MS-IPR work, Wong [17-18] and others have used a Karhunen Loeve amplitude or similar image pre-processing operation to produce an intensity equalized histogram. Our weighted MSF synthesis technique for MS-IPR can be reformulated as a type of frequency domain histogram equilization filtering. By decreasing low spatial frequencies and increasing high spatial frequencies in the spectrum of the image, we tend to equalize the histogram of the image's intensities. Such a process tends to flatten and broaden the spectrum of the image and tends to decrease the width of the output correlation peak. Such issues are important in image registration and for image differencing by frame-to-frame correlation [19].

We used SNR defined in (7) as our measure of correlation quality. By whitening the spectrum of the data, we decreased the variance of the correlation noise and hence increased the SNR of the correlation (decreasing the low frequency components in the image decreases the statistical correlation contributions and this makes the correlation more deterministic). To determine the noise filtering properties of the MSF holograms, we show in Figure 7 the variance of the output correlation noise for the cross-correlation of the imagery of Figure 3 versus the optimum MSF band u* chosen. As shown, correlation noise decreases as u* increases, thus indicating that flattening or broadening of the spectrum of the scene occurs in weighted optical MSF synthesis.

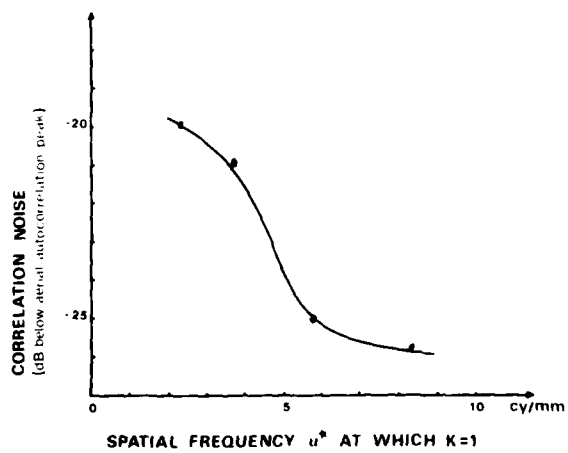

Figure 7. Var{c(x,y)} versus u* for the cross-correlation of the Figure 3 imagery.

6. SUMMARY

From these brief theoretical remarks and an extensive experimental program, we have shown that edge enhancement pre-processing is not always optimum for MS-IPR. Edge enhancement pre-processing is optimum only when the image contains a well structured and defined key object and when the MS imaging process contributes additive noise to one MS image. The true MS-IPR problem corresponds to the statistical image case (Figure 2). In this instance, the contrast reversals in the imagery contribute to the statistical distribution of the

gradient of the image and the optimum pre-processing is a weighted combination of no pre-processing and edge enhancement. Such multiplicative noise represents the true MS image problem. It differs considerably from the standard signal and additive noise problem (Figure 1).

Considerable prior MS-IPR research exists, both optical [13-15] and digital [3,16]. The prior IPR research is of most direct concern. In [13], radar and aerial scenes were correlated. In the correlation process, emphasis was given to the edges of the image (or to image structure) by optical differentiation. However, the major concern and use of these correlations was for the correction of geometrical errors in the image pairs. In [14], a general formulation of the optimum edge enhancement frequency plane operator was advanced and (for certain cases) the optimum edge enhancement operator was found to be similar to a Laplacian operator. This analysis lends further credence to prior work. In [15], major attention was given to multi-spectral data and attention was focused on the use of edge enhancement pre-processing and the importance of the number of key objects in the scene. In this formulation, contrast reversals within the key object were not allowed in the definition. In some digital MS-IPR research, the scenes chosen for correlation were often [17,18] dominated by a single key object with no contrast reversals for multiplicative noise present. Such images correspond to the classical signal in additive noise case, not to the true MS-IPR problem involving both additive and multiplicative noise (the presence of contrast reversals within the scene as well as within the key object).

In all cases, no prior work of which we are aware, has addressed: the statistical and deterministic contributions to the optical MSF pattern recognition correlation process, the importance of the polarity of the gradient of the scene in the OPR of such MS data, and the issues of image edge quality and image spatial structure distribution. In our work reported upon here, we have shown both in theory and by experiment that an optical correlator using weighted MSFs can successfully correlate MS imagery. We have also shown that such a pattern recognition system is of use in cases of multiplicative noise, additive noise, and no noise. This research was conducted for one specific MS-IPR data set (aerial and radar images). However, the results appear to be general enough to be of use in other MS-IPR cases or other IPR applications. A new model for such imagery and new definitions of classes of such imagery as well as the optical pre-processing required for each case have also been defined in the course of this work.

ACKNOWLEDGEMENTS

The support of the Air Force Office of Scientific Research (grant AFOSR 75-2851) for the research reported on here is gratefully acknowledged.

REFERENCES

1. R.G. Wilson and W.E. Sivertson, SPIE, 178 (1979).
2. W.K. Pratt, IEEE, AES-10, pp. 353-358 (1974).
3. M. Svedlow, et al., IEEE, AES-14, pp. 141-149 (1978).
4. D. Casasent and M. Saverino, SPIE, 118, 11 (1977).
5. D. Casasent, SPIE, 133, 51 (1978).
6. L. Kovasznay and H. Joseph, IRE, 43, pp. 560-570 (1955).
7. F. Smith, et al., Systems Control Incorporated, Palo Alto, October 1976 (Report DAAH 01-76-C-0673).
8. G. Winzer, Optica-Acta, 21, pp. 697-707 (1974).
9. D. Watrasiewicz, et al., Applied Optics, 7, pp. 1047-1051 (1968).
10. D. Casasent and A. Furman, Applied Optics, 16, pp. 1652-1662 (1977).
11. A. Vander Lugt, IEEE, IT-10, 139 (1964).
12. H. Kasdan and D. Mead, EOSD, 248 (1975).
13. R. Hudgin, SPIE, 117, 126 (1977).
14. F. Dickey and K. Shanmugan, Applied Optics, 16, pp. 145-148 (1977).
15. D. Casasent and Y. Barniv, SPIE, 137, 57 (1978).
16. M. Svedlow and C. McGillem, IEEE, GE-15, pp. 257-259 (1977).
17. R.Y. Wong, IEEE, AES-14, pp. 128-140 (1978).
18. R.Y. Wong, IEEE, SMC-7, 836 (1977).
19. L. Wald, D. Casasent, et.al., (these proceedings).
20. A. Arcese, et al., IEEE, IT-16, pp. 534-541 (1970).

CHAPTER 6

AVERAGED FILTERS

Optical pattern recognition using average filters to produce discriminant hypersurfaces

Charles F. Hester
Advanced Sensors Directorate, Technology Laboratory
U. S. Army Missile Command DRSMI TEI (R&D)
Redstone Arsenal, Alabama 35809

David Casasent
Department of Electrical Engineering
Carnegie Mellon University
Pittsburgh, Pennsylvania 15213

Abstract

A hyperspace description of the multiclass (multiobject) pattern recognition problem is advanced. Average filters composed of linear sums of orthonormal basis functions are found to provide the necessary discriminant hypersurfaces. Optical correlation using weighted matched spatial filter synthesis is used to determine the basis functions and their linear weights. The average filters are then assembled on a digital computer and used in an optical frequency plane correlator. Initial problem formulation theory and simulation results are included for an infrared tank pattern recognition problem.

Introduction

In the general pattern recognition problem multiple classes of objects, whether inherent or generated by a specific object, must be recognized with rejection of other objects not in the multiclass set. The multiaspects of targets encountered during target acquisition for missile guidance[1-3] as well as product line inspection[4] are diverse examples of this general multiclass pattern recognition problem. In this paper, a description of hyperspace (next section) and its use in solving this pattern recognition problem is reviewed[5]. We show how the discriminate hypersurfaces necessary to accomplish multiclass recognition and provide adequate false target rejection can be achieved by using an average filter. In the section on basis function determination, we describe how these average filters can be produced as weighted linear combinations of the orthonormal functions (the hyperspace basis) by which the input and reference have been described. How optical correlation using weighted matched spatial filter synthesis can be used to determine the basis, their weights and the average filter is discussed in the section entitled IR tank pattern recognition together with experimental data and a complete correlation matrix.

The experimental case chosen is the recognition of a tank from IR imagery independent of the aspect of the tank. Our initial average filter results and the result of correlations between it and various aspects of the tank target are presented in the section on IR tank pattern recognition.

Prior approaches to the multiclass problem have involved the use of multiple matched spatial filters[3,6]. Little attention has been given to pattern recognition techniques for IR sensors although considerable IR sensor advancements have occurred[7-9]. Other researchers have suggested post processing of the correlation matrix outputs of a multichannel correlator to enhance discrimination in cases such as character recognition[10]. Although our research is of use in this latter area, our present concern is to improve the recognition of a multiclass set of objects moreso than discrimination of one particular class from another class. The average filter used is based on the correlation matrix, thus incorporating post processing into the filter itself, and avoids the need for multiple filters and extensive post processing.

Hyperspace

We will consider one-dimensional functions for simplicity only. We denote the input image as f and assume that K different inputs $\{f_k\}$ can occur. The object functions to be recognized are g of which we assume that N different orientations $\{g_n\}$ of it are available. The average filter h to be constructed will be a weighted linear combination of the g_n. The task of the pattern recognition system is to recognize f if f belongs to the set of functions $\{g_n\}$ and to reject it otherwise. The K inputs may be different orientations of f, but not necessarily one of the N orientations in $\{g_n\}$. In fact, in the general formulation, the $\{g_n\}$ need not be different orientations of one object g.

We begin the description of our system by expanding f in a set of orthonormal functions ϕ, i.e.,

$$f(x) = \sum_j a_j \phi_j(x) \tag{1}$$

where $\int \phi_j(x)\,\phi_i(x)dx = \delta_{ji}$. (2)

The set of basis functions $\{\phi_j\}$ establishes the expansion coefficients a_j that specify f(x). Thus f(x) may be represented as a vector

$$\hat{f} = (a_1, a_2, \ldots a_n) \tag{3}$$

in a multidimensional vector space (hyperspace) where the $\phi_j(x)$ are the basis functions. Our reference functions can be expanded similarly

$$g(x) = \sum_i b_i \phi_i(x). \tag{4}$$

The correlation output is

$$R_{fg} = f(x) \circledast g(x) = \int f(x+\tau)g(x)dx = \sum_j \sum_i a_j b_i \int \phi_j(x+\tau)\phi_i(x)dx$$

or at $\tau = 0$, $R_{fg}(0) = \sum_j a_j b_j = \hat{f}\cdot\hat{g}$. (5)

From (5), we have established the special significance of the dot product as the correlation of $\hat{f}$ with $\hat{g}$ in this representation.

To illustrate the fundamental ideas of discriminate surface generation in hyperspace, we consider the two-dimensional diagram of Figure 1. Each X denotes a vector belonging to the set of objects to be recognized and each O is an unwanted object to be rejected. In this simple case, many discrimination surfaces are possible because the X and O points are well separated and clustered. Since $\hat{f}\cdot\hat{g}$ = constant, where g is a fixed vector, describes a line (hyperplane) in the diagram, a single average filter g can be used followed by threshold detection. Alternatively, surface I could be chosen and generated by $\hat{f}\cdot\hat{f}$ = constant, a hypersphere. In this case, surface I is an equi-energy surface and a simple criteria such as requiring the auto-correlation peak of the input to be within a fixed range will provide adequate discrimination. Surface III is another more complex possibility. However, it is more difficult to produce requiring many average filter surfaces and a multichannel system to approximate it. Such techniques are necessary as performance requirements are increased and are essential when the input data has low SNR.

Our interest is in the multiobject case which we illustrate by considering the two vectors $\hat{f}_1$ and $\hat{f}_2$ of Figure 1. The pattern recognition problem is to determine if either f_1 or f_2 is present at the input and reject all other objects. Both $\hat{f}_1 = (a_{11}, a_{12})$ and $\hat{f}_2 = (a_{21}, a_{22})$ lie on a line (plane) which can be specified by $\hat{f}\cdot\hat{g}$ = constant. In particular, g can be seen to be the vector normal to the plane and the constant is $\{\hat{g}\cdot\hat{g}\}^{1/2}$. Thus g has been uniquely specified and is found to be a linear combination of $\hat{f}_1$ and $\hat{f}_2$, i.e.,

$$\hat{g} = b_1\hat{f}_1 + b_2\hat{f}_2 = (b_1 a_{11} + b_1 a_{12})\hat{\phi}_1 + (b_2 a_{21} + b_2 a_{22})\hat{\phi}_2 \tag{6}$$

Thus with g and a simple thresholded output the task is accomplished. This can be extended to more dimensions as outlined below and an average filter h defined to perform multiobject recognition.

Basis function determination

We now consider how the basis functions ϕ_j and the average filter h can be found. For this case, we consider N reference functions $\{g_n\}$ given by

$$g_n(x) = \sum_j b_{nj}\,\phi_j(x) \tag{7}$$

The $\{g_n\}$ will be recognized, if they are in the set $\{f_n\}$ of inputs, by an average filter

$$h(x) = \sum c_i\,\phi_i(x). \tag{8}$$

The correlation outputs for the multiclass pattern recognition case are

$$R_{g_n h}(o) = R_n(o) = g_n \circledast h = \sum_i b_{ni}\,c_i = R_n \tag{9}$$

where (2), (7), and (8) have been used. The objective is to find $\{\phi_j\}$, b_{ni}'s, and finally the c_i's of h such that $R_{g_n h}$ provides the acceptable correlation performance.

We have shift invariance and can assume that the n correlations, R_n, peak at zero for all registered inputs. This "co-location" feature will require shifting each g_n to the correct location when forming h and is acceptable since this is an off-line procedure. This feature allows the weighting of portions of each g_n differently when forming h.

If the Gram-Schmidt[11] procedure is used to select $\{\phi_j\}$, then we find the ϕ_j's from the correlation matrix R_{ij} of the pairs $g_i * g_j$ of $\{g_n\}$. The relationships are:

$$\phi_1(x) = g_1(x)/k_1$$

$$\phi_2(x) = [g_2(x) - R_{12}\phi_1(x)]/k_2$$

$$\vdots$$

$$\phi_n(x) = [g_n(x) - \sum_{j=1}^{n-1} R_{nj}\phi_j(x)]/k_n \tag{10}$$

where the k_n are normalizing constants that are functions of the R_{ij}. With $\{\phi_j\}$ determined, the coefficients b_{ni} in (7) are found. We can then solve the set of N cross-correlation equations in (9) for c_i. For the multiclass case the equations for R_n in (9) are all set equal to a constant. Specific examples of the determination of the R_{ij} correlation matrix, of $\{\phi_j\}$, of b_{ni}, and h follow in the next two sections.

IR tank pattern recognition (determination of correlation matrix R_{ij})

The particular pattern recognition case study chosen to utilize the techniques advanced in the second and third sections of this report was the acquisition of a military tank target from IR sensor imagery independent of the target's orientation. The imagery was taken through the 8-14 micrometer IR window because of the higher and more reliable radiance image variances of this window. The seven tank aspects used as the $\{g_n\}$ reference set are shown in Figure 2.

To generate the correlation matrix R_{ij}, the seven tank images were correlated using a matched spatial filter (MSF) correlator. The MSF technique[12,13] performs a bandpass filter in the correlation process. By varying the spatial frequency u' at which the beam balance ratio K (ratio of the reference to signal beam) is unity, the bandpass can be varied. The resultant peak intensity, I_p, of the optical correlation of each of the five major tank views plotted against u' is shown in Figure 3. From these data, the optimum bandpass filter was found to be one with u' = 2.25 cy/mm. This u' was chosen for all future MSF's.

All pairs of the seven images $\{g_n\}$ in Figure 2 were then auto- and cross-correlated both optically (using the MSF techniques used to determine u') and digitally (using conventional two-dimensional FFT techniques on the same images which were digitized and bandpass filtered at the digital frequency of u' as above). The entire cross-correlation matrix is shown in Figure 4.

The correlation coefficients R_{ij} from Figure 4 were then used to generate the basis functions $\phi_1 - \phi_7$ by the Gram-Schmidt procedure of (10). Shown in Figure 5 are the resulting ϕ_j's. For example, from Figure 5

$$\phi_1 = .642 \times g_1 \tag{11}$$

and inversely $g_1 = 1.56\phi_1$. Furthermore, with the determination of the ϕ_j's, the weights b_{ni} in (7) are determined and found to be the inverse of the table in Figure 5.

IR tank pattern recognition (determination of h)

The coefficients c_j of the average filter, h, in (8) were then computed with the appropriate shifts in the g_n as noted in the third section. The resultant average filter relative weightings are

$$h = 0.64\,\phi_1 + 0.60\,\phi_2 + 0.42\,\phi_3 + 0.93\,\phi_4 + 0.57\,\phi_5 + 0.59\,\phi_6 + 1.85\,\phi_7 \tag{12}$$

A reconstruction of the average filter obtained is shown in Figure 6. This filter was then correlated with all seven of the input images in Figure 2. The peak intensities of all the correlations were in a range from seven to 30. A projection of five cross-sectional scans around the peak of a typical output correlation surface of $g * h$ is shown in Figure 7. All seven correlation surfaces exhibited a sharp correlation peak.

Summary

In pattern recognition problems where a multiclass of objects must be recognized as one class of objects, we have shown, using a hyperspace formulation, that the multiclass discriminate surface can be generated using an average filter. From our hyperspace representation, a method of calculation of such an average filter was directly developed based on an othornormal function expansion. Furthermore, the method was demonstrated using optical processing techniques on an IR pattern recognition problem associated with target acquisition of a tank at multiaspects. A Gram-Schmidt expansion was used as the basis functions and the resultant average filter was correlated with an image set. The filter exhibited good performance with the correlation surfaces themselves possessing the important characteristic sharp peak of correlation detection.

Acknowledgements

The authors would like to acknowledge the US Army Materiel Development and Readiness Command for their sponsorship of Charles Hester at Carnegie Mellon University where much of the above work was done. Also, support for David Casasent and for the facilities used was provided by the Air Force Office of Scientific Research (Grant no. AFOSR-75-2851B).

References

1. Casasent, D., Optical Engineering, Vol. 13, p. 228 (1974).
2. Upatnieks, J., Final Report, Battelle Task No. 0989 (1977).
3. Leib, K. G., et al, Applied Optics, Vol. 17, p. 2892 (1978).
4. Gara, A. D., Applied Optics, Vol. 16, p. 149 (1977).
5. Duda, R. O., and Hart, P. E., Pattern Classification and Scene Analysis, John Wiley and Sons (1973).
6. Christensen, C. R., Upatnieks, J., and Guenther, B. D., US Army Missile Research and Development Command, Technical Report No. T-79-18 (1979).
7. Bode, D. E., and Bratt, P. R., Proceedings of the SPIE, Vol. 95 (1976).
8. Proceedings of the SPIE Conference on IR Technology, Vol. 124 (1977).
9. SPIE Conference on Aerial Reconnaisance, Washington, D.C. (1978).
10. Caulfield, H. J., and Maloney, W. T., Applied Optics, Vol. 8, p. 2354 (1964).
11. Wozencraft, J. M., and Jacobs, I. M., Principles of Communication Engineering, John Wiley and Sons (1965).
12. Casasent, D., and Furman, A., Applied Optics, Vol. 16, pp. 1652 and 1662 (1977).
13. Vander Lugt, A., IEEE, IT-10, p. 139 (1964).

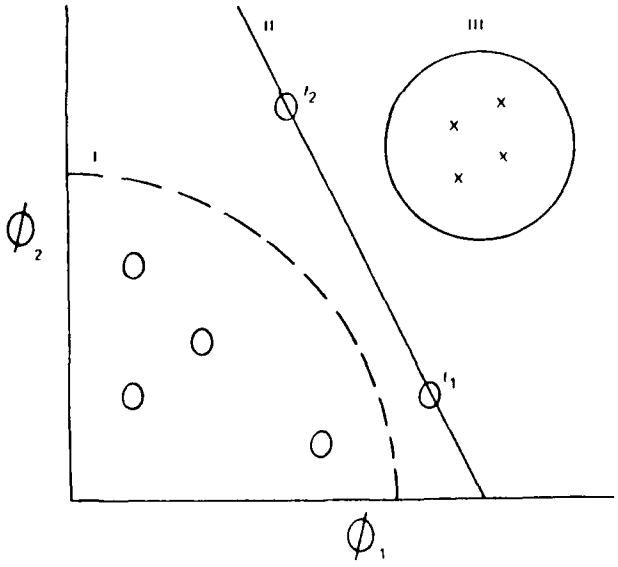

FIGURE 1. TWO-DIMENSIONAL SPACE

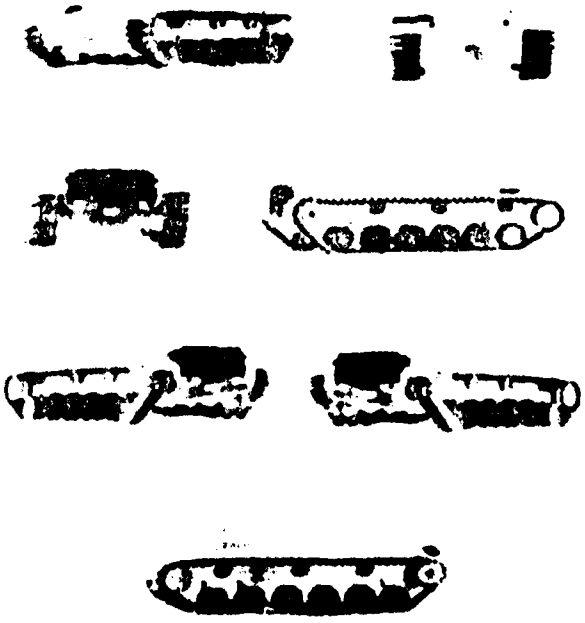

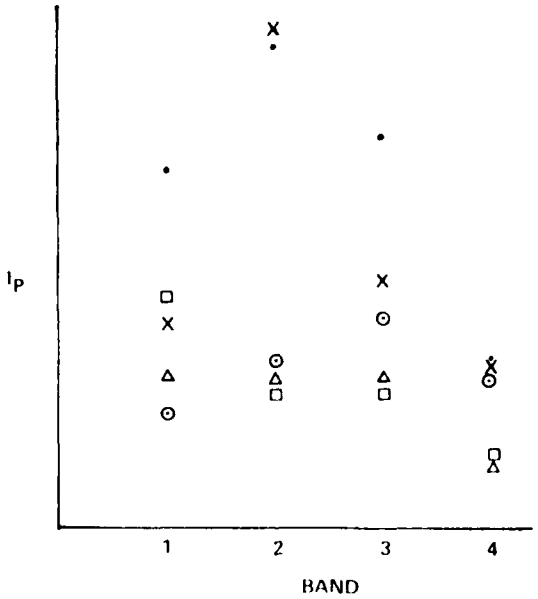

FIGURE 3. I_P VERSUS u'

CORRELATION MATRIX EXPERIMENTAL

ASPECT	1	2	3	4	5	6	7
1	2.42	0.29	0.15	−0.24	−0.09	−0.12	0.10
2	0.29	2.19	0.10	−0.14	−0.10	−0.07	0.06
3	0.15	0.10	4.95	0.02	0.35	0.30	0.03
4	−0.24	−0.14	0.02	1.51	0.04	−0.02	0.04
5	−0.09	−0.10	−0.35	0.04	3.87	0.03	0.02
6	0.12	−0.07	0.30	0.02	0.03	3.93	0.02
7	0.10	0.06	0.03	0.04	0.02	0.02	0.22

FIGURE 4. CORRELATION MATRIX R_{ij}

	g_1	g_2	g_3	g_4	g_5	g_6	g_7
ϕ_1	0.64	–	–	–	–	–	–
ϕ_2	−0.08	0.68	–	–	–	–	–
ϕ_3	−0.02	−0.01	0.44	–	–	–	–
ϕ_4	0.07	0.04	−0.00	0.82	–	–	–
ϕ_5	0.01	0.02	0.03	−0.01	0.51	–	–
ϕ_6	0.02	0.01	0.02	0.01	−0.00	0.50	–
ϕ_7	−0.08	−0.06	−0.01	−0.07	0.01	−0.01	2.1

GRAM-SCHMIDT BASIS

FIGURE 5. GRAM-SCHMIDT COEFFICIENTS

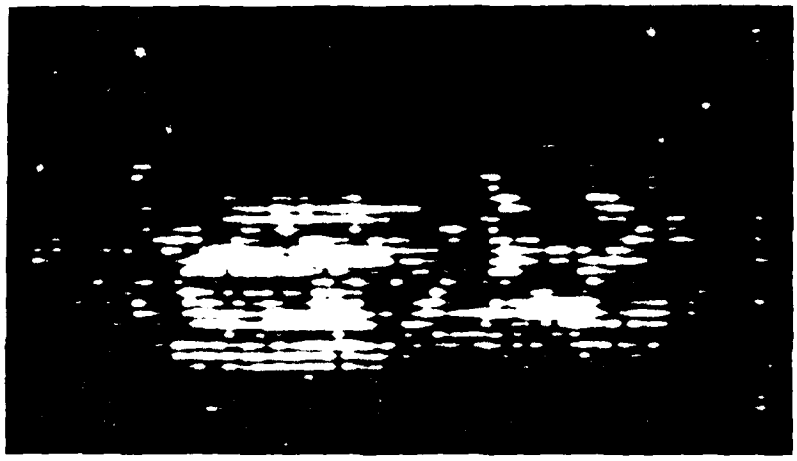

FIGURE 6. RECONSTRUCTED AVERAGE FILTER

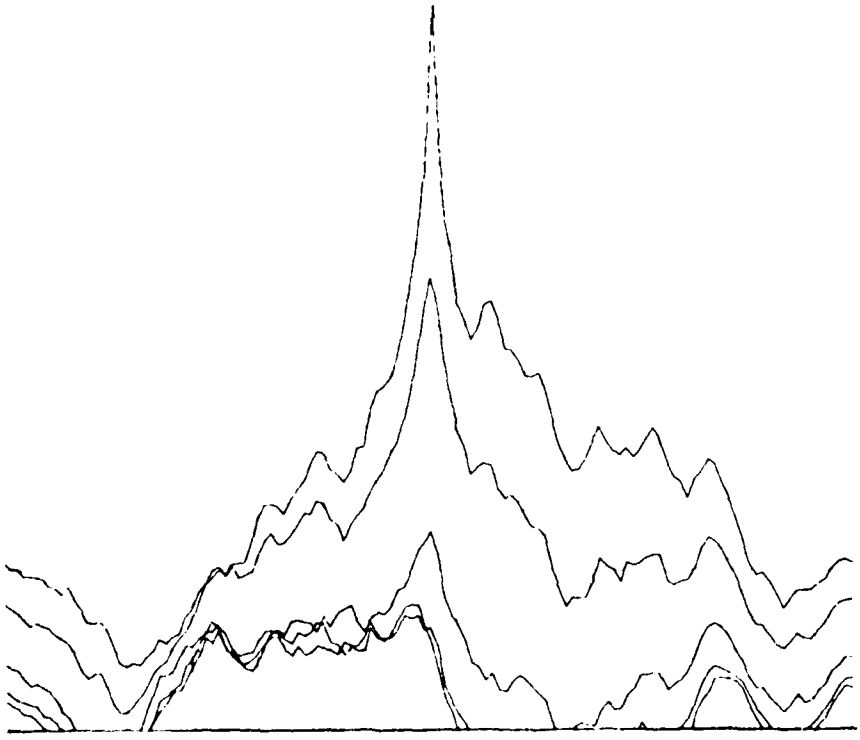

FIGURE 7. AVERAGE FILTER CORRELATION SURFACE

CHAPTER 7

PATTERN RECOGNITION BY INVARIANT MOMENTS

Reprinted from SPIE Vol. 201 – Optical Pattern Recognition
© 1979 by the Society of Photo-Optical Instrumentation Engineers, Box 10, Bellingham, WA 98225 USA

Optical pattern recognition using normalized invariant moments

David Casasent, Demetri Psaltis
Department of Electrical Engineering, Carnegie-Mellon University
Pittsburgh, Pennsylvania 15213

Abstract

A novel approach to coherent optical pattern recognition is described. It does not utilize matched spatial filters and optical correlation methods. Rather, a 2-dimensional input function is described in terms of its absolute normalized invariant moments. Comparison of these moments enables one to determine the presence of a given object independent of geometrical distortions. A parallel optical processor with a special mask is used to generate all moments for a 2-D scene in parallel. A simple digital post processor calculates the actual absolute normalized invariant moments with the high dynamic range necessary. Our initial work reported upon here has concentrated on: the optical generation of individual moments, how the individual moments vary, the dynamic range requirements of the system and how they may best be met in a hybrid optical digital topology, and methods to generate all moments optically in parallel.

1. Introduction

The flexibility of coherent optical pattern recognition systems and the repertoire of operations possible on these systems have greatly improved in recent years [1]. Optical pattern recognition has long relied on the Fourier transform and matched spatial filter correlation operations inherently possible in an optical computer [2]. The purpose of the present research program was to develop a new approach to optical pattern recognition that did not rely on the Fourier transform and matched spatial filter systems that have been used for so long. Recent research in matched spatial filter [3] and space variant [4] optical pattern recognition has concentrated on practical pattern recognition problems, namely maintaining correlation when the input and reference are not equal. Geometrical differences between the input and reference scene are the major cause of correlation performance degradation.

In this paper, we describe a novel coherent optical pattern recognition technique that appears to allow pattern recognition independent of any geometrical differences between the input and reference scene. The technique we employ is to represent an image by its absolute normalized invariant moment. This approach has its origin in the mathematical literature on algebraic invariants [5] and moment invariants [6]. Several recent digital processing programs in this area have been reported [7-9]. These recent works have shown the usefulness of this technique in pattern recognition, but the computational load involved in the calculation of the moments has impeded further progress.

In this paper we present: a less mathematical, revised formulation of the theory of invariant moments (Section 2); a detailed numerical case study using a simple square input function (Section 3); the design and fabrication of a coherent optical system to generate individual moments for a 2-D input pattern and; initial experimental results obtained on our system (Section 4). An optical system to generate all moments in parallel is then briefly discussed together with an analysis of the required system dynamic range. This results in the design of an optimum hybrid optical/digital system for pattern recognition using absolute normalized invariant moments (Section 5).

2. Theoretical basis

The theory of algebraic invariants [5] begins by the description of a homogeneous polynomial of u and v as a binary algebraic form or more simply as a binary form of order p

$$a_{p0}u^p + \binom{p}{1} a_{p-1,1} u^{p-1} v + \binom{p}{2} a_{p-2,2} u^{p-2} v^2 + \dots + \binom{p}{p-1} a_{1,p-1} uv^{p-1} + a_{0p} v^p \tag{1}$$

The more compact notation:

$$\left(a_{p0};\ a_{p-1,1};\ \dots;\ a_{1,p-1};a_{0p}\right) (u,v)^p \quad . \tag{2}$$

for this polynomial is preferable. This homogeneous polynomial of the coefficients a_{p0} is said to be an algebraic invariant of weight w if:

$$I(a'_{p0}, \dots, a'_{0p}) = \Delta^w I(a_{p0}, \dots, a_{0p}) , \tag{3}$$

where a'_{pn} are the coefficients of the polynomial expansion after the general linear transformation

$$\begin{bmatrix} u \\ v \end{bmatrix} = \begin{bmatrix} \alpha & \gamma \\ \beta & \delta \end{bmatrix} \begin{bmatrix} u' \\ v' \end{bmatrix} , \quad \Delta = \begin{vmatrix} \alpha & \gamma \\ \beta & \delta \end{vmatrix} \neq 0. \tag{4}$$

In (4) Δ is the determinant of the coordinate transform and for absolute invariance we require $w = 0$. The basic idea associated with algebraic invariants is to describe a general geometrical distortion in terms of (4) and to then determine the relationship that the coefficients a_{pn} and a'_{pn} must satisfy.

The moment generating function of a 2-D input function $f(x,y)$ is

$$M(u,v) = \iint_{-\infty}^{\infty} \exp(ux+vy)\ f(x,y)dxdy \tag{5a}$$

$$= \sum_{p=0}^{\infty} \sum_{q=0}^{\infty} m_{pq} \frac{u^p}{p!} \frac{v^q}{q!} \tag{5b}$$

$$= \iint_{-\infty}^{\infty} \sum_{p=0}^{\infty} \frac{1}{p!} (ux+vy)^p\ f(x,y)dxdy \tag{5c}$$

$$= \sum_{p=0}^{\infty} \frac{1}{p!} (m_{p0}, \ldots, m_{0p})(u,v)^p\ . \tag{5d}$$

This operator is most useful in determining the moment invariants. The integral form in (5a) is the fundamental definition. The moments m_{pq} of a 2-D function $f(x,y)$ are defined by

$$m_{pq} = \iint_{-\infty}^{\infty} x^p y^q f(x,y)dxdy\ ,\quad p,q = 0,1,2\ldots \tag{6}$$

From this definition we can express M as a power series expansion of the moments m_{pq} as in (5b). Expanding the exponential term in (5a) in a power series, (5c) results. Interchanging the order of integration and summation, the compact notation [6] in (5d) results.

The general formulation procedure to determine the invariant moments uses the algebraic invariants and moment generating function concepts. The basic approach is to apply the general linear transformation

$$\begin{bmatrix} x' \\ y' \end{bmatrix} = \begin{bmatrix} \alpha & \beta \\ \gamma & \delta \end{bmatrix} \begin{bmatrix} x \\ y \end{bmatrix} \tag{7}$$

to $f(x,y)$. A new M'_1 moment generating function results. Applying the coordinate transformation in (4) to M, we obtain a new $M_1(u',v')$ of the same functional form as M. Rewriting M and M_1 in the form of (4) and equating coefficients, the relationships necessary to make M_{pq} and M'_{pq} (the moments of the original and coordinate transformed functions) equal are obtained. The proper combinations of several moments can then be selected such that they are independent of the indicated coordinate transformation. This general procedure thus involves application of (7) to $f(x,y)$ to yield $f_1(x',y')$ and a new M'_1 and application of (4) and (7) to (5c). This yields a moment generating function

$$M_1(u',v') = \iint_{-\infty}^{\infty} \sum_{p=0}^{\infty} \frac{1}{p!} (u'x'+v'y')^p f(x',y')(1/|J|)dx'dy'. \tag{8}$$

where J is the Jacobian of the coordinate transformation in (7). (For a linear coordinate transformation, $J=\Delta$, the determinant). Note that application of (4) and (7) to (5c) is equivalent to the application of (7) to (5c) with the coefficients of x' and y' in the coordinate transformation factor $(ux+vy)$ equal to u' and v'. Note also that the choice of the coordinate transformations in (4) and (7) are such that

$$(ux+vy) = (u'x'+v'y'). \tag{9}$$

Since M and M_1 are of the same form as in (5c) and (8), we can express them as in (5d). Using (9), the coefficients in these two coordinate transformed versions of M and M_1 can be compared and the moments of order p have the same invariance as in (3) with an added factor J as in:

$$I(m'_{p0},\ldots,m'_{0p}) = |J|\Delta^w I(m_{p0},\ldots,m_{0p}). \tag{10}$$

The basic conclusion is the formulation in (10) and the general procedure described. Use of this technique is best demonstrated by example. This is provided in Section 3.

3. Case study

Specific cases of translation, scale, and rotation invariance are analyzed in general terms in Sections 3.1-3.3. The absolute normalized invariant moments (Section 3.4) then result.

3.1 Translational invariance

Under the coordinate transformation (11)

$$x' = x+\alpha \qquad y' = y+\beta \qquad \alpha,\beta = \text{constants}, \tag{11}$$

where α and β are the shift variables, the central moments μ_{pq} =

$$\mu_{pq} = \iint_{-\infty}^{\infty} (x-\bar{x})^p (y-\bar{y})^q f(x,y)\,d(x-\bar{x})\,d(y-\bar{y}), \tag{12}$$

where the centroid of f is described by

$$\bar{x} = m_{10}/m_{00}, \quad \bar{y} = m_{01}/m_{00} \tag{13}$$

are invariant under a coordinate translation. The central moments μ_{pq} can thus be expressed in terms of the ordinary moments m_{pq} (for the first four terms) by

$$\begin{aligned}
\mu_{00} &= m_{00}, & \mu_{11} &= m_{11} - \bar{y}m_{10} \\
\mu_{10} &= 0, & \mu_{30} &= m_{30} - 3\bar{x}m_{20} + 2m_{10}\bar{x}^2 \\
\mu_{01} &= 0, & \mu_{12} &= m_{12} - 2\bar{y}m_{11} - \bar{x}m_{02} + 2\bar{y}^2 m_{10} \\
\mu_{20} &= m_{20} - \bar{x}m_{10} & \mu_{21} &= m_{21} - 2\bar{x}m_{11} - \bar{y}m_{20} + 2\bar{x}^2 m_{01} \\
\mu_{02} &= m_{02} - \bar{y}m_{01} & \mu_{03} &= m_{03} - 3\bar{y}m_{02} + 2\bar{y}^2 m_{01}
\end{aligned} \tag{14}$$

It can be shown [6] that no differences result if M is described using μ rather than m.

3.2 Scale invariance

Under a scale transformation (scale factor a)

$$\begin{bmatrix} x' \\ y' \end{bmatrix} = \begin{bmatrix} a & 0 \\ 0 & a \end{bmatrix} \begin{bmatrix} x \\ y \end{bmatrix}, \quad a = \text{constant}, \tag{15}$$

the moment generating functions M and M_1 can be expressed in the form of (5b). Equating coefficients in these expressions, we find the moments

$$\eta_{pq} = \frac{m_{pq}}{m_{00}^{1+(p+q)/2}} \tag{16}$$

to be invariant to a scale change and the moments

$$\nu_{pq} = \frac{\mu_{pq}}{\mu_{00}^{1+(p+q)/2}} \tag{17}$$

to be invariant to both a scale and translational change.

3.3 Rotational invariance

The rotational transformation

$$\begin{bmatrix} x' \\ y' \end{bmatrix} = \begin{bmatrix} \cos\theta & \sin\theta \\ -\sin\theta & \cos\theta \end{bmatrix} \begin{bmatrix} x \\ y \end{bmatrix} \tag{18}$$

can be achieved by describing M and M_1 in terms of μ and m and μ' and m' in the form of (5b). Comparing coefficients between m and m' or μ and μ' in these M and M_1 equations yields the desired moments. Reformulation of the coordinate transformation by proper redefinition of (u,v) axes greatly simplifies the procedure. The resultant rotational invariant moments become

$$
\begin{aligned}
\rho_1 &= m_{20} + m_{02} \\
\rho_2 &= (m_{20}-m_{02})^2 + 4m_{11}^2 \\
\rho_3 &= (m_{30}-3m_{12})^2 + (3m_{21}-m_{03})^2 \\
\rho_4 &= (m_{30}+m_{12})^2 + (m_{21}+m_{03})^2 \\
\rho_5 &= (m_{30}-3m_{12})(m_{30}+m_{12})[(m_{30}+m_{12})^2 - 3(m_{21}+m_{03})^2] \\
&\quad + (-m_{03}+3m_{21})(m_{03}+m_{21})[(m_{03}+m_{21})^2 - 3(m_{12}+m_{30})^2].
\end{aligned} \tag{19}
$$

3.4 Absolute invariant moments

Combining the results of the three prior subsections, the absolute normalized invariant moments (invariant to position, scale, and rotation) are obtained by replacing m_{pq} in (19) with

$$\eta_{pq} = \frac{\mu_{pq}}{(\mu)^{1+(p+q)/2}} \tag{20}$$

The first seven absolute normalized invariant moments are then:

$$
\begin{aligned}
\phi_1 &= \eta_{20} + \eta_{02} \\
\phi_2 &= (\eta_{20} - \eta_{02})^2 + 4\eta_{11}^2 \\
\phi_3 &= (\eta_{30}-3\eta_{12})^2 + (3\eta_{21} + \eta_{03})^2 \\
\phi_4 &= (\eta_{30}+\eta_{12})^2 + (\eta_{21} + \eta_{03})^2 \\
\phi_5 &= (\eta_{30}-3\eta_{12})(\eta_{30}+\eta_{12})[(\eta_{30}+\eta_{12})^2 - 3(\eta_{21}+\eta_{03})^2] \\
&\quad + (3\eta_{21}-\eta_{03})(\eta_{21}+\eta_{03})[3(\eta_{30}+\eta_{12})^2 - (\eta_{21}+\eta_{03})^2] \\
\phi_6 &= (\eta_{20}-\eta_{02})[(\eta_{30}+\eta_{12})^2 - (\eta_{21}+\eta_{03})^2] \\
&\quad + 4\eta_{11}(\eta_{30}+\eta_{12})(\eta_{21}+\eta_{03}) \\
\phi_7 &= (3\eta_{12} - \eta_{30})(\eta_{30}+\eta_{12})[(\eta_{30}+\eta_{12})^2 - 3(\eta_{21}+ \eta_{03})^2] \\
&\quad + (3\eta_{21}-\eta_{03})(\eta_{21}+\eta_{03})[3(\eta_{30}+\eta_{12})^2 - (\eta_{21} + \eta_{03})^2]
\end{aligned} \tag{21}
$$

3.5 Case study

As specific numerical example, consider an input square extending from $x_1 = 1$ to $x_2 = 2$ and $y_1 = 0$ to $y_2 = 1$ as in Figure 1. Its ordinary moments obtained from (6) are listed in Table 1. Since $m_{00} = 1$, the moment m_{10} and m_{01} describe the centroid of the function. The central moments μ_{pq} are also included in Table 1 computed using (12) where $\bar{x} = m_{10}/m_{00} = 1.5$ and $\bar{y} = m_{01}/m_{00} = 0.5$ from (13). Under translation to coordinates $x_1 = 4$ to $x_2 = 5$ and $y_0 = 0$ to $y_1 = 1$, the normalized central moments $\eta_{pq} = \mu_{pq}/\mu_{00}^{y}$ where $y = 1+(p+q)/2$ are found. The resulting ϕ_n moments with $\mu_{20} = 1$ are also given in Table 1. Comparing these ϕ_n moments, we see the invariance of ϕ_n to translation of the input. For rotation of the input as in Figure 3, $\bar{x} = -0.5$ and $\bar{y} = +1.5$, the ϕ_n values are shown in Table 1. The same ϕ_n values again result. A scale change by $a = 2$ as in Figure 4 (with $\bar{x} = 3$, $\bar{y} = 1$ and $\mu_{00} = 4$) yield identical ϕ_n values again as shown. For this example, and with considerable algebraic manipulation, the absolute invariance of the seven functions ϕ_n is confirmed.

4. Optical system design and experimental demonstration

The coherent optical system used to realize (6) is shown in Figure 5. The simplicity of the system is one of its prime features. The input function $f(x,y)$ is placed at P_1, illuminated with coherent laser light, and imaged onto a mask $g(x,y)$ at P_2. Leaving P_2, the light distribution is fg. Lens L_3 forms the Fourier transform of the product fg and on-axis at P_3 we find

$$u_3(0,0) = \iint f(x,y)g(x,y)dxdy. \tag{22}$$

If the mask at P_2 is absent, $g = 1$ and the output is m_{00}.

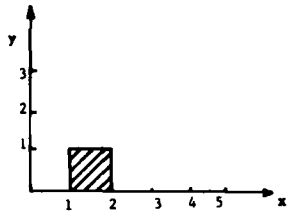

Fig.1. Original Input

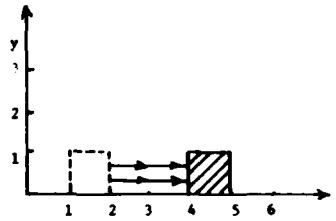

Fig.2. Translated Input

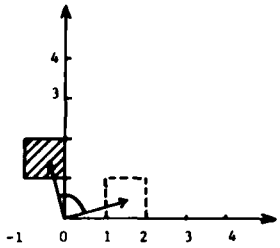

Fig.3. Rotated Input

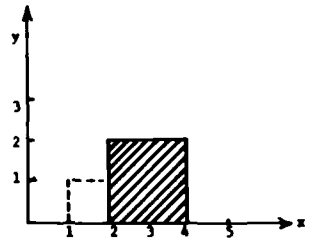

Fig.4. Scaled Input

NUMERICAL CASE STUDY EXAMPLE

Table 1

THEORETICAL CASE STUDY (SQUARE INPUT)

n	(p,q)	ORIGINAL m_{pq}	ORIGINAL μ_{pq}	ORIGINAL ϕ_n	TRANSLATED (ϕ_n)	ROTATED (ϕ_n)	SCALED (ϕ_n)
1	00	1	1	0.166	0.166	0.166	0.166
2	10	1.5	0	0	0	0	0
3	01	0.5	0	0	0	0	0
4	20	0.33	0.083	0	0	0	0
5	02	0.33	0.083	0	0	0	0
6	30	3.75	0	0	0	0	0
7	03	0.25	0	0	0	0	0
	11	0.75	0				
	21	1.66	0				
	12	0.5	0				

m_{pq} = ordinary moments

μ_{pq} = central moments

ϕ_n = invariant moments

$$u_3(0,0) = \iint f(x,y)dxdy = m_{00}. \tag{23a}$$

When the mask at P_2 is a simple linearly graded transmittance function $g = x$ or $g = y$, the output at P_3 is m_{10} or m_{01} respectively. If the $g = x$ and $g = y$ masks are superimposed, $g = xy$ results and the output is

$$u_3(0,0) = \iint f(x,y)xy\ dxdy = m_{11}. \tag{23b}$$

Continuing in this manner, we see that all the ordinary moments m_{pq} of the 2-D function $f(x,y)$ can be generated with the appropriate masks $g(x,y)$.

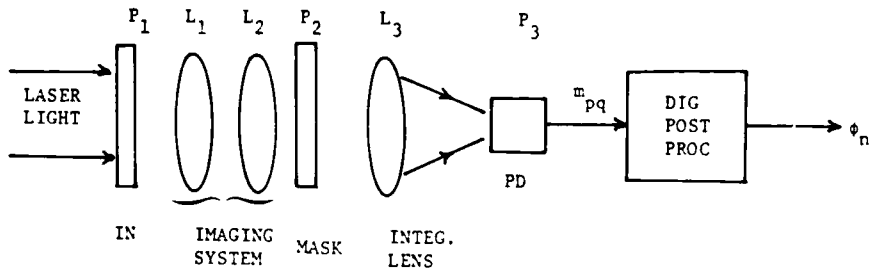

Fig. 5 Hybrid optical/digital system to compute the absolute normalized invariant moments.

In the system shown in Figure 5, the ordinary moments m_{pq} are computed by the optical system. The absolute normalized invariant moments ϕ_n are then calculated from these optically produced outputs in a high dynamic range and accurate special-purpose digital post processor.

The mask functions $x^p y^q$ should be bi-polar. This can be achieved by using a positive amplitude mask with a $\lambda/2$ phase retarding plate in one-half of the P_2 plane. In our present experiments, the location of the input function was restricted to the right half of the input plane so that a unipolar positive mask could be used. A computer controlled cathode ray tube with 10 point correction for the nonlinear t-E film characteristics was used to generate the necessary $g=x$, $g-x^2$, etc. mask patterns needed. These mask patterns were then photographed from the CRT surface and inserted in P_2 of the system shown in Figure 5. Because the film masks used did not have perfect transmittance t=1 or perfect absorption t=0 where necessary, direct computation of m_{pq} was not possible, rather modified m''_{pq} moments were produced. To compare our experimental data, the normalized moments m''_{00}/m''_{pq} were calculated from our measured m''_{pq} values and compared to the theoretically obtained ones. The simple square inputs used are shown in Figures 6-9. Cross-sectional scans of the P_3 output obtained with a scanning photometric microscope interfaced to a high dynamic range PMT and chart recorder are shown in Figure 10. The comparative experimental and theoretical data are provided in Table 2. As seen from Table 2, the comparison between theory and experiment is good. These initial experiments were thus most promising.

5. Discussion and advanced system considerations

A general analysis of the dynamic range of the first ten ordinary moments m_{pq} was conducted, from which m_{pq} was seen to decrease for higher orders and to be inversely proportional to the input space bandwidth product (for a fixed input size). For the case of a 25 mm input aperture and a 20 cy/mm input function, the worst case $m_{pq}(max)/m_{pq}(min)$ dynamic range was found to be 42 dB. This range is easily satisfied by existing photo detectors. The corresponding dynamic range of the first seven invariant moments ϕ_n was a far larger 191 dB. The hybrid optical/digital system shown in Figure 5 appears to be the best practical system that utilizes the optical system for the low accuracy and dynamic range computations of the m_{pq} values and a special-purpose digital post processor for the high accuracy and dynamic range computations of the ϕ_n values.

The use of the masks $(1+x^p y^q)$ for the generation of the ordinary moments introduces output bias levels that greatly increase the required photo detector dynamic range and complicate the post processing required. The necessity for bi-polar masked transmittance functions or restricted input function positional locations is another disadvantage of the present system. Moreso, separate masks are necessary for each m_{pq} to be calculated. We have thus considered an alternate system design in which all moments can be generated in parallel without the dynamic range, bias level, and positive/negative polarity problems associated with the prior system. The concept of this system can be seen by:

(1) replacing x and y in (6) by $x \exp(j\omega_0 x)$ and $y \exp(j\omega_0 y)$ respectively, and

(2) use of a Fourier transform rather than integrating lens and multiple output detectors rather than a single on-axis photo-diode as in Figure 5.

The resultant output plane and m_{pq} equation then becomes:

$$m_{pq} = \iint x^p y^q \exp[-j(p\omega_0 x + q\omega_0 y)]\, t(x,y) \exp[-j(\omega_x x + \omega_y y)]\, dx\, dy \tag{24}$$

From (24), we see that each m_{pq} is now spatially separated at the output Fourier transform plane locations

$$(\omega_x, \omega_y) = (p\omega_0, q\omega_0). \tag{25}$$

The required mask is complex. However, it can be produced by use of two real masks $t_A = \exp(x \cos \omega_0 x)$ and $t_B = 1+\cos(x \sin \omega_0 x + \omega_1 x)$. After single sideband filtering t_B and tilting the optical axis appropriately, the filtered complex output $\exp(jx \sin \omega_0 x)$ is obtained and imaged onto t_A and the input function $f(x,y)$. The Fourier transform of this pattern is then formed and (24) results in the output plane. All m_{pq} values

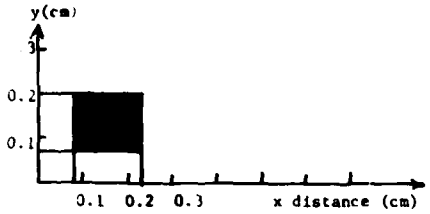

Fig.6. Input

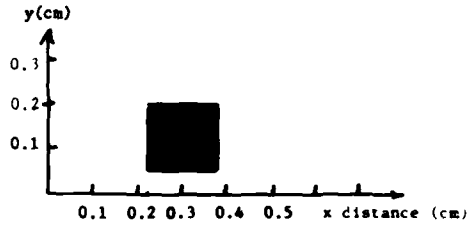

Fig.7. Translated input

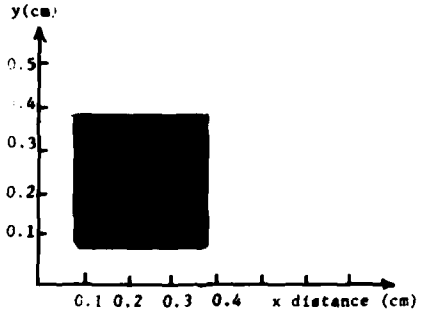

Fig.8. Scaled input

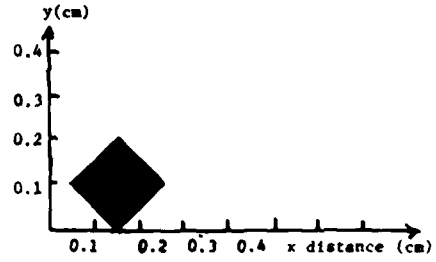

Fig.9. Rotated input

Table 2. Comparison of theoretical and experimental m_{pq} moment computations.

NORMALIZED MOMENT	ORIGINAL		TRANSLATED		SCALED		ROTATED	
	THEORY	EXPERIM	THEORY	EXPERIM	THEORY	EXPERIM	THEORY	EXPERIM
m''_{00}/m''_{10}	2.28	2.27	2.0	1.65	2.16	1.82	2.37	1.71
m''_{00}/m''_{20}	5.03	5.2	4.32	4.64	4.4	5.16	5.62	5
m''_{00}/m''_{11}	5.25	6.7	4.87	5.8	4.7	5.3	5.4	6
m''_{00}/m''_{30}	11.16	11.7	8.9	9.5	9.8	12.8	11.8	11.8
m''_{00}/m''_{21}	11.62	12.3	9.7	10.4	10.2	11.8	11.25	12.1

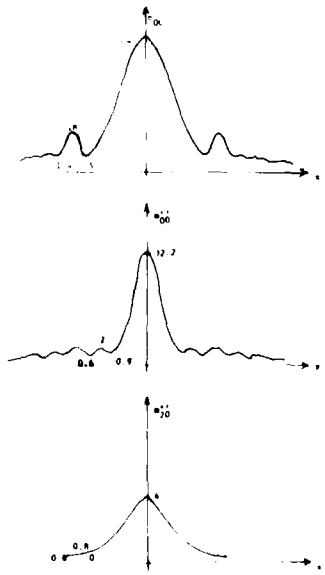

Fig. 10 Cross-sectional scans of the P_3 outputs in Figure 5 for several m''_{pq} functions.

are generated in parallel and are spatially separated in the output transform plane. The required mask and its resolution specifications are greatly simplified if only the first ten ordinary moments m_{pq} are required, as appears to be the case.

ACKNOWLEDGEMENTS

The support of this research by the Air Force Office of Scientific Research on Grant AFOSR-75-2851 is gratefully acknowledged.

REFERENCES

1. J.D. Goodman, Proc. IEEE, 65, 29 (1977).
2. A. Vander Lugt, IEEE, IT-10, 139 (1964).
3. D. Casasent and A. Furman, Applied Optics, 16, 1652, 1662 (1978).
4. D. Casasent and D. Psaltis, Proc. IEEE, 65, 77 (1977).
   D. Casasent and D. Psaltis, pp. 291-356 in Progress in Optics, Volume XVI (E. Wolf, editor, North Holland Publishing Co., Amsterdam, 1978).
5. G.B. Curevich, Foundations of the Theory of Algebraic Invariants, P. Noardhoff Ltd., Groningen, Netherlands (1964).
6. M.K. Hu, IRE, IT-8, 179, February (1962).
7. R. Wong and E. Hall, Comput. Graphics and Image Processing, 8, 16 (1978).
8. S. Dudani, K. Breeding and R. McGhee, IEEE, C-26, 39 (1977).
9. S. Maitra, Proc. IEEE, 67, No. 4, 697 (1979).

CHAPTER 8

COHERENT OPTICAL PATTERN RECOGNITION

Coherent Optical Pattern Recognition

DAVID CASASENT

Reprinted from Proceedings of the IEEE, Vol. 67, No. 5, May 1979
0018-9219/79/0500-0813$00.75 © 1979 IEEE

Coherent Optical Pattern Recognition

DAVID CASASENT, FELLOW, IEEE

Abstract—Pattern-recognition systems, techniques, and applications using coherent optical systems are reviewed. Many optical pattern-recognition system architectures exist that include time-domain optical correlators and the optical joint transform correlator and refinements in the original optical matched spatial filter synthesis processor. Advanced optical pattern-recognition systems are also described such as hybrid optical/digital processors and diffraction-pattern sampling systems using specially shaped Fourier plane detector arrays. The optical space-variant pattern-recognition systems described are examples of the growing repertoire of operations now achievable in optical computers.

I. Introduction

THE BASIS of coherent optical Fourier transform (FT) theory began with the microscopy image resolution work of Abbe [1], the spatial-filtering experiments of Porter [2], and the phase-contrast microscope of Zernike [3]. However, it was Marechal and Croce [4] in 1953 who provided the basic analysis of coherent optical systems in terms of spatial-frequency response and thus gave new meaning to the work of Abbe. Significant developments in optical spatial filtering began with the marriage of communications theory and optics in the classic work of O'Neill [5] who unified much of the earlier research.

The objective of the types of pattern-recognition systems to be discussed is to determine the presence (and usually the location) of a key object or signal within an input containing other data (referred to as noise). Depending on the specific application, the pattern-recognition problem can be classified as the extraction of a signal buried in noise, character recognition in which one or several members of a given set are searched for, or the location of one key object in diverse backgrounds. Turin [6] provides an excellent description of matched filters for such diverse scenarios.

Optical pattern recognition, as one generally views it today, began with the optical realization of a complex matched spatial filter by vander Lugt [7]. This work was based upon sidelooking radar-processing concepts developed by Cutrona *et al.* [8] and the holography work of Leith and Upatnieks [9] These early successes and developments, plus the commercial availability of continuous-wave lasers caused a rapid maturing in the field of optical data processing.

Many developments have occurred in the fifteen years since the first optical matched filtering paper. The intrigue of processing data in parallel and in real-time has captured the imagination and tapped the inventiveness of many researchers. This has led to an increasing repertoire of coherent optical pattern-recognition systems and techniques. In this survey paper, we provide a vitally needed summary of optical pattern recognition over these recent fifteen years, and a consolidated summary of the system architectures [10], operations achievable [11], and applications [12]-[15] of this aspect of the more general field known as optical computing [14].

Cutrona *et al.* [16] describe a wealth of optical pattern-recognition system architectures and their use in signal processing. When coded signal waveforms are used, signal-processing systems become multichannel 1-*D* versions of the more conventional 2-*D* pattern-recognition topologies, and we thus include advancements in such work in this survey.

Optical pattern recognition is but one aspect of the larger field of optical computing [14]. Space does not permit detailed discussions of all optical techniques related and associated with pattern recognition. Recent advances in non-coherent optical pattern recognition are discussed elsewhere [17]. Similarly, image enhancement and restoration techniques [18] and image deblurring methods [19], [20] in which the output is a corrected image are not discussed. Rather, preference is given to systems whose output contains the final desired pattern-recognition decision and data. We will concentrate on coherent optical-processing systems in which the optical system itself performs the actual processing and the pattern recognition of the data, rather than serving only as the data collection vehicle or as an image enhancement preprocessor.

In the type of coherent optical processor considered in this paper, the data to be processed is assumed to be an image or some similar two-dimensional pattern. This input data is entered into the optical processor as a transparency, e.g., a 35-35-mm slide of the input scene. Such a transparent pattern is then illuminated with parallel coherent (laser) light of uniform amplitude (spatially). This spatially uniform light passes through the transparent input medium and emerges spatially modulated in amplitude proportional to the two-dimensional amplitude transmittance pattern recorded on the input medium. This process is thus quite analogous to the operation of a simple slide-projector, but yet demonstrates the two-dimensional feature of such processors.

However, because the input illumination used is coherent laser light, a multitude of operations quite useful in pattern recognition are obtainable. The fundamental operation performed in such coherent optical processors is the Fourier transform (FT) (Section II). As the input data is a spatial pattern rather than temporal, we represent it in 1-*D* by $f(x)$ and in 2-*D* by $f(x_1, y_1)$. Thus in optics, we speak of a spatial FT, in which distance in the input data plane is directly analogous to time in the more conventional temporal FT. As we describe in subsequent sections, the normal linear-systems operations of correlation and convolution (often used in pattern recognition) can be realized in such optical processors. For now

Manuscript received May 16, 1978; revised October 4, 1978. This work was supported by the Air Force Office of Scientific Research under Contract AFOSR75-2851, administered by the Air Force Systems Commands; the Office of Naval Research under Contract NR-366-005; and the National Science Foundation under Contract ENG77-20038; and other agencies for much of the author's work included in this survey.

The author is with the Department of Electrical Engineering, Carnegie-Mellon University, Pittsburgh, PA 15213.

0018-9219/79/0500-0813$00.75 © 1979 IEEE

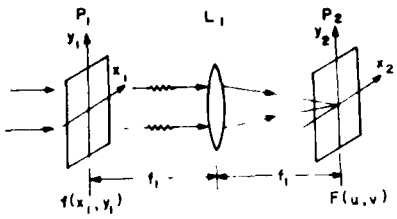

Fig. 1. Schematic of the conventional optical FT system.

we only note that these operations are realizable on two-dimensional input data and in parallel (i.e., the input light operates in parallel on all pixels of data present in the input plane).

The ability of an optical processor to operate in parallel on 2-*D* input data and to perform operations such as the FT, correlation and convolution, is why such systems have been considered for pattern recognition and other applications. The final feature of such systems that makes them attractive alternatives to digital processors is the speed with which these parallel operations can be performed. The coherent laser light is used only as the optimum carrier upon which to modulate or impress the input data and as the information bearing carrier that flows through the system. The speed with which this light carrier moves is roughly 1 ns/ft (1 ns = 10^{-9} s). Thus for a three-foot optical system, the required processing time for parallel 2-*D* pattern-recognition operations would be 3 ns (excluding input data recording and output data detection times). It is too premature and early in the development of optical processors and not the purpose of this paper to expand upon the size, weight, and cost effectiveness of such systems compared to digital or other alternative analog methods. It is also not the purpose of this paper to compare optical and digital pattern-recognition systems. Rather, our emphasis is to convey the operations achievable and to summarize recent progress made in optical pattern-recognition research.

II. Optical Fourier Transform

The basic operation in nearly all coherent optical systems is the FT. It is well known [21] that if an input transparency with amplitude transmittance $f(x_1, y_1)$, placed in the front-focal plane P_1 of a spherical lens L_1 (of focal length f_L), is illuminated with collimated coherent laser light (of wavelength λ), then the light amplitude distribution in the back-focal plane P_2 of L_1 is the complex 2-*D* FT of $f(x_1, y_1)$. We represent the 2-*D* optical spatial-FT of $f(x_1, y_1)$ by $F(u, v)$, where

$$F(u, v) = \frac{1}{\lambda f_L} \iint_{-\infty}^{+\infty} f(x_1, y_1) \exp\left[j2\pi(ux_1 + vy_1)\right] dx_1\, dy_1. \tag{1}$$

The schematic of this simple optical-FT system is shown in Fig. 1. We denote space functions by lower case variables (e.g., f, g, h) and their FT's by the corresponding upper case variables (e.g. F, G, H). Distances in the input plane P_1 are denoted by (x_1, y_1). The spatial distances (x_2, y_2) in the FT plane P_2 are related to the spatial frequencies (u, v) present in the input plane P_1 data by

$$u = x_2/\lambda f_L \qquad v = y_2/\lambda f_L \tag{2}$$

where the units of x and y are typically millimeter and the units of u and v are cycles per millimeter (analogous to cycles/time or Hertz in the conventional temporal FT).

Fig. 2. Example of the optical FT. The inserts show the FT of the corresponding regions of the input plane P_1 pattern [13]. The direction, velocity, and amplitude of the ocean waves can be found from these FT data.

An understanding of the anatomy of an optical FT is vital to obtain the insight necessary to follow the future operations and applications to be discussed. In general, the transmittance of P_1 must be real and positive and thus input data must be recorded on a bias (the acoustooptical transducers discussed in Section III and film-thickness variations, which we ignore, are exceptions). Thus if the input is a sinewave, its optical FT at P_2 appears as a dc spot on-axis plus two symmetrically located spots of light on each side of dc. The locations $\pm x_2'$ of these two spots correspond to the input spatial frequency u' of the sinewave as in (2). If the input sinewave is recorded horizontally (vertically), the FT-plane spots appear along the horizontal u or x_2 axis (vertical v or y_2 axis) at P_2. If the frequency u' of the input sinewave is increased (decreased), the separation of the two off-axis FT-plane spots from the origin of P_2 increases (decreases). If the input sinewave is recorded at +45° to the input x_1 axis, the spots of light comprising the FT-pattern occur on a line inclined at −45° to the x_2 axis of the FT plane.

Thus the location of a spot of light in the optical FT-plane P_2 indicates the presence of a given spatial frequency in the input data, as well as the orientation of this data in the input plane. The amplitude of each spot of light in P_2 indicates the amount of that spatial frequency component present in the input data. Low spatial frequencies lie closer to the origin of P_2.

A simple example of the information content available in the optical FT plane pattern is shown in Fig. 2. This figure shows an aerial photograph of a portion of the Caribbean with the optical FT-pattern of various regions of the input shown in the inserts [13]. Close examination of each FT-pattern will show a series of spots of light at different orientations. The direction of the FT-light pattern indicates the direction of the ocean currents and the spacing of the spots indicates the velocity of the ocean currents in the corresponding region of the input scene.

Although the classic optical pattern-recognition system one envisions is a correlator topology, pattern recognition can often be achieved by analysis of the contents of the FT plane alone. When such a simplified optical system is usable, it is clearly preferable to the more sophisticated optical correlators to be described later. The optical FT pattern is usually referred to as the diffraction pattern. We now consider a diffraction-pattern system for pattern recognition that uses a unique frequency plane detector at P_2 of Fig. 1.

A. Pattern Recognition by Diffraction Pattern Sampling

Advances in integrated circuit and detector technology as well as statistical and nonparametric digital pattern-recognition algorithms have benefitted optical pattern recognition just as they have advanced the sophistication of digital pattern recognition. The diffraction-pattern sampling system to be discussed is the simplest and most hardened hybrid optical/digital system. It is commercially available from Recognition Systems, Inc. The key opto-electronic element in this system is a special Fourier plane detector consisting of thirty-two wedge-shaped and thirty-two ring-shaped detector elements in the two semicircular halves of a one-inch diameter silicon detector [22]. (Many other Fourier plane detectors exist, and digital-computer systems to model this wedge/ring detector (WRD) have been described [23]. We restrict discussion to this FT plane sampling system as representative of such pattern-recognition processors.) The outputs from all sixty-four elements in this WRD are available in parallel and can be multiplexed, electronically preprocessed, and fed to a digital computer for final analysis.

The detector is placed in the FT plane P_2 of the optical system of Fig. 1. The outputs of the ring-shaped detector elements provide the analyst with information on the spatial frequencies present in the input data, on the amount of each spatial frequency present, and thus a measure of the information content of the input data. The outputs of the wedge detector elements provide data on the orientation of the information in the input plane.

When the WRD is used in a pattern-recognition application, the outputs of only selected wedge or ring detector elements are used, thus resulting in a large reduction in data analysis. However, to determine which WRD outputs are to be used and how sums or differences of selected detector outputs are to be weighted, a test set of inputs is used. All WRD outputs are collected for all of these test inputs. Statistical tests are then applied to determine if these data are separable and if recognition algorithms can be developed. Nonparametric pattern-recognition methods are then developed for these data. Once the recognition routine has been determined analysis of future inputs is automatic and rapid.

This type of optical pattern recognition is useful in applications requiring coarse sorting and the analysis of large amounts of data. When such a method is appropriate, a system using WRD data is faster and cheaper than an optical correlator because it requires the analysis of far less data than that contained in the entire input (usually only five or fewer ring measurements are needed in the final system). If all points in the input plane pattern are needed to sort the data, matched spatial filtering or other correlation pattern-recognition methods are required. However, if the resolution of the input data is finer than what is needed and if the input pattern is large and generally uninteresting except for certain smaller key regions, then diffraction pattern sampling using the WRD at P_2 of Fig. 1 is an appropriate pattern-recognition technique.

Many uses of the WRD diffraction pattern-sampling system have been demonstrated [22]. These include: distinguishing urban from nonurban imagery [24] (by the higher spatial frequency data present in urban imagery at higher rings); distinguishing various physiographic regions of an image [25]; and analysis of X-ray images to determine the presence of black lung disease [26]. In this last case, textural image data is used. Sixty-two features of each of six lung zones are measured, feature extraction is achieved by a step-wise discriminant analysis, and a correct classification of over 86 percent of the X-rays examined was achieved using the data from only two to five ring detectors. Detection of muscular dystrophy, the screening of cervical cytologic samples for malignancy, a flow cell analysis system, measurement of linewidths in photomasks, the inspection of griege goods, the determination of the printability of paper and the analysis of handwriting are among other more well-known laboratory and factory applications of this WRD-system [22].

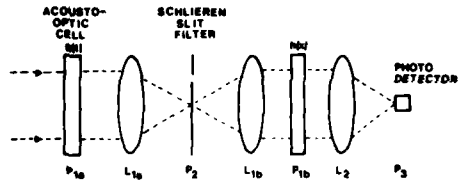

Fig. 3. Schematic of a real-time spatial integrating 1-D optical correlator.

The WRD-system is best suited for more general pattern-analysis applications. The recognition of specific image features generally requires the use of more sophisticated pattern-recognition methods. This is due to the loss of resolution and the phase portion of the FT that occurs when only the diffraction pattern is sampled. Hereafter, we discuss only optical pattern-recognition systems that achieve correlation and matched spatial filtering. These systems are more powerful, but are more complex and less extensively available commercially.

III. Time-Domain Optical Pattern Recognition

Correlation is still the basic optical pattern-recognition operation. In 1-D, we describe the correlation of two time functions or signals by

$$p(\tau) = \int_{-\infty}^{\infty} g(t)\, h(t+\tau)\, dt = g \circledast h \tag{3}$$

where g is the input function, h is the reference function, and τ is the shift parameter. To realize the parallel processing advantages of an optical processor in real time, transducers capable of introducing the input data into the system in real time are needed. The most available and proven real-time optical transducers are acoustooptic cells [27]. In these devices, the input signal is fed to a transducer on the acousto-optic cell and a sound wave proportional to the input signal travels along the cell. Korpel, Minkoff, King, and Lambert *et al.* pioneered much of the research and applications of these devices, especially in radar processing [28]–[31]. These systems usually realize the correlation operation in the time domain and thus we discuss them separately here. These acoustooptic cells are 1-D transducers and thus the resultant correlators are only 1-D and hence are generally restricted to signal pattern-recognition applications. Because of the large center frequencies (up to 1 GHz) and bandwidths (up to 500 MHz) of available acoustooptic cells, such systems are of direct use in radar signal pattern recognition. Many of these concepts originated elsewhere and are reviewed in [32].

The schematic of a spatial integrating 1-D correlator is shown in Fig. 3. The operation of these systems is straightforward. The coded reference signal $h(t)$ is stored at P_{1b} as $1 + h(x_1)$. The real-time received input signal $g(t)$ is applied to

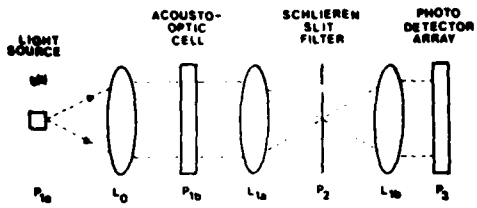

Fig. 4. Schematic of a time integrating real-time 1-D optical correlator.

the transducer at P_{1a}. As this signal moves through the input P_{1a} aperture, it causes a spatial variation in the index of refraction of the cell. This results in a signal in P_{1a} that varies in space (distance x_1 along the cell) and time t. We thus represent this signal as $g(x_1 + v_s t)$, where v_s is the velocity of the sound wave which moves vertically in the x_1 direction in Fig. 3. The wavefront leaving P_{1a} is phase-modulated by $g(x_1 + v_s t)$ and is described by

$$t_1(x_1, t) = a_0 \exp(j\omega t) \exp[jbg(x_1 + v_s t)] \tag{4}$$

where b is a constant and $a_0 \exp(j\omega t)$ describes the plane-wave input of uniform amplitude a_0 traveling in time. The L_{1a} and L_{1b} imaging system and slit filter convert the phase modulation in (4) to amplitude modulation by passing only the first-order term in the transform of (4). The filtered image of t_1 incident on P_{1b} is then

$$t_1'(x_1, t) = jba_0 g(x_1 + v_s t) \exp(j\omega t) \tag{5}$$

and the light distribution transmitted through P_{1b} is $t_1'[1 + h(x_1)]$.

Lens L_2 produces the FT of this product of two filtered signals at P_3, where the FT is evaluated only on-axis by a single photodetector at $u = 0$. L_2 thus effectively integrates $t_1'[1 + h(x_1)]$ over a spatial distance $v_s T$ where T is the time aperture or time window of the input acoustooptic cell. The time history of the output of the photodiode at P_3 is thus (omitting terms with signal functions with no Fourier components with periods of the order of $v_s T$ or larger).

$$u_3(t) = \left| \int_0^{v_s T} g(x + v_s t)\, h(x)\, dx \right|^2$$

or the magnitude squared of the desired correlation of the input and reference signals. Since this correlation is performed in space and displayed in time, the name spatial-integrating correlator is used. With the correlation shift τ between the two functions obtained by the movement of $g(t)$ through the acoustooptic cell, this and similar systems using moving-window transducers are time-domain correlators.

A time-integrating version of this correlator [33] is shown in Fig. 4. This topology is similar to a noncoherent processor described earlier by Bromley [17] and later extended by Goodman [34] for use with a linear input LED array for matrix-vector multiplication applications. In this system, the time-output intensity from an LED is modulated by the input signal $g(t)$ and the input light is now

$$I_1(t) = B_1 + g(t) \tag{7}$$

where B_1 is the input bias level. The reference signal is added to a bias B_2 and used to amplitude modulate the center carrier frequency of an acoustooptic cell. The light distribution incident on the output detector array is now

$$u_3(x, t) = [B_1 + g(t)]\,[B_2 + h(x + v_s t)]. \tag{8}$$

In this topology, integration of the product in (8) is performed on the output detector array and the dc bias terms are removed by ac coupling. Once again the desired correlation of g and h results. In this system, the correlation is performed in time and displayed in space. We thus refer to this as a time-integrating correlator.

Extensions of these 1-D systems to multichannel correlators and the use of heterodyne detection to yield complex correlations are among the many extensions possible in these time-domain pattern-recognition systems [32]. The interaction of bulk laser light and surface acoustic waves represents another viable 1-D optical signal processing approach that promises small size systems of high bandwidth [35].

IV. Frequency-Domain Optical Pattern Recognition

The architecture of the correlators described in Section III was determined by the real-time acoustooptic input transducer used in which the signal moved through the input plane. Although permitting processing of high-bandwidth input data, the space or time bandwidth product of acoustooptic cells is limited to 2000 and the time apertures are typically limited to 10 μs. In addition, these systems are basically 1-D correlators and more conducive for signal rather than image pattern recognition. Optical systems with a fixed rather than moving input data frame and systems that achieve correlation by multiplication in the frequency domain rather than the time domain or space domain are more customarily used in image and 2-D pattern recognition.

The basic equations from linear-system theory that describe such correlators are:

$$\begin{aligned} p(x, y) &= g(\xi, \eta) \circledast h(\xi, \eta) = \text{correlation} \\ &= \iint_{-\infty}^{\infty} g(\xi, \eta)\, h^*(x + \xi, y + \eta)\, d\xi\, d\eta \\ &= \mathcal{F}^{-1}[G(u, v)\, H^*(u, v)] \end{aligned} \tag{9}$$

$$\begin{aligned} r(x, y) &= g(\xi, \eta) * h(\xi, \eta) = \text{convolution} \\ &= \iint_{-\infty}^{\infty} g(\xi, \eta)\, h(x - \xi, y - \eta)\, d\xi\, d\eta \\ &= \mathcal{F}^{-1}[G(u, v)\, H(u, v)]. \end{aligned} \tag{10}$$

We represent the inverse FT by $\mathcal{F}^{-1}$ and the forward FT by $\mathcal{F}$. Optically these two operations are essentially equivalent if the output coordinate axes are properly defined. From the last formulations in (9) and (10), we see that the convolution of two functions can be produced by forming the FT of the product of the FT's of the two functions. When the conjugate transform of the reference function is used (a superscript * denotes complex conjugate), the correlation results. Several 2-D optical correlator architectures are now described and examples of the outputs of such systems are presented.

A. Frequency Plane Correlator

The optical system of Fig. 5 directly implements (9). With $g(x_1, y_1)$ placed at P_1, the light distribution incident on P_2 is $G(u, v)$. With the transmittance of P_2 described by $H^*(u, v)$,

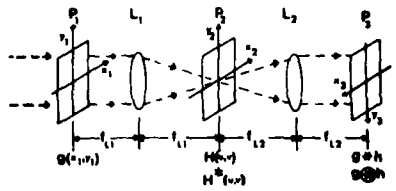

Fig. 5. Schematic of a frequency plane correlator (FPC) with a matched spatial filter (MSF) of the reference function recorded at P_2.

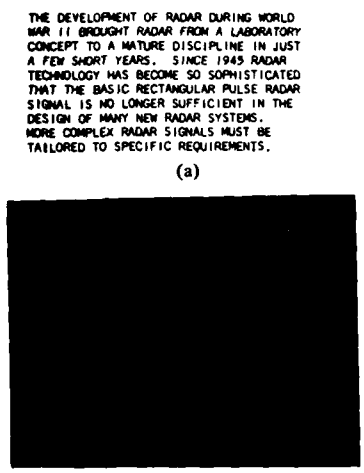

Fig. 6. Representative example of optical pattern recognition using the system of Fig. 5. (a) Input plane P_1 pattern. (b) Output correlation plane P_3 pattern with a matched spatial filter of the word "RADAR" recorded at P_2 of Fig. 5. The location of the correlation peaks correspond to the locations of the word "RADAR" in the input paragraph of text [36].

the light distribution leaving P_2 is $G(u, v)\, H^*(u, v)$. Lens L_2 forms the FT of this product $G(u, v)\, H^*(u, v)$ of two transforms as described by (9). Thus the desired correlation of g and h results at P_3 of Fig. 5. The display of an optical-correlation plane differs significantly from a digital correlation with the coordinates of P_3 being the (x, y) shift parameters of the correlation. The optical-correlation pattern in P_3 consists of peaks of light. The presence of a peak of light in P_3 indicates the presence of h in g, the location of the peak of light denotes the location of h in g, and the amplitude of the peak denotes the degree to which h and the associated region of the input g agree. This coding of the locations and amplitudes of the peaks of light at P_3 in an optical-output correlation plane are best shown by example. In Fig. 6 we show the input plane pattern (a paragraph of text = g) and the resultant output correlation plane pattern (with H^* being the conjugate transform of the word "RADAR"). The reader can convince himself that the locations of the peaks of light in Fig. 6(b) correspond to the locations of the word "RADAR" in the input paragraph of text.

We can describe the example of Fig. 6 mathematically with increased insight into the process that occurs. To achieve such a formulation, we describe the input by

$$g(x, y) = f(x, y) + \sum_{n=1}^{6} h(x - x_n, y - y_n) \tag{11}$$

where h represents the word "RADAR," (x_n, y_n) denote the six locations of this word in the full input g, and f describes the remaining portions of the full input. The transform of (11) incident on P_2 is

$$G(u, v) = F + \sum_{n=1}^{6} H \exp\left[-j2\pi(ux_n + vy_n)\right]. \tag{12}$$

The transmittance of P_2 is H^* and thus the light distribution leaving P_2 is

$$U_2(u, v) = GH^* = FH^* + \sum_{n=1}^{6} HH^* \exp\left[-j2\pi(ux_n + vy_n)\right]. \tag{13}$$

Lens L_2 forms the FT of U_2 and at P_3 we obtain

$$\begin{aligned} u_3(x, y) &= \mathcal{F}[U_2] = \mathcal{F}[GH^*] \\ &= f \circledast h + \sum_{n=1}^{6} h \circledast h * \delta(x - x_n, y - y_n) \\ &= \sum_{n=1}^{6} \delta(x - x_n, y - y_n). \end{aligned} \tag{14}$$

In the last expression in (14), the autocorrelation $h \circledast h$ of h was assumed to be a delta function of normalized unit amplitude (i.e. $h \circledast h = 1$) and the key object and the other regions of the input are assumed to be uncorrelated (i.e., $f \circledast h = 0$). The resultant correlation of g and h thus reduces to six delta functions at locations (x_n, y_n) corresponding to the six locations of h in g.

The correlator of Fig. 5 is the classic matched spatial filter (MSF) system devised by Vander Lugt [7] in 1964. The H^* pattern recorded at P_2 is an MSF. We refer to this as a frequency plane correlator (FPC) since the desired correlation is achieved by multiplying the FT's of g and h. One of Vander Lugt's major contributions was the description of how a filter function with complex transmittance H^* could be recorded on an intensity-sensitive medium at P_2. The scheme used is similar to the holographic-synthesis procedure originated by Gabor [37], and developed by Leith and Upatnieks [9] for 3-D imaging applications.

B. Matched Spatial Filter

The MSF synthesis procedure as described by Vander Lugt assumed g to be the signal-plus-noise and the application directly envisioned was the recovery of a signal h buried in noise. In our pattern-recognition application, those portions of the input that do not agree with the signal or reference function h are effectively the noise or the function f in (11). To record H^* at P_2, the function h is placed at P_1 and the interference of its transform H (formed by L_1 at P_2) and a plane wave reference beam $U_R = \exp(j2\pi\alpha x_2)$ of unit amplitude is recorded at P_2, where $\alpha = (\sin\theta)/\lambda$ is the spatial frequency due to the off-axis angle θ between the reference and signal beams. The pattern recorded at P_2 and the subsequent transmittance of P_2 is

$$\begin{aligned} t_2(x_2, y_2) = |H + U_R|^2 &= 1 + |H|^2 \\ &+ H \exp(j2\pi\alpha x_2) + H^* \exp(-j2\pi\alpha x_2). \end{aligned} \tag{15}$$

The last term in (15) is proportional to the desired transmittance H^* of P_2. To see how the effects of this term are separated from the other three terms in (15), we consider the correlation process itself in detail.

During correlation, g is placed at P_1 and the full transmittance of P_2 is t_2 given by (15). The light distribution leaving P_2 is Gt_2 and L_2 of focal length f_{L2} forms the FT of this product at P_3, where we find

$$\begin{aligned} u_3(x_3, y_3) = \mathcal{F}[Gt_2] &= g \text{ at } x_3 = y_3 = 0 \\ &+ h \circledast h * g \text{ at } x_3 = y_3 = 0 \\ &+ g * h \text{ at } x_3 = \alpha\lambda f_{L2}, y_3 = 0 \\ &+ g \circledast h \text{ at } x_3 = -\alpha\lambda f_{L2}, y_3 = 0. \end{aligned} \tag{16}$$

From (16), we see that the desired correlation $g \circledast h$ can be separated from the other three terms in the output plane pattern by proper choice of the reference to signal-beam angle θ. The region of the correlation plane shown in Fig. 6 is the portion centered at $x_3 = -\alpha\lambda f_{L2}, y_3 = 0$.

The FPC optical pattern-recognition system of Fig. 5 is useful when a single fixed reference function is to be located. In many applications (i.e., character recognition), multiple and composite MSF's are useful to allow a parallel pattern-recognition search to be performed. Several multiple MSF approaches are summarized in [38]. Much of the work in this area relates to optical data storage [39]. Optical pattern-recognition techniques have been applied to a multitude of applications including diatom (water pollution particle) [40], text [41], aerial imagery [42], and key-object [43] recognition. Single, multiple, and averaged MSF's have been used in [40] and [43] to reduce the number of required filters and to enchance the capacity of the recognition system.

C. Joint Transform Correlator

An alternate optical pattern-recognition topology [44] is shown in Fig. 7. In this architecture, the two functions to be correlated (g and h, assumed to be of spatial extent b) are placed side by side at P_1 with a center-to-center separation $2b$. The transmittance of P_1 (in 1-D, for simplicity only) is

$$u(x_1) = g(x_1 - b) + h(x_1 + b). \tag{17}$$

Lens L_1 forms the FT of (17) or a joint transform pattern that is recorded at P_2. The subsequent transmittance of P_2 is

$$\begin{aligned} t_2(u) &= |G \exp(-j2\pi ub) + H \exp(+j2\pi ub)|^2 \\ &= |G|^2 + |H|^2 + GH^* \exp(-j4\pi ub) + G^*H \exp(+j4\pi ub). \end{aligned} \tag{18}$$

P_2 is now illuminated with a plane wave of read-light (shown incident on P_2 in reflection in Fig. 7).

With P_2 in the front focal plane of L_2, the pattern at P_3 is the FT of (18) or

$$\begin{aligned} u_3(x_3) = g \circledast g &\text{ at } x_3 = 0 \\ + h \circledast h &\text{ at } x_3 = 0 \\ + g \circledast h &\text{ at } x_3 = +2b \\ + h \circledast g &\text{ at } x_3 = -2b. \end{aligned} \tag{19}$$

Proper choice of the separation $2b$ between the inputs in Fig. 7 enables the desired $g \circledast h$ term in the output pattern of (19) to be separated from the other terms. This is similar to how the choice of θ in the FPC system of Fig. 5 enabled the desired correlation term to be separated from other terms in that output plane. This is referred to as a joint transform correlator (JTC) [44].

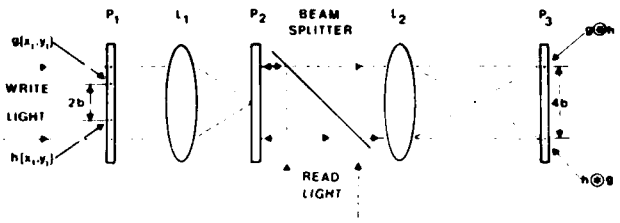

Fig. 7. Schematic of a joint transform correlator (JTC) for optical pattern recognition.

D. Real-Time Optical Pattern Recognition

Since the advantages of optical pattern recognition include real-time and parallel processing, reusable and real-time 2-D electrooptical transducers are necessary at the input plane P_1, and often at the transform plane P_2 in the systems of Figs. 5 and 7, if real-time operation is to be realized. The devices used for these purposes are known as spatial light modulators (SLM) [45], [46]. The architecture of the optical pattern-recognition system of Fig. 7 assumed an optically addressed and reflex-mode readout SLM at P_2 with different write and read wavelengths. Most optically sensitive SLM's operate in this manner.

The example shown in Fig. 6 was performed in real-time on the FPC system of Fig. 5 using an electron-beam addressed electrooptic crystal input plane P_1 transducer. The input paragraph of text was scanned onto a special target crystal by a current-modulated electron gun, quite similar to the operation of a television. A collimated laser beam was then passed through this crystal and emerged spatially modulated with the input data. The electrooptic effect [47] is used in this and similar devices to modulate an input light wave proportional to the spatially varying voltage or charge pattern across the crystalline material [45], [46].

Another real-time optical pattern-recognition application nearing completion at General Motors [48] is shown in Fig. 8. The application involved the recognition and location of the position of a 3-D object (a relay for the example shown in Fig. 8) on an assembly line. The output of this optical pattern-recognition system is to be interfaced to a robot as part of an automated assembly line. In operation, a diffusely illuminated image of the assembly line is continuously focused onto the photoconductor side of an SLM at P_1 of Fig. 5. The image on the liquid-crystal input transducer used is read out continuously in reflection in coherent laser light. Since the decay time of the liquid-crystal SLM is only 20 ms, the liquid-crystal input transducer serves as a noncoherent-to-coherent input P_1 image converter for the FPC system of Fig. 5. Several images of the input object (a relay) on the assembly line are shown in Fig. 8(b). An MSF of the key object to be searched for (the relay) is stored on film at P_2 of Fig. 5. The peak in the output correlation plane P_3 pattern and its cross sectional scan are shown in Fig. 8(a) for several locations of the input relay on the moving assembly line in real time.

To change the key object to be searched for, only the film at P_2 need be changed. A modified scan and prism system is presently under consideration at General Motors to enable recognition of a key object to be maintained in the presence of expected rotational and scale differences between the input and reference (or MSF) imagery. In Sections V and VI, we consider alternate methods by which such distortion invariance and increased optical pattern-recognition flexibility can be realized.

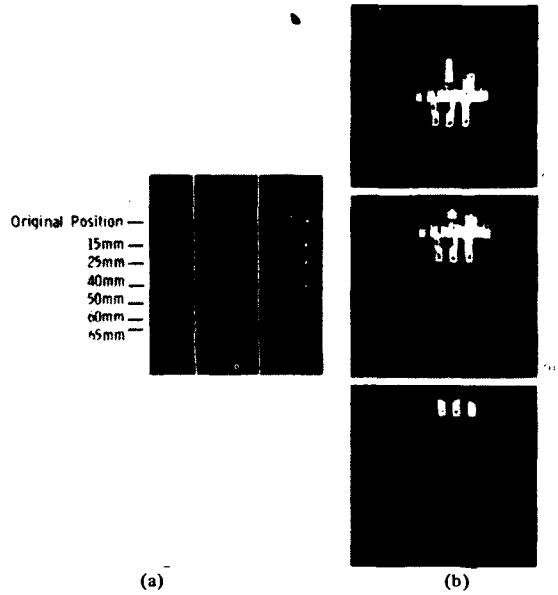

Fig. 8. (a) Example of a real-time optical pattern recognition [48]. (b) Output correlation peak and its cross sectional scan for various locations of the input object (a relay) in the input field of view.

An alternate real-time 2-*D* optical pattern-recognition system [49] intended for signal-processing applications, specifically the generation of the ambiguity function (range versus Doppler) for any coded input waveform, is shown in block diagram form in Fig. 9. This topology combines the high bandwidth features of the acoustooptic correlators described in Section III with the 2-*D* nature of an optical processor. In signal correlations, coded waveforms are generally employed and the target's range and Doppler vary. The desired target data (its range and Doppler) is best conveyed by an ambiguity surface [50] with range τ and Doppler v axes. This output can be realized in a multichannel correlator in which different Doppler shifted versions of the reference signal are recorded on different lines. Each of these signals is then correlated with the received signal in 1-*D*. The resultant 2-*D* plot (correlation or range τ horizontal and Doppler vertical) is an ambiguity function, widely used in radar. This basic signal pattern-recognition problem thus deserves note in this paper. Many methods exist by which this operation can be realized. One of the more promising and developed ones is shown schematically in Fig. 9 and is described below.

In the pulse compression section (Fig. 9(a)), the coded radar waveform to be used is generated by computer or other methods and displayed on a CRT from which it is continuously imaged onto a liquid crystal. The received input radar signal is fed to an acoustooptic input transducer. This received input signal is continuously imaged onto the reference signal (on the liquid crystal) in reflection, the product integrated and heterodyne detected by a photodiode, whose time-history output is the correlation of the transmitted coded radar signal and the reflected signal received from various targets for various transmitted pulses in the pulse burst. If this process is continued for N pulses in a pulse burst waveform, N output correlations appear in time from the photodiode. These outputs are separated in time by one pulse period and correspond to the returns from targets at a specific range, with each of the N-returns modulated by the target's Doppler. If these

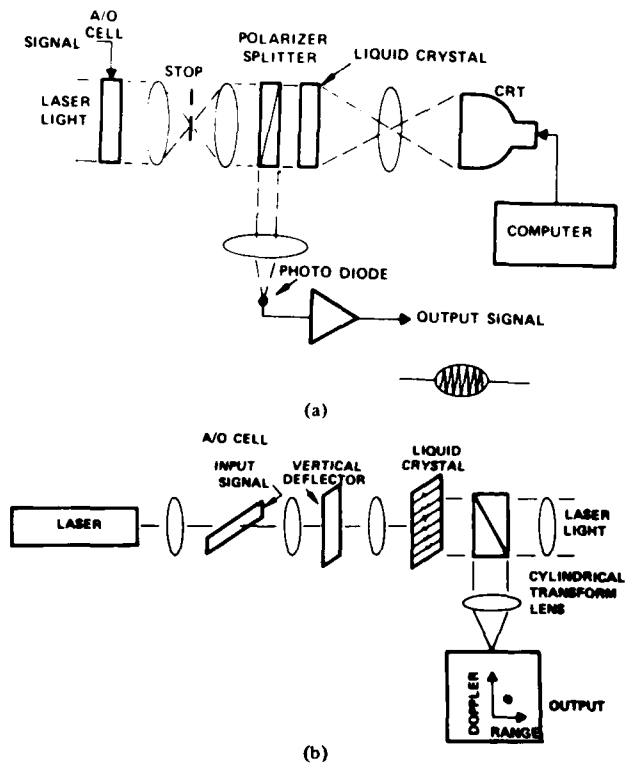

Fig. 9. Schematic of a 2-*D* real-time optical signal processor. (a) Pulse compression section. (b) Doppler processing section [49].

correlations, corresponding to the returns due to sequential transmitted pulses, are recorded on separate horizontal lines, they will align vertically for a target at a given range.

To obtain Doppler data on the target, one must integrate across these N correlations. To achieve this, the output from the photodetector is fed to a second acoustooptic cell (Fig. 9(b). A laser is pulsed on in synchronization with the PRF of the code and passed through a 1-*D* deflector. In the resultant pattern recorded on the second liquid crystal, each of the N correlations from the pulse compression section are recorded on N separate lines. The vertical scanning system for this 2-*D* pattern is synchronized to the PRF of the transmitted waveform. This second liquid crystal is then read from the right side and the 1-*D* vertical FT of the pattern on this liquid crystal yields the desired range/Doppler ambiguity function. This system is scheduled for completion and delivery in late 1978.

V. Weighted MSF Synthesis

As implied in Section IV, practical pattern-recognition systems of any kind must be able to operate even with various distortions (scale, rotation, aspect, etc.) present between the input and reference functions. Such flexibility is achieved in digital pattern recognition by sophisticated software algorithms. Recent programs intended to increase the flexibility of optical pattern-recognition systems are addressing such practical problems with encouraging results. One approach toward this goal involves control of the MSF synthesis process [42]. To describe this method, we rewrite (15) as

$$t_2(x_2, y_2) = 1 + 1/K + (2/\sqrt{K}) \cos \psi \qquad (20)$$

where $K = A^2/|H|^2$ is the ratio of the intensities of the refer-

ence and signal beams and where $\psi = 2\pi\alpha x_2 + \text{Arg}\ (H)$ describes the recorded MSF as a fringe pattern at spatial frequency α with the phase of H encoded as a phase modulation on this carrier frequency α.

At this point, it is necessary to discuss one feature of all MSF optical pattern-recognition systems. We refer to the limited dynamic range of the P_2 recording material. The optical FT of an image contains a large dc term (that contains no information useful in distinguishing objects) and higher frequency components of far lower intensity (that contain the data needed to distinguish or discriminate one object from another similar one). The bias on the MSF material is properly adjusted so that this dc term saturates the MSF material, whereas high modulation is given to the lower intensity and higher spatial frequency data. Thus in practice, an optical FPC system correlates the ac rather than the dc portions of imagery.

Referring to (20), we see that since H varies spatially (with x_2 and u) so does K and hence, so does the modulation of the fringe pattern. Recently [42] use has been made of this fact to choose the spatial frequency f^* at which $K = 1$ (corresponding to full modulation). This effectively weights specific spatial frequencies in the MSF. The use of this adjunct to optical pattern recognition is best shown by example. The image of Fig. 10(a), characterized by regions A, B, and C that are respectively predominantly rural, urban and structured was used as the test image. An MSF of the full image was made with $K = 2$ at various spatial frequencies f^* and correlated with the three indicated isolated regions of Fig. 10(a). In Fig. 10(b) we show the variation of the peak intensity I_p of these correlations with the f^* band in which $K = 1$ during MSF synthesis. The correlation for the urban input (curve B) clearly peaks at a larger f^* setting than for the rural input (curve A), with the correlation for the structured image region (curve C) peaking at an intermediate f^* setting. From this example, we clearly see that control of K and f^* can greatly effect the resultant correlation. The WRD detector (Section II-A) was used to facilitate rapid evaluation of the effects of f^* and K settings on the output correlation [42].

This same technique, which we refer to as weighted MSF synthesis, is also useful in controlling the effect of various expected image-degradations on I_p and signal-to-noise ratio (SNR) of the output correlation [42]. Many different expected degradations can occur between the input and reference image. In Fig. 10(c) we consider rotational misalignments between the key object as it appears in the input and reference scenes and the effect that selection of the proper f^* band can have on the SNR of the output correlation. As shown, setting $K = 1$ at a large f^* (band H) results in a larger SNR than lower f^* choices. However, as the angle θ of rotational misalignment between the input and reference image increases, the SNR of the correlation with the MSF formed with $K = 2$ in band H rapidly decreases. Conversely, a lower f^* choice (band B) results in a lower initial SNR, but a far lower SNR loss with θ variations.

Thus when image degradations are present, lower f^* settings are preferable. The reason is simply that when emphasizing high-input spatial frequencies (by high f^* settings), these are the first components lost when degradations occur between the input and reference imagery. By emphasizing lower input spatial frequency components (by lower f^* settings) and sacrificing some initial SNR and I_p (Fig. 10(c)), we find the resultant correlation preferable when differences or degradations are expected between the input and reference images.

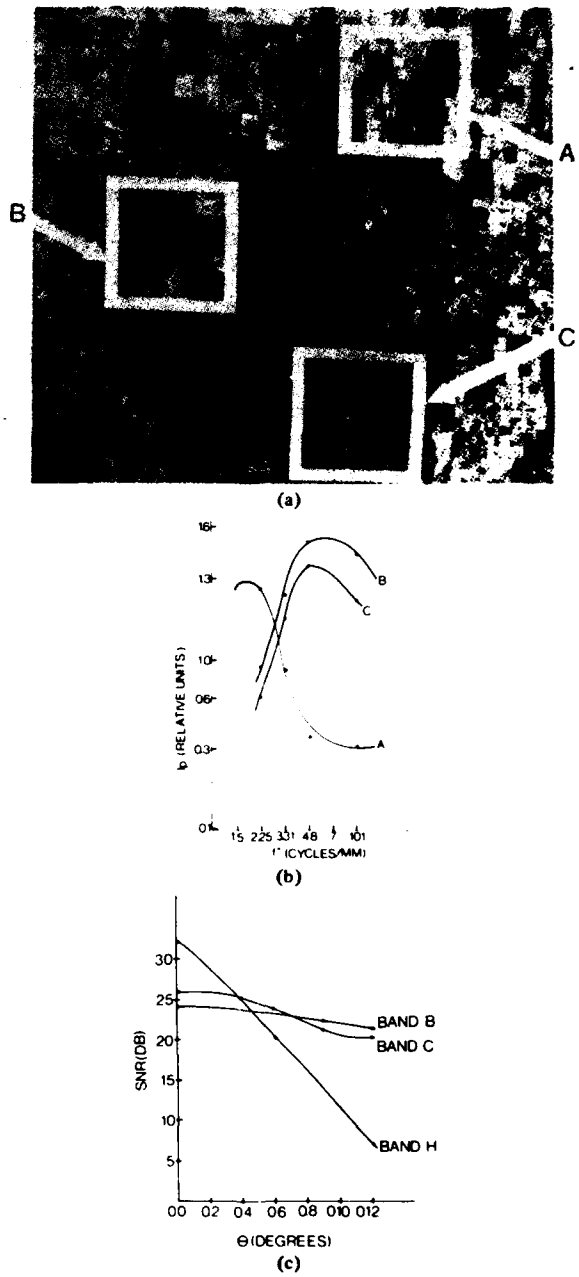

Fig. 10. Optical pattern recognition by weighted MSF control [42]. (a) Input scene. (b) I_p versus f^* for input regions A, B, C. (c) SNR versus θ for various f^* bands.

Many types of image differences have been examined [51] such as scenes of the same area taken years apart, in different seasons, from different aspect angles, and radar images taken from different headings or from different sensors, etc. The magnitude of the I_p and SNR correlation loss for each of these degradation sources were found. For the imagery analyzed, textural-image differences (snow cover in winter scenes and new structure in imagery taken years apart) were found to have less of a degrading effect on the correlation than geometrical image distortions (due to heading or aspect differences). Weighted MSF synthesis control was found to be helpful in reducing the correlation loss due to geometrical-image differences if the spectrum of the imagery was broad

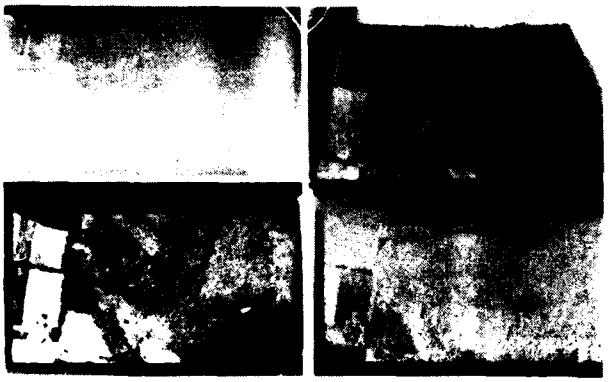

Fig. 11. Multisensor imagery exhibiting intensity disparity [55].

and if the image degradation could be classified by a narrow-band distortion function. Aspect differences satisfy these criteria, whereas slant range error and radar shadow effects in the SLAR imagery examined (opposite headings and low depression angles) were of such a broad-band nature that extensive compensation for correlation loss was not possible.

Another expected source of image differences arises when images taken from different sensors are correlated [52]. In a missile guidance application, the stored reference image is usually assumed to be a high-quality aerial image and the input image a real-time radar map. In such cases, intensity differences occur in various image regions between the two scenes. The intensity of a given object depends on the nature of the object, the illuminating wavelength, and so many other factors that one cannot predict in advance how a given scene will appear in a radar image without *a priori* knowledge of the content of the various regions of the scene. We refer to this aspect of multisensor image processing as intensity disparity image pattern recognition. Similar intensity differences arise between imagery taken from the same sensor at different times.

One of the classic approaches to intensity disparity is to differentiate both images [53]. The premise here is that only the edges of the regions in such scenes are the features that are common between such imagery. However, this is a purely statistical contribution to the correlation. This contribution decreases as we increase the number N of uniquely shaped regions in the image with random intensity variations. There are also various types of image differentiation [54]. If we consider an MSF in which K is set to 1 (optimum modulation) at a high spatial frequency f^* (thus emphasizing the high spatial frequency portion of the input image), we are effectively performing one type of image differentiation. A plot of the transmittance of such an MSF shows that it represents a high-pass filtered transfer function with a 6-dB cutoff at the f^* spatial frequency at which K was set to unity during MSF synthesis.

Thus, in performing the correlation $g \circledast h$ using an MSF, the reference scene h can be modified to be a high-pass filtered version h' by the action of the MSF (and so is g). The correlation $g' \circledast h'$ of the input and a high-pass filtered reference function is thus performed. By varying f^*, we can control the degree of image differentiation used and arrive at the optimum combination of statistical and deterministic (edge-enhanced) pattern recognition. An example of one set of multisensor imagery is shown in Fig. 11. The left portion of the image exhibits several fields of various degrees of random intensity variations and of somewhat unique shapes. This portion of the image can be viewed as a set of N key objects (where N is somewhat small), whereas the remaining portion of the image contains little information content. By the proper choice of the spatial frequency f^*, we have successfully correlated all four images in this and similar image sets using only one MSF formed from one of the images. Similar multispectral correlations on various other image sets (including a completely contrast-reversed image pair) have been achieved by this method [55].

VI. Space-Variant Pattern Recognition

As noted in Sections IV and V, geometrical differences between the input and reference imagery severely degrade correlations. Scale and rotation are the most common geometrical differences. These can be accommodated by use of multiple MSF's at P_2 of Fig. 5. However, this approach requires that multiple output correlation planes be scanned and always results in a considerably reduced output light intensity. In another approach to producing a scale-invariant optical correlator, the input plane P_1 in Fig. 5 is placed behind L_1. A scaling correlator results in which a scale search of the input function can be performed by varying the distance from P_1 to P_2. Rotational differences in the orientation of the MSF can also be accommodated by rotating P_1 or P_2. In both of these latter schemes, the time required to manually search scale and rotational differences is not compatible with the real-time processing advantages of an optical pattern-recognition system. In this section, we consider a real-time optical processing approach to the problem of geometrical differences in pattern recognition. The resultant optical processor will be a space variant rather than a space-invariant system.

One of the major limitations in the realization of a practical recognition system has been the space invariance of an optical processor. This feature allows these systems to be described by the convolution integral in (10). With reference to Fig. 5, the input function is g, the system's impulse response is h (the transform of the system's transfer function H recorded at P_2), and the content of the output plane P_3 pattern is the convolution of g and h. Considerable research, presently in progress, is concerned with producing various types of space-variant optical systems (whose impulse response varies spatially with input position). One program in this area directly related to pattern recognition involves the use of coordinate transformation preprocessing [56] as initially described by Huang [57] and Sawchuck [58]. We describe two examples of such optical systems in detail below.

We consider first a space-variant optical pattern-recognition system whose output correlation is invariant to scale differences between the input and reference functions. By applying a logarithmic transformation to the input and reference functions, we obtain (in 1-D for simplicity) $g' = g(\exp x)$ and $h' = h(\exp x)$. The FT of these functions yields G' and H' (or H'^*). It has been shown [56] that the FT of g' is the Mellin transform [59] of g. Of particular interest is the case when $h(x) = g(ax)$ (i.e., g and h differ by a scale factor a). In this case the Mellin transforms M_g and M_h of g and h are related by

$$M_g(u) = M_h(u) \exp(-j2\pi u \ln a) \exp(-j2\pi\alpha x_2). \quad (21)$$

This follows from the definitions of M_g and M_h as the FT's of g' and h'. The final exponential factor in (21) is due to the spatial carrier α on which M_h is recorded (as in the MSF synthesis and correlation operation described in Section IV).

When realized using the FPC system of Fig. 5, g' is placed at P_1 and M_h^* is recorded at P_2 of Fig. 5. The light incident on P_2 is M_g (the FT of g') and the light distribution leaving P_2 is $M_g M_h^*$. Lens L_2 in Fig. 5 forms the FT of $M_g M_h^*$ at P_3 where we find

$$u_3 = \mathfrak{F}[M_g M_h^*] = \mathfrak{F}[M_h M_h \exp[-j2\pi(u \ln a + \alpha x_2)]$$
$$= h \circledast h * \delta(x_3 - \ln a\, \alpha\lambda f_L). \tag{22}$$

From (22), we see that the resultant correlation is displaced from its normal location $x_3 = \alpha\lambda f_L$ by an amount proportional to the natural logarithm of the unknown scale factor "a" between the two functions. Thus from the location of the correlation peak we can determine "a." Of more importance is the fact that the output correlation is identical to the autocorrelation $h \circledast h$, just as if $g \equiv h$ with no scale difference present.

We now consider a space-variant optical pattern-recognition system that is invariant to rotational differences between the input and reference images. The same coordinate preprocessing approach is again used. The two functions are h and g (a rotated version of h with rotational angle θ_0). We first convert both $h(x, y)$ and $g(x, y)$ to new functions $h'(\xi, \eta)$ and $g'(\xi, \eta)$ by the coordinate transformations $\xi = \tan^{-1}(y/x)$ and $\eta = \sqrt{x^2 + y^2}$ (i.e., a polar transform). This transformation now converts a rotation by θ_0 into a shift. The 1-D conjugate transform H'^* of the coordinate transformed undistorted function h' is formed and stored at P_2 of Fig. 5.

With g' recorded at P_1 of Fig. 5, the light distribution leaving P_2 is $G'H'^*$. To best understand how the rotational invariance is achieved, we separate the original function g into two parts g_1 and g_2 (where in polar-coordinates, g' occupies the 0 to $-\theta_0$ portion of θ space and g_2' occupies the remaining 0 to $2\pi - \theta_0$ region). The portions G_1' and G_2' of the FT's of the coordinate-transformed polar functions $g'(\xi, \eta) = g'(\theta, r)$ are related to the FT's G_1 and G_2 of the corresponding portions g_1 and g_2 of the original $g(x, y)$ image by

$$G' = G_1' + G_2' = G_1 \exp(-j\omega_\theta \theta_0) + G_2 \exp[-j\omega_\theta(2\pi - \theta_0)] \tag{23}$$

where ω_θ denotes the Fourier plane spatial frequency variable associated with the polar-angle variable $\theta = \xi$.

The light leaving P_2 is now $G'H'^*$ and its FT formed at P_3 of Fig. 5 by L_2 is

$$u_3 = \mathfrak{F}[G'H'^*] = g_1' \circledast h + g_2' \circledast h$$
$$= h_1 \circledast h * \delta(\theta - \theta_0) + h_2 \circledast h$$
$$* \delta(\theta + 2\pi - \theta_0). \tag{24}$$

From (24), we see that the output correlation is now divided into two correlation peaks separated in distance by 2π in P_3 space. The sum of these two correlation peaks is

$$u_3 = h_1 \circledast h + h_2 \circledast h = h \circledast h \tag{25}$$

or the output correlation of two rotated functions equals the autocorrelation of the original unrotated functions. There is thus no correlation loss even if the input and reference functions are rotated versions of one another with an unknown rotational angle θ_0. From (24) we see that the location of the output correlation peak is proportional to the unknown rotational angle θ_0 and thus θ_0 can also be found from the output correlation.

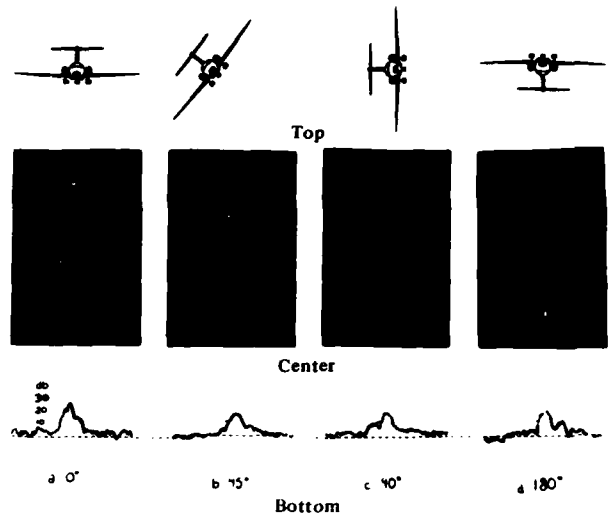

Fig. 12. Rotation-invariant optical pattern recognition. (Top) input. (Center) output correlation plane. (Bottom) cross-sectional scan of the correlation peak.

An example of this rotation invariance is shown in Fig. 12. The reference image chosen was an airplane, an MSF of the polar transformed version of the airplane was recorded at P_2 of Fig. 5. As the input was rotated (Fig. 12, top), its polar transform was formed and recorded at P_1. The resultant output correlation plane pattern (Fig. 12, center) and its cross sectional scan (Fig. 12, bottom) show the predicted results. The location of the output correlation peak changes proportional to the rotational misorientation between the input and reference and the output correlation peak remains essentially invariant to the input rotational differences.

The log coordinate transformation required in the Mellin transform correlator can easily be realized by use of log modules in the deflection system of the input plane SLM. The polar transforms in Fig. 12 were realized in real time using a specially modified camera. Extensions of these optical space-variant pattern-recognition methods and the formulation of a system invariant to multiple distortions are described in detail elsewhere [60].

VII. Hybrid Optical/Digital Correlators

The final embodiment of any optical processor will be a hybrid system [36] in which the best features of optical and digital processing are properly married. The architecture of one such hybrid system that has been assembled [61] is shown in Fig. 13. The upper portion of this schematic shows the FPC system of Fig. 5 with real-time SLM's at the input and filter planes. Digital control of the content of these SLM's and control of the system's WRITE, READ, and ERASE cycle are implied in the flowlines shown. The digital preprocessor in Fig. 13 is used for format control and as a scan converter. As shown, the outputs at the FT and correlation planes are detected by a 2-D array and analyzed by a microprocessor array (250-ns cycle time, Intel 3000 series) to extract the desired information (usually the location of the correlation peak). A buffer memory within the interface allows interframe operations to be performed such as change detection and output time history of correlation peaks to be found.

The microprocessor-interface system allows us to digitize the output correlation plane to a variable resolution. This is an

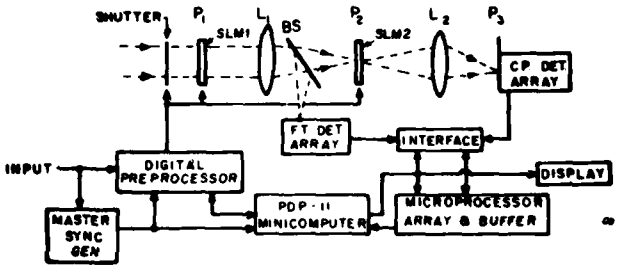

Fig. 13. Schematic diagram of a microprocessor-based hybrid optical/digital pattern-recognition system [61].

important feature as it allows us to reduce the quantity of output data to be analyzed, as the application warrants. Simple thresholding of the output plane to any of 256 gray levels is possible. However, such a simple detection scheme is rarely adequate. Thus an integrator, peak detector, and counter were added to the output-detection system to allow use of alternate-detection criteria such as the area under the correlation peak or whether the output signal exceeds a given threshold level for a given amount of time. We have shown earlier [42] that the area of the correlation peak decreases less rapidly than I_p with rotation, scale, or other distortion parameters. Thus use of such alternate detection methods is another way by which the pattern-recognition system's sensitivity to differences between the input and reference imagery can be reduced.

An alternate version of a hybrid-correlator can be realized by placing a TV or linear CCD/photodiode detector in the frequency plane P_2 of the JTC system of Fig. 7. Lens L_2 and plane P_3 in Fig. 7 are not used now, rather the transform of the data at P_2 previously performed by L_2 is now realized by a digital fast Fourier transform (FFT) or spectrum-analyzer system [62]–[64].

To accomplish the processing previously performed by L_2 in Fig. 7 on the joint-transform pattern of (17), the pattern in (18) is detected and scanned as a time or video signal $v(t)$. An FT operation on $v(t)$ is realized by multiplying $v(t)$ by quadrature sinusoids ($\sin \omega_0 t$ and $\cos \omega_0 t$); the two separate products are then integrated over one line scan time of the output detector, squared, and summed. From (18), we see that the $|G|^2 + |H|^2$ envelope is the slowly varying part of the output video signal, whereas the important part of $v(t)$ is the cosine function.

If the input and reference patterns are equal, $g = h$ and (18) becomes

$$v(t) = 2|H|^2(1 + \cos 4\pi bu). \tag{26}$$

For this case the frequency of the cosine depends upon the separation between the input and reference in P_1 or, therefore, the location of h in g. If g is displaced from h by $2.5b$ rather than $2b$, then (26) becomes

$$v(t) = 2|H|^2[1 + \cos(4\pi bu + \pi bu)] \tag{27}$$

from which we see that the location of h in g can be found from the frequency of the cosine pattern.

To demonstrate this principle, a landing field was chosen as the key reference object h to be located (Fig. 14(a), left) in a larger input scene (Fig. 14(a), right). Several of the input image pairs at P_1 of the JTC system are shown in Fig. 14(a), with the separation between h and g in the two images increasing. The joint transform of each input image pair was detected, scanned, and quadrature modulated as noted earlier. As the frequency of the local oscillator was swept with time, the output was displayed (Fig. 14(b)). The horizontal axis in Fig. 14(b) thus corresponds to different mixing oscillator frequencies or equivalently to testing different displacements or shifts of the input function. As shown, the location of

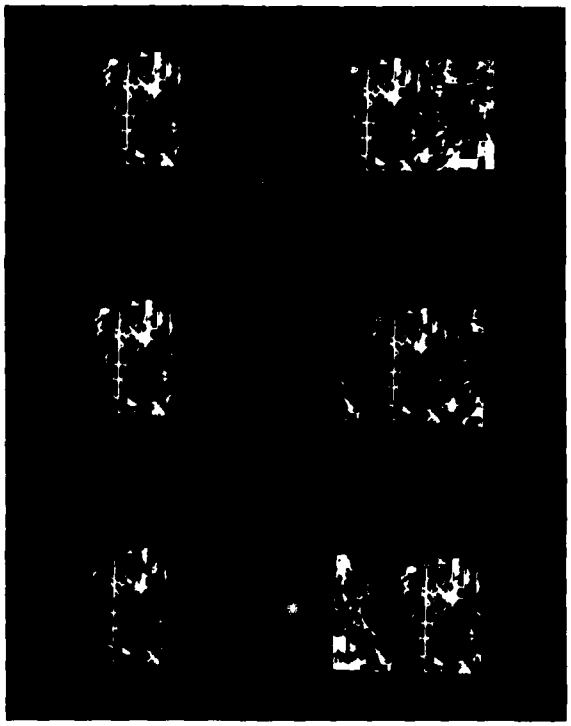

(a)

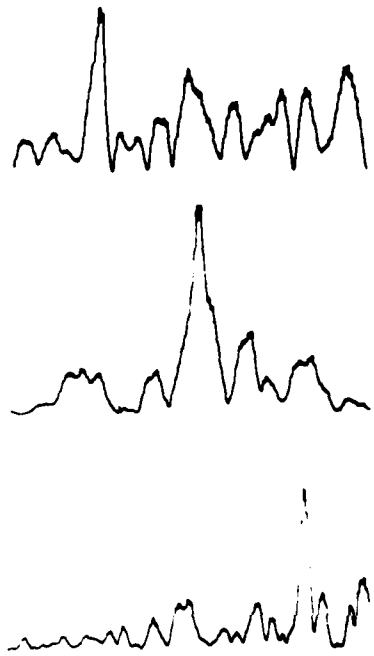

(b)

Fig. 14. Experimental demonstration of a hybrid optical coherence measure pattern-recognition system [64]. (a) Inputs. (b) Cross-sectional scan of the output correlation.

the peak output from the electronically processed joint-transform pattern shifts right as the location of h in g shifts right. The presence of a peak indicates the presence of h in g and the location of the peak indicates the location of h in g.

Returning to (26) and (27), we see that the amplitude of the recorded cosine pattern depends on the product of the magnitudes of the FT's of the two input functions. If g and h are identical except for their strength, i.e., $g(x) = ah(x)$ in 1-D, the detected pattern is

$$t_2 = |H|^2(1 + a + 2a \cos 4\pi bu). \tag{28}$$

From (28), we find that the modulation is reduced proportional to the reduced signal strength of g. Since the amplitude $2a$ of the cosine term can easily be found from the electronically processed output, the vertical scale in the output pattern (Fig. 14(b)) can appropriately be adjusted and thus a normalized correlation produced.

Another feature of electronic postprocessing and further insight into the operation of the original JTC-system can be seen by considering the case when $h \neq g$. The fringe pattern at P_2 is now no longer a pure cosine but is phase modulated (spatially) by the difference between the phases of the transforms G and H. The power spectral density at the carrier frequency $2b$ is now decreased proportional to the degree of mismatch of g and h. Thus from the magnitude of the output-spectral density, we have a measure of the spectral purity of the video signal and equivalently the coherence or similarity of the two inputs. The carrier period variance and carrier phase variance can easily be found (e.g., from a phase-locked loop on the output) and hence a "coherence measure correlator" results.

However, electronic postprocessing also allows increased flexibility since the signals can be modified prior to quadrature modulating and processing them. This luxury and flexibility is not present in the full optical system of Fig. 7, since L_2 must take the FT of the P_2 pattern (the joint transform of G and H) and once detected P_2 cannot easily be modified. In practice g and h will differ as noted in Sections IV and V. For the case when the distortion present in g can be described by the action of a linear-space invariant system with impulse response f, we can describe g by $g = h * f$. In many instances the distortion f is known or reasonable distortion functions can be assumed *a priori*. In such cases, the electronic postprocessor of the P_2 data can be modified (for example, by phase-modulating the local oscillator in the detection system with the transfer function F of the assumed distortion function f). An "equalizing correlator" (a term borrowed from communications) then results in which various distortions present in g that are not in h can be removed (or their effects equalized). Experimental confirmation of the "equalizing optical correlator" has also been reported [64].

An alternate technique by which improved discrimination can be achieved in optical pattern recognition was suggested by Caulfield and Maloney [65]. In this approach, linear combinations of the system's responses to various input characters are formed in a second processing stage.

Electronic preprocessing and postprocessing techniques have recently been used to enable bipolar correlations to be performed on incoherent processors [66]–[69]. The use of computer-generated holograms to synthesize spatial filters [70], [71] of functions not easily physically realizable represents yet another use of digital techniques in optical pattern recognition.

VII. Summary

Although many survey articles, special issues, and books exist on optical computing, this article is the first to address only the issue of optical pattern recognition–thus allowing a unified treatment in some depth. When we think of optical pattern recognition, we usually consider only the optically matched spatial-filtering system of 1964. However as shown, many advances have occurred since 1964. A wealth of new architectures for optical pattern-recognition systems exist and have been demonstrated and many refinements have occurred in the original Vander Lugt correlator.

Research in optical pattern recognition is now addressing more practical and real pattern-recognition problems. These directed research efforts and major advances in optoelectronic and solid state components, plus advances in digital electronics and digital pattern-recognition algorithms have affected optical pattern-recognition systems. A rapidly increasing repertoire of new operations (such as space-variant ones) are now possible in optical processors. Many of these have already been applied to pattern-recognition applications.

Many other optical processing operations not discussed in this survey exist that do not use the classic FT property of a lens. These include an optical system to realize the discrete FFT [72], optical systems operating in residue arithmetic [73]–[75] and many others [11]. In time, these and other optical processing methods will be applied to pattern-recognition applications. This will further increase the capability of optical pattern-recognition systems, while retaining the high-speed parallel processing, and large-space-bandwidth product features of optical processors that have made them attractive for the past twenty years.

Acknowledgment

The author thanks his present and past Ph.D. students who performed most of the experiments whose results are included, especially Dr. Warren Sterling, Dr. Demetri Psaltis, and Dr. Alan Furman.

References

[1] E. Abbe, "Beitrage zur theorie des mikroskops und der mikroskopischen Wahrnehmung," *Arch. Mikroskop. Anat.*, vol. 9, pp. 413–468, 1873.
[2] A. B. Porter, "On the diffraction theory of microscope vision," *Phil. Mag.*, vol. 11, p. 154, 1906.
[3] F. Zernike, "Das Phasenkontrastverfahren bei der mikroskopischen beobachtung," *Z. Tech. Phys.*, vol. 16, p. 454, 1935.
[4] A. Marechal and P. Croce, "Un filtre de frequences spatiales pour l'amelioration du contrast des images optiques," *C. R. Acad. Sci.*, vol. 127, p. 607, 1953.
[5] E. L. O'Neill, "Spatial filtering in optics," *IRE Trans. Inform. Theory*, vol. IT-2, pp. 56–65, June 1956.
[6] G. L. Turin, "An introduction to matched filters," *IRE Trans. Inform. Theory*, vol. IT-6, pp. 311–329, June 1960.
[7] A. Vander Lugt, "Signal detection by complex spatial filtering," *IEEE Trans. Inform. Theory*, vol. IT-10, pp. 139–145, Apr. 1964.
[8] L. J. Cutrona *et al.*, "On the application of coherent optical processing techniques to synthetic aperture radar," *Proc. IEEE*, vol. 54, pp. 1026–1032, Aug. 1966.
[9] E. N. Leith and J. Upatnieks, "Reconstructed wavefronts and communication theory," *J. Opt. Soc. Amer.*, vol. 52, pp. 1123–1130, Oct. 1962.
[10] D. Casasent, "Optical pattern and character recognition," in *Handbook of Holography*, H. J. Caulfield, Ed. New York: Academic Press, 1979.
[11] J. W. Goodman, "Operations achievable with coherent optical information processing systems," *Proc. IEEE*, vol. 65, pp. 29–38, 1977.
[12] J. T. Tippett *et al.*, Eds., *Optical and Electro-Optical Information Processing*. Cambridge, MA: M.I.T. Press, 1965.
[13] A. Vander Lugt, "Coherent optical processing," *Proc. IEEE*, vol.

62, pp. 1300–1319, 1974.
[14] *Proc. IEEE, Special issue on Optical Computing*, vol. 65, Jan. 1977.
[15] D. Casasent, Ed., *Optical Data Processing: Applications, Vol. 23, Topics in Applied Physics*. Heidelberg, Germany: Springer-Verlag, 1978.
[16] L. J. Cutrona, E. N. Leith, C. J. Palermo, and L. J. Porcello, "Optical data processing and filtering systems," *IRE Trans. Inform. Theory*, vol. IT-6, pp. 386–400, June 1960.
[17] M. Monahan, K. Bromley, and R. P. Bocker, "Incoherent optical correlators," *Proc. IEEE*, vol. 65, pp. 121–129, Jan. 1977.
[18] P. S. Consodine and R. A. Gonsalves, "Optical image enhancement and image restoration," in *Optical Data Processing: Applications, Vol. 23, Topics in Applied Physics*. Heidelberg, Germany: Springer-Verlag, 1978.
[19] G. W. Stroke, *et al.*, "Image improvement and three-dimensional reconstruction using holographic image processing," *Proc. IEEE*, vol. 65, pp. 39–62, Jan. 1977.
[20] S. H. Lee, "Recent developments in optical information processing using non-linearity and feedback," in *Optical Information Processing*, vol. 2, E. S. Barrekette *et al.*, Ed., New York: Plenum, 1978, pp. 171–191.
[21] J. W. Goodman, *Introduction to Fourier Optics*. New York: McGraw-Hill, 1968.
[22] H. Kasdan and D. Mead, "Out of the laboratory and into the factory: optical computing comes of age," in *Proc. Electronic Optic System Design Conf.* (Anaheim, CA) Oct. 1975.
[23] H. Stark, "An optical-digital computer for parallel processing of images," *IEEE Trans. Comput.*, vol. C-24, pp. 340–347, Apr. 1975.
[24] G. Lendaris and G. Stanley, "Diffraction pattern sampling for automatic pattern recognition," *Proc. IEEE*, vol. 58, pp. 198–216, Feb. 1970.
[25] G. Stanley and G. Lendaris, "Diffraction pattern sampling for automatic pattern recognition," *Soc. Photo-Opt. Instrum. Eng.*, vol. 18, pp. 127–153, June 1969.
[26] R. Kruger, W. Thompson and A. Turner, "Computer diagnosis of pneumoconiosis," *IEEE Trans. Syst. Man Cybern.*, vol. SMC-4, pp. 40–49, Jan. 1974.
[27] *Optical Eng., Special Issue on Acoustooptics*, vol. 16, Sept. 1977.
[28] L. Lambert, M. Arm and A. Aimette, chapter 38 in *Optical and Electro-Optical Information Processing*, J. T. Tippet *et al.*, Eds., Cambridge, MA: M.I.T. Press, 1965, pp. 715–748.
[29] L. Lambert, "Electro-Optical Correlation Techniques," in *Textbook of Modern Radar Techniques*. New York: Wiley, 1966.
[30] W. T. Maloney, "Acousto-optical approaches to radar processing," *IEEE Spectrum.*, vol. 6, pp. 40–49, Oct. 1969.
[31] E. B. Felstead, "A simple real-time incoherent optical correlator," *IEEE Trans. Aerosp. Electron. Syst.*, vol. AES-3, pp. 907–914, Nov. 1967.
[32] L. Flores and D. Hecht, "Acousto optic signal processors," *Proc. Soc. Photo-Opt. Instrum. Eng.*, vol. 118, pp. 182–192, Aug. 1977 (IEEE Cat. No. 77CH1265-8C).
[33] R. Sprague and C. Koliopolous, "Time integrating acoustooptic correlator," *Appl. Opt.*, vol. 15, pp. 89–92, Jan. 1976.
[34] J. W. Goodman, A. R. Dias and L. M. Woody, "Fully parallel, high-speed incoherent optical method for performing discrete Fourier transforms," *Opt. Letts.*, vol. 1, pp. 1–3, Jan. 1978.
[35] J. Lee, B. Udelson, and N. Berg, "Acousto-optic signal processing for radar applications," *Proc. Soc. Photo-Opt. Instrum. Eng.*, vol. 128, pp. 192–201, Sept. 1977.
[36] D. Casasent and W. Sterling, "A hybrid optical/digital processor: hardware and applications," *IEEE Trans. Comput.*, vol. C-24, pp. 348–357, Apr. 1975.
[37] D. Gabor, "Microscopy by reconstructed wavefronts. I and II," *Proc. Roy. Soc.* (Ser. A), vol. 197, p. 454, 1959 and (Gen.) vol. 64, p. 449, 1951.
[38] C. L. Burckhardt, "Storage capacity of an optically formed spatial filter for character recognition," *Appl. Opt.*, vol. 6, pp. 1359–1366, Aug. 1967.
[39] Di Chen and J. D. Zook, "An overview of optical data storage technology," *Proc. IEEE*, vol. 63, pp. 1207–1230, Aug. 1975.
[40] S. Almeida and J. K-T Eu "Water pollution monitoring using matched spatial filters," *Appl. Opt.*, vol. 15, pp. 510–515, Feb. 1976.
[41] A. Vander Lugt, F. B. Rotz and A. Klooster, "Character reading by optical spatial filtering," in *Optical and Electro-Optical Information Processing*, J. T. Tippet *et al.*, Eds., Cambridge, MA: M.I.T. Press, 1965, pp. 125–141.
[42] D. Casasent and A. Furman, "Optimization of parameters in matched spatial filter synthesis," *Appl. Opt.*, vol. 16, pp. 1662–1669, June 1977. See also D. Casasent and A. Furman, "Sources of correlation degradation," *Appl. Opt.*, vol. 16, pp. 1552–1661, June 1977.
[43] K. Leib *et al.* "Aerial reconnaissance film screening using optical matched-filter image-correlator technology," *Appl. Opt.*, vol. 17, pp. 2892–2899, Aug. 1978.
[44] J. Rau, "Detection of difference in real distributions," *J. Opt. Soc. Amer.*, vol. 56, pp. 1490–1494, Nov. 1966.
[45] D. Casasent, "Spatial light modulators," *Proc. IEEE*, vol. 65, pp. 143–157, Jan. 1977.
[46] *Opt. Eng., Special Issue on Real Time Spatial Light Modulators*, vol. 17, July 1978.
[47] B. H. Billings, "The electro-optic effect in uniaxial crystals of the dihydrogen phosphate type, I. Theoretical," *J. Opt. Soc. Amer.*, vol. 39, p. 797, Oct. 1949.
[48] A. Gara, "Real-time optical correlation of 3-*D* scenes," *Appl. Opt.*, vol. 16, No. 1, pp. 149–153, Jan. 1977.
[49] H. Brown and B. Markevitch, "Radar signal optical processor," *Proc. Soc. Photo-Opt. Instrum. Eng.*, vol. 128, pp. 204–209, Sept. 1977.
[50] P. M. Woodward, *Probability and Information Theory with Applications to Radar*. New York: Pergamon, 1955.
[51] D. Casasent and M. Saverino, "Optical image processing for missile guidance," *Proc. Photo-Opt. Instrum. Eng.*, vol. 118, pp. 11–20, Aug. 1977.
[52] R. Y. Wong, "Sensor transformations," *IEEE Trans. Syst. Man Cybern.*, vol. SMC-7, pp. 836–841, Dec. 1977.
[53] R. Y. Wong, "Sequential scene matching using edge features," *IEEE Trans. Aerosp. Electron. Syst.*, vol. AES-14, pp. 128–140, Jan. 1978.
[54] G. S. Robinson, "Detection and coding of edges using directional masks," *Opt. Eng.*, vol. 16, pp. 580–585, Nov. 1977.
[55] D. Casasent and Y. Barniv, "Coherent optical processing for multi-sensor image processing," *Proc. Photo-Opt. Instrum. Eng.*, vol. 137, Mar. 1978.
[56] D. Casasent and D. Psaltis, "New optical transforms for pattern recognition," *Proc. IEEE*, vol. 65, pp. 77–84, 1977.
[57] G. Robbins and T. S. Huang, "Inverse filtering for linear shift invariant image systems," *Proc. IEEE*, vol. 60, pp. 862–872, July 1972.
[58] A. A. Sawchuk, "Space variant motion degradation and restoration," *Proc. IEEE*, vol. 60, pp. 854–861, July 1972.
[59] R. Bracewell, *The Fourier Transform and Its Applications*, New York: McGraw-Hill, 1965.
[60] D. Casasent and D. Psaltis, "Deformation-invariant, space-variant optical pattern recognition," in *Progress in Optics, vol. XVI*, E. Wolf, Ed. New York: North Holland Publ., 1978.
[61] D. Casasent, J. Hackwelder, and P. DiLeonardo, "A microprocessor-based optical/digital processor," *Proc. Soc. Photo-Opt. Instrum. Eng.*, vol. 117, pp. 26–32, Aug. 1977.
[62] E. Rau, "Real-time complex spatial modulation," *J. Opt. Soc. Amer.*, vol. 57, pp. 798–802, June 1967.
[63] C. W. Weaver *et al.*, "The optical convolution of time functions," *Appl. Opt.*, vol. 9, pp. 1672–1682, July 1970.
[64] D. Casasent and A. Furman, "Equalizing and coherence measure correlators," *Appl. Opt.*, vol. 17, 1978.
[65] H. J. Caulfield and W. T. Maloney, "Improved discrimination in optical character recognition," *Appl. Opt.*, vol. 8, pp. 2354–6, Nov. 1969.
[66] A. W. Lohmann, "Incoherent processing of complex data," *Appl. Opt.*, vol. 16, pp. 261–263, Feb. 1977.
[67] A. W Lohmann and W. T. Rhodes, "Two pupil synthesis of optical transfer functions," *Appl. Opt.*, vol. 17, pp. 1141–1151, Apr. 1978.
[68] W. Stoner, "Incoherent optical processing via spatially offset pupil masks," *Appl. Opt.*, vol. 17, pp. 2454–2467, Aug. 1978.
[69] A. Furman and D. Casasent, "Bipolar incoherent optical pattern recognition by carrier encoding," *Appl. Opt.*, submitted for publication.
[70] A. W. Lohmann and D. P. Paris, "Computer generated spatial filters for coherent optical data processing," *Appl. Opt.*, vol. 7, p. 651, 1968.
[71] W. H. Lee, "Sampled Fourier transform hologram generated by computer," *Appl. Opt.*, vol. 9, p. 639 1970.
[72] J. W. Goodman, A. R. Dias, and L. M. Woody, "Fully parallel, high-speed, incoherent optical method for performing discrete Fourier transforms," *Opt. Lett.*, vol. 2, pp. 1–3, Jan. 1978.
[73] Y. Tsunoda, A. Huang, and J. W. Goodman, "Proposed optoelectronic residue matrix vector multiplier," *Appl. Opt.*, 1979.
[74] S. A. Collins, Jr., "Numerical optical data processor," *Proc. Soc. Photo-Opt. Instrum. Eng.*, vol. 128, pp. 313–319, Sept. 1977.
[75] D. Psaltis and D. Casasent, "A correlation-based approach to optical residue arithmetic," *Appl. Opt.*, 1979.

Chapter 9

Papers Published Under this AFOSR Contract

(1 October, 1978 -- 31 September 1979)

1. D. Casasent and A. Furman, "Equalization and Coherence Measure Correlators," Appl. Opt., 17, 3418-3423 (November 1978).

2. A. Furman and D. Casasent, "Bipolar Incoherent Optical Pattern Recognition by Carrier Encoding," Appl. Opt., 18, 660-665 (March 1979).

3. D. Casasent and D. Munoz, "Statistical and Deterministic Aspects of Multi-Sensor Optical Image Pattern Recognition," SPIE, 201 (August 1979).

4. D. Casasent and D. Psaltis, "Optical Pattern Recognition Using Normalized Invariant Moments," SPIE, 201 (August 1979).

5. D. Casasent and D. Psaltis, "Parallel Optical Fourier Transform Techniques for Fourier Spectroscopy," SPIE, 191 (August 1979).

6. D. Casasent, M. Libby and D. Psaltis, "New Acousto-Optic Signal Processing Architectures and Applications," SPIE, 202 (August 1979).

7. C. Hester and D. Casasent, "Optical Pattern Recognition Using Average Filters To Produce Discriminant Hypersurfaces" SPIE, 201 (August 1979).

8. H. J. Caulfield and D. Casasent, "Coherent Optical Pattern Recognition," Lasers 1978, Paper 168-09 (December 1978).

9. D. Casasent, "Coherent Optical Computing," Computer, 12, 27 (January 1979).

10. T. Luu and D. Casasent, "Effects of Wavefront Propagation Error in an Optical Correlator," Appl. Opt., 18, 791 (March 1979).

11. D. Casasent, "Review of Coherent Optical Correlation Techniques," SPIE, 177, 2 (1979).

12. D. Casasent, "Coherent Optical Pattern Recognition," Proc. IEEE, 67, 813 (May 1979).

13. D. Casasent, "Performance Evaluation of Spatial Light Modulators," Appl. Opt., 18, 2445-53 (July 1979).

14. D. Casasent, et al., "New Birefringence Theory and Use of the Photo-DKDP SLM in Optical Data Processing," SPIE, 202 (August 1979).

Chapter 10

Seminars and Talks Presented on AFOSR Research

(1 October 1978 -- 31 September 1979)

1. 25 October 1978, "Optical Data Processing at CMU," Carnegie-Mellon University, (Varian Associates), Pittsburgh, Pennsylvania.

2. 26 October 1978, "Optical Data Processing at CMU," Carnegie-Mellon University, (Sophmore Seminar), Pittsburgh, Pennsylvania.

3. 27 October 1978, "Optical Data Processing at CMU," Carnegie-Mellon University, (Berkeley University), Pittsburgh, Pennsylvania.

4. 12 December 1978, "Coherent Optical Pattern Recognition," Lasers 1978 Conference, Orlando, Florida.

5. 15 February 1979, "Space-Variant Image and Signal Processing," Northrop Corporation, Anaheim, California.

6. 16 February 1979, "Optical Data Processing," SRI, Palo Alto, California.

7. 20 February 1979, "Fourier Optics," White Sands Missile Range, New Mexico.

8. 21 February 1979, "Coherent Optical Pattern Recognition," White Sands Missile Range, New Mexico.

9. 15 March 1979, "Space-Variant Image and Signal Pattern Recognition," ARI, Boston, Massachusetts.

10. 15 March 1979, "Space-Variant Image and Signal Pattern Recognition," OSA, Boston, Massachusetts.

11. 17 April 1979, "A Review of Coherent Optical Correlation Techniques," SPIE East, Washington, D.C.

12. 17 May 1979, "Optical Signal and Image Processing," Inst. Phys. Chem. Res., Tokyo, Japan.

13. 22 May 1979, "Optical Signal and Image Processing," Osaka University, Osaka, Japan.

14. 25 May 1979, "Optical Signal and Image Processing," Hokkaido University, Sapporo, Japan.

15. 4 June 1979, "Optical Data Processing," Hughes Research Lab, Los Angeles, California.

16. 6 June 1979, "Optical Image Processing," SCI, Palo Alto, California.

17. August 1979, "Statistical and Deterministic Aspects of Multi-Sensor Optical Image Pattern Recognition," SPIE, San Diego.

18. August 1979, "Optical Pattern Recognition Using Normalized Invariant Moments," SPIE, San Diego.

19. August 1979, "Parallel Optical Fourier Transform Techniques for Fourier Spectroscopy," SPIE, San Diego.

20. August 1979, "New Acousto-Optic Signal Processing Architectures and Applications," SPIE, San Diego.

21. August 1979, "Optical Pattern Recognition Using Average Filters to Produce Discriminant Hypersurfaces," SPIE, San Diego.

22. August 1979, "New Binefringence Theory and Use of the Photo-DKDP SLM in Optical Data Processing," SPIE, San Diego.